ABSTRACT

Title of thesis: SIMULATION OF VAPORIZATION AND COMBUSTION OF A LARGE-SCALE CRYOGENIC LIQUID METHANE POOL

Jason Michaels McGill, Master of Science, 2006

Thesis directed by: Professor Arnaud Trouvé
Department of Fire Protection Engineering

Professor Gregory Jackson
Department of Mechanical Engineering

The risk of terrorist attack on large cryogenic hydrocarbon fuel tankers is unclear, due partly to difficulties in understanding how the spill, pool vaporization, turbulent dispersion and fuel-vapor mixing are coupled. The current study's objective is to model the vaporization, dispersion, and deflagration of liquid methane pools boiling on water while subjected to airflow around a prismatic body. The Fire Dynamics Simulator CFD code developed by NIST facilitates large-eddy simulations of the turbulent dispersion that is coupled to a combustion model capturing premixed flame ignition, propagation, and if sustainable, transition to diffusion pool fire. The pool and water are characterized as isothermal surfaces with a dominant convection heat transfer mode. Flammable mass, cloud visualization, flame height, temperature, and heat flux provide diagnostics. Slower winds produce larger flammable clouds, but insufficient mixing inhibits successful ignition. Provisional adjustment of the flammability limits demonstrates reasonable flame height and diffusion flame heat release rates.

SIMULATION OF VAPORIZATION AND COMBUSTION OF A LARGE-SCALE CRYOGENIC LIQUID METHANE POOL

by

Jason Michaels McGill

Thesis submitted to the Faculty of the Graduate School of the
University of Maryland, College Park in partial fulfillment
of the requirements for the degree of
Master of Science
2006

Advisory Committee:

Professor Arnaud Trouvé, Chair
Professor Gregory Jackson, Co-Chair
Professor James Duncan

TABLE OF CONTENTS

LIST OF TABLES

LIST OF FIGURES

CHAPTER 1 – INTRODUCTION

1.1 Shipping of Liquid Hydrocarbons and Potential Hazards

United States governmental, residential and commercial sectors rely on the import of hydrocarbon fuels for the purposes of, among other things, heating, electricity, and transportation. Liquefied Natural Gas (LNG) usage and consequently, its importation, has increased since the late 1990's and the early 2000's [1]. An estimated 7.6 billion metric tons of LNG was imported daily in the United States during 2005 [2]. To compare, approximately 22,790 metric tons of Liquefied Petroleum Gases (LPG) are imported daily into the United States. LPG types commonly imported include ethane/ethylene, propane/propylene, butane/butylene, and isobutane/isobutylene [3].

1.1.1 The Growing Significance of LNG to Global Energy Demand

Liquefied Natural Gas (LNG) has been considered as a means of storing and transporting natural gas (composed primarily of methane – 85% or usually higher) since the 19th century. Commercial natural gas liquefying stations have existed since 1941 to provide fuel for electrical power during peak demand hours in the United States [4]. Long distance shipments of LNG have occurred since 1959, and tankers produced explicitly for LNG transport were commissioned in 1964 [5]. Due to growing power demands from industries, residencies, and businesses worldwide -and at least for the short term future while supplies are plentiful- LNG will undoubtedly play an increasingly large supplemental role in meeting the energy demands in the industrialized world [6].

Natural gas consumption in the United States is expected to rise to 30.7 trillion cubic feet (Tcf) in 2025 from 22.0 Tcf in 2003. The domestic electric power generating sector is expected to consume 9.4 Tcf of the supply in 2025 in contrast to the 5.0 Tcf consumed in 2003, due primarily to the "lower capital costs, higher fuel efficiency, shorter construction lead times, and lower emissions" of natural gas-fired generators compared to coal-fired generators. It should be noted that currently, high natural gas prices have dissuaded gas-fired plant production in favor of cheaper coal-fired generators. It is predicted that 130 gigawatts of natural-gas-fired-capacity would be added from the end of 2004 to 2030, while 154 gigawatts of coal-fired-capacity would be added during the same time period [6, 7]. Growing demand in petroleum refining, bulk chemical, and food processes constitute much of the industrial natural gas consumption. Residential and commercial-sector natural gas consumption is also expected to boost demand in the following decades [6].

As demand for natural gas increases yearly, annual natural gas production is projected to remain comparatively unvaried. Conventional natural gas production in the lower 48 states, as well off-shore production facilities will actually demonstrate drops in natural gas outputs by 2025 of 9 percent and 7.7 percent, respectively [6]. Production levels are currently sustained through alternative natural gas extraction methods; unconventional gas production from tight sands, shales, and coalbed methane sources account for 44 percent of projected natural gas production in the lower 48 states in 2025, a 9 percent increase from 2003 production totals. Crude oil reserves providing associated-dissolved

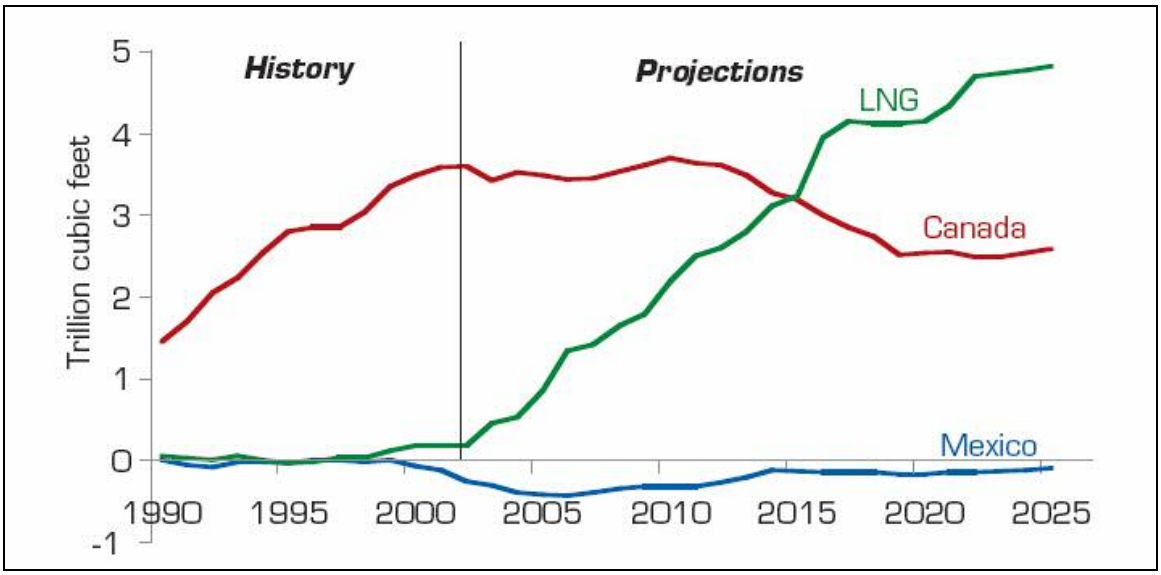

Figure 1: Projection of Natural Gas Imports to the United States (Negative values indicate importation of American natural gas) [4]

natural gas will account for an estimated 3.1Tcf in 2010, after which there too will be a decline in AD natural gas production (2.4 Tcf in 2025).

LNG will account for the majority of natural gas imports to the United States in the near future. Worldwide liquefaction capacity will have increased from 6.6 Tcf in 2003 to 9.4 Tcf in 2007. Statistics for LNG import growth in the United States predict that LNG imports will provide 8 percent of natural gas consumption by 2010, up from 2 percent of consumption in 2003. The LNG tanker fleet was estimated at 151 in 2003, and is expected to reach 193 total vessels in 2006. Ship hold volumes currently range from below 50,000 to over 120,000 cubic meters, each equipped with 3 to 5 separate LNG tanks for storage during shipment. The anticipated growth in LNG demand has fueled proposals for larger vessels with up to 250,000 cu meter capacities [8, 9]. Ship manufacturers have also begun to utilize dual fuel propulsion, whereby marine diesel is

supplemented with boil-off LNG gas to power the ships diesel-electric motors [8]. Projected LNG consumption and competition among shipbuilders have driven a significant reduction of ship cost; 138,000 cu meter vessels now cost approximately $150 to $160 million compared to $280 million in 1995 [5, 8].

The Southern Union-owned Lake Charles regasification facility produces the largest daily sendout of natural gas in the United States at 1.5 billion cubic feet (Bcf). Total daily output from the existing American regasification plants stands at 4.735 Bcf. Nine American LNG terminal projects have received approval from the Federal Energy Regulatory Commission (FERC), not including two approved LNG terminals in the Bahamas. Integration with the existing U.S. LNG terminal infrastructure would add an additional 12.6 Bcf to the daily peak sendout capacity. There are 5 approved North American LNG terminals outside of the United States; three are from Mexico and have a proposed peak sendout of 3.1 Bcf; two others are located in New Brunswick and Nova Scotia in Canada, with a total peak sendout of 2.0 Bcf daily [10].

Opposition to the drilling, liquefaction, shipment, regasification, and distribution of natural gas has grown parallel to the growth of LNG production and shipment worldwide, and reasoning behind LNG concerns is myriad. Shell and ExxonMobil gas extraction projects on Sakhalin Island, Russia have been cited for “massive fish die-offs…and contamination of the local water supply” in a marine environment that is home to the Western Pacific Gray Whale, of which only 100 still exist. LNG opponents also claim extraction, liquefaction, shipping and regasification processes contribute up to 40 percent

more carbon dioxide than just burning domestic natural gas [11]. Opponents regularly cite renewable energies such as wind turbine, solar power, and geothermal resources as cleaner, less politically charged, and viable alternatives to a foreign dependence on liquefied natural gas. Human rights advocates cite the danger indigenous populations have been exposed to as a result of natural gas extraction on Sakhalin Island, Camisea in Peru, and in the Tangguh natural gas fields in West Papua, Indonesia [12].

1.1.2 Associated Risk of LNG Transport

There are four representative events that fuel the reluctance of communities in the United States, Mexico, and Canada to allow LNG import regasification terminals to be constructed in proximity to their respective residencies and metropolitan areas:

Skikda LNG Liquefaction Plant Explosion (Algeria) - The six gas-liquefaction plants (units) in Skikda are part of a 3,100-acre industrial zone, which provides 12,000 jobs to the northeastern Algerian port city of 152,000 people. Liquefaction Unit 40 detonated on January 19, 2004 at 6:40 p.m., causing the explosions of adjacent liquefaction Units 20 and 30. Total deaths resulting from the accident totaled 27, with 80 more people sustaining injuries. The ensuing shockwave induced structural damage to maintenance, security, and administrative facilities in the industrial zone, in addition to wharfs at Skikda harbor and residential homes more than a mile away.

The explosion was blamed on a gas leak that allowed vapors to accumulate and then ignite in the firebox of Unit 40's boiler once the leak/air mixture was within the flammability limits. It is believed this small ignition within the firebox, coupled with the

enclosed nature and location of the ignition, allowed for substantial pressure rise and transition to a large detonation. Whether the vapor was natural gas is unknown. Proponents of LNG in the United States disregard the relevancy of the incident because; U.S. regasification terminals are not equipped with boilers; and claims borne out by accident investigation teams allege poor maintenance of the Skikda facility. These allegations include biweekly "technical intervention" on gas-leaking cryogenic units, neglected complaints by upper management pertaining to boiler deficiencies, and Unit 40's obsolescence (it was constructed in 1976 and refurbished in the late 1990's) [4, 13].

The numerous unanswered questions regarding deficient risk prevention measures, the cause of the Skikda explosion and the inadequacy of emergency preparedness, have galvanized LNG opponents, whose protests have recently repelled ExxonMobil's proposed LNG conditioning facilities in Mobile, Alabama [13].

September 11, 2001 - The vast scope of the terrorist attacks on the World Trade Center, the Pentagon, and United Airlines Flight 93 have fueled concerns of future incidents that could kill and injure thousands of people, and damage industries essential for continued commerce in the United States.

USS Cole Bombing - Suicide bombers guided a small explosive-laden craft into the port side of the USS Cole on October 12, 2000, as the *Arleigh Burke*-class destroyer refueled in the harbor of Aden, Yemen. The ensuing blast claimed the lives of 17 American sailors and injured over 40 other crewmen. The attack, which left a 1,600 square foot hole in the

USS Cole's hull, poignantly illustrates the scenario delineated by LNG opponents fearful of regasification import terminals adjacent to residences and vital commercial areas; reliance on neighboring LNG terminals would simultaneously pose risks to proximate communities and damage the ability to balance regional energy demands [14].

Limburg Oil Tanker Bombing - The potential for a terrorist attack to impact fuel concerns was further elucidated in October of 2002 when a small craft rammed the French oil tanker Limburg off the coast of Yemen. The collision and ensuing explosion penetrated 7 to 8 meters into the double-hulled vessel. It is believed, as in the case of the bombing of the USS Cole, the impacting vessel was piloted by suicide bombers and equipped with explosives [15].

The potential damage of an LNG tanker breach will vary with individual incidents. The size of the hole and volume flow rate of the cryogenic liquid is dependant on whether the damage to the hull was accidental or intentional. The volume flow rate is likewise affected by the design of the LNG vessel and its cargo tanks. Moss tankers utilize spherical LNG compartments to transport natural gas after liquefaction. Fire-prevention methods such as nitrogen-purged compartments below the spherical tanks have also been implemented in their design. Additionally, Moss tankers are double-hulled vessels; the 2-meter space between is a ballast that is purged with a full cargo load, and also a make-shift hold for leaking LNG in the event of a breach. LNG tankers can be fitted with self-supporting prismatic cargo tanks as an alternative to the Moss design [4].

LNG tanker specifications are imposed by the International Maritime Organization code for the carriage of liquefied gases in bulk, which necessitate primary and secondary containment barriers for all containment systems. Ship holds are also required to contain leaking products for 15 days. The space between individual tanks, the number of compartments in a LNG tanker, and the location of the breach will also dictate the severity of the spill and immediacy of the consequences [5].

In December 2004, Sandia National Laboratories published a detailed critical analysis of, and proposed emergency response to, various risks associated with LNG spills over water [4]. The document provides analyses of both accidental (collision, grounding) and intentional (terrorist) breach and dispersion scenarios with the aid of finite-volume analysis and CFD software. Conclusions from the report's accidental and intentional breach analyses are summarized here to outline the potential consequences associated with LNG transport, which are addressed in this project's large-scale simulations.

Accidental LNG Spill

The Sandia report categorizes accidental LNG tanker collisions as either collisions with small vessels, collisions with large vessels, or accidental groundings. Breaching, defined as the rupturing of both of the LNG vessel hulls and the LNG cargo tank, is viable only in the accidental large-vessel collision scenario. This is because neither the grounding nor small-vessel collision types generate enough kinetic energy to breach the LNG cargo tank. Finite-volume analysis concluded specifically that small vessels would not rupture the inner hull of a double-hulled LNG tanker. Collisions with large vessels could produce

cargo tank ruptures of 5 to 10 m^2, though additional analysis concludes that perhaps only .5 to 1 $m^2$of the hole may actually leak LNG. Cryogenic damage to the tanker steel due to the vaporization of the super-cooled liquefied gas is predicted, though the "extent and impact of the damage will depend on the breach and spill size and location and effectiveness of risk prevention and mitigation strategies…"

The report's spill dispersion hazard analysis established potential impact of deflagrations in terms of incident heat flux on a surface, where 37.5 kW/m^2 was a high impact on public safety, and 5 kW/m^2 was a low impact safety hazard. High speed accidental collisions can result in small fires, damage to the LNG vessel, and in the instance of delayed ignition of the spilled LNG, a vapor cloud dispersion that could drift over highly populated areas. It was concluded that, within 250 meters of the spill origin, there was high potential of fire and vapor cloud dispersion to impact public safety. The risk of fire and vapor cloud dispersion was moderate out to 750 meters from the spill. The risk of fire was estimated as low beyond 750 meters, although public safety remained moderately compromised when considering vapor cloud drift. Low-speed collisions with, and grounding of LNG vessels, posed low risks to public safety even at distances of 250 meters from the spill origin.

Intentional LNG Spill

Eulerian finite volume code was utilized to model the shock physics associated with intentional breaching scenarios, and it was concluded that cargo tank ruptures between 2 and 12 m^2 were possible. The Sandia study adopted 5 to 7 m^2 as an appropriate range for

intentional spills. As in the case of the accidental spill analysis, it was concluded that the LNG vessel would likely be subjected to varying degrees of cryogenic damage, the extent of which depends on the breach size, the number of ruptured cargo tanks, and if existing cryogenic damage initiated further structural failure. The upper limit of vessel hole size (12 m^2) could lead to LNG pool diameters as large as 512 meters and -assuming ignition from a source at the spill site- severe radiative heat fluxes of 37.5 kW/m^2 over 600 meters away from the spill origin. Potential risk from severe thermal radiation generally extended 500 meters from the pool origin; the distance between 500 and 1600 meters was determined to be an intermediate hazard zone, while low thermal hazards were associated with distances beyond 1.6 km.

It was concluded that during an intentional breaching event, hazard zones can extend beyond 3.6 km if an ignition source is not available at the pool origin. Vapor dispersion would be possible under these conditions, and assuming light winds and stable atmospheric conditions, could allow the gas cloud to drift into heavily populated regions where it could encounter various ignition sources. Due to the high probability of the vaporizing LNG being ignited at the pool origin during the course of an intentional breaching event, dispersion distances of this magnitude are considered highly improbable. However, the possibility of an intentional spill without breaching was considered, and the absence of an immediate ignition source could result in a vapor cloud dispersion of over 1600 meters.

As stated in the summaries of accidental and intentional spill risks, the LNG cryogen has the potential to cause structural damage to the vessel and cargo holds. Human contact with liquefied natural gas may cause cryogenic burns, similar to when skin comes in contact with liquid nitrogen. High pressure ignition sources (grenades, mortars, suicide-bombers) could initiate detonations near the spill source and in confined areas. There also exists the possibility of asphyxiation due to high concentrations of LNG vapor; this is secondary to the risk of deflagration due to the high number of potential ignition sources in the aftermath of accidental and intentional spills.

Real world hydrocarbon spills, deflagrations, and detonations, as well as the attacks on national and commercial infrastructures, prompted the Sandia report. The current study similarly investigates the vaporization, dispersion, and deflagration of cryogenic hydrocarbon pools. Physical assumptions concerning the pool's heat transfer and spreading mechanisms are used in conjunction with the numerical modeling software FDS to predict the mass vaporization rate of a cryogenic spill, as well as eventual cloud dispersion and possible ignition. The resultant heat release rate is also predicted, should the flammable cloud be subjected to an ignition source.

1.2 Review of Spill Modeling

The various attempts at modeling large chemical releases encompass wide-ranging initial conditions, simplifying assumptions, analyses, results, and conclusions. Differences in spill models are attributable to sparse real-world data by which modeling estimates can be validated, and the absence of experimental data involving spill sizes comparable to

intentional breaching scenarios. There have been 8 marine LNG spills since shipment began in 1959, with no recorded cargo fires or shipboard fatalities [4]. Studies conducted by Fay, Conrado-Vesovic, and Lehr, in addition to shallow-water conservation equations, have made use of simplifying assumptions and produced results and conclusions utilized in the current modeling code [16, 17]. Material from those studies amenable to the research conducted for this paper is addressed below.

1.2.1 Fay Model

Fay has produced analytical and computer models that predict the behavior of spills of LNG and oil from the holds of tankers [18]. The models are based on analytical analysis of force and mass balances which take into account simplified and radially symmetric scenarios, as well as data taken from experiments involving oil and LNG spills. Fay considers the mechanisms by which a chemical pool spreads (horizontal pressure gradient due to gravity potential, and surface tension) and is retarded (inertial and viscous forces), and performs an order of magnitude analysis to determine the predominant forces during initial, intermediate, and long time scales. Thus, Fay divides the spread history into three regimes:

- Gravity spreading and inertial retardation.
- This is followed by pool spreading governed by gravity force which is counteracted by viscous force.
- During long time scales (measured in days and weeks for an oil slick) surface tension overtakes gravity potential as the primary spreading mechanism, while viscosity remains the most important impeding force.

Though it is widely used to model LNG spreading, the Fay model produces values different from those measured from experimental LNG spills [16]. Fay uses his magnitude analysis criteria as a basis for describing the relationship between the pertinent physical and geometric characteristics of a spreading pool. The volumetric flow rate of cryogenic liquid discharged from the ship hold, hydrocarbon liquid mass density, the time-dependent height of the cryogen in the ship, as well as the vaporization rate of the hydrocarbon pool, all characterize the pool behavior.

Fay defines two types of definitive pool behavior dependent on the size of the breach in the hydrocarbon tanker; 'small' holes in the breached ship hold yield a quasi-steady evaporation process, whereby the evaporation rate of the pool and the discharge rate from the ruptured tanker are the same [19]. Large ruptures in the hydrocarbon tanker result in pools that discharge in much shorter time scales than quasi-steady pools. Pool vaporization results from the boiling of the cryogenic liquid on the surface of the water, or the thermal radiation of an incident pool fire. Fay differentiates between quasi-steady and instantaneous pool behavior by way of magnitude analysis, similar to that used to define his three spreading regimes. Computational cost and software limitations limit the present study to modeling quasi-steady (constant pool area) spills.

Lehr and Simecek-Beatty provided contrasting results from spill modeling of petroleum products and LNG. Gravity-inertial regime spreading of a radial pool was assumed, where the spill volume dictates pool radius for instantaneous releases; the volume flow rate of the spill dictates pool radius for a continuous release [16]. In using Fay's spill

regime model, Lehr and Simecek-Beatty assume viscosity and surface tension-related effects are ignored, and that the pool spreads on a quiescent surface (there is no modeling of waves). It is also assumed by Lehr and Simecek-Beatty that the body of water is a vast heat source, identical to the assumptions made by Conrado and Vesovic in their model.

1.2.2 Conrado and Vesovic

Conrado and Vesovic devised a numerical model estimating the vaporization rate of LNG and liquefied petroleum gas (LPG) on unconfined water surfaces [17]. The chemical composition of each was accounted for, an abscondence of the common assumption that the spilled hydrocarbon is a pure fluid. LNG was assumed a binary mixture of 90% methane/10% ethane, while LPG was a by-mass 90% propane/10 % butane mixture. The model assumed an instantaneous cryogen release which takes place in the gravitational-inertial spreading regime, as defined by Fay, and viscous and surface tension forces negligible due to the rapid evaporation of the cryogen. The water and spilled fluid are assumed to be flat isothermal surfaces. The rate of spread is modeled as a radial propagation governed by a leading front velocity.

Conrado and Vesovic determined the boiling regime (nucleate, transitional, or film boiling) for the different components of the cryogenic mixtures to set an appropriate heat transfer coefficient during the vaporization process. Only heat transfer from the water to the spilled hydrocarbon liquid is accounted for, as transfer by air convection and radiation contribute less than 5 percent of the total thermal energy exchange. Interfacial turbulence due to the hydrocarbon spill propagation and the thermal inertia of the unconfined water

are assured to minimize water-cryogen temperature gradients, which might induce ice formation. Additionally, ice formation during cryogenic spill events has never been observed on open, unconfined water; only experiments utilizing shallow and confined water tanks have produced ice formation. A fourth-order Runga-Kutta numerical scheme was used to solve the coupled first-order differential equations governing cryogen spreading and vaporization.

In summary, computer simulations using the appropriated model show that the difference in composition of pure methane and LNG affected the vaporization rate of the cryogenic fluid; the vaporization rate of LNG decreased as the pool became more ethane rich, while pure methane exhibited an increased rate for all time in the simulation. LPG similarly evaporated faster than pure propane, though the change in vaporization rate was not as pronounced as in the LNG case.

1.3 Review of Dispersion Modeling for Chemical Spills

Accurate modeling for chemical spills requires not only the simulation of the pool spread, but also coupling to equations governing the vaporization of the chemical (due to pool boiling, convection, and radiation), and the subsequent dispersion of the vapor above the pool. The analysis encompasses heat transfer principles to determine pool temperature and vaporization flux, and a model predicting vapor cloud dispersion in an environment subject to turbulent flow.

1.3.1 Modeling Spill Vaporization

Vaporization of a spilled chemical at its gas-phase/liquid-phase interface is represented by a mass vaporization flux, which is a function of a mass transfer coefficient and fuel vapor concentration (mass fraction). The mass fraction of the chemical spill at the interface can be used to obtain its surface partial pressure. The Clausius-Clapeyron equation relates the surface temperature to the saturation pressure of the fuel [20].

The hydrocarbon spill surface temperature is attainable by deriving the mass flux and knowing the heat of vaporization and net (convective and radiative) flux to the pool surface and conduction into the liquid phase beneath the surface. The rate of temperature change is a conduction of heat into the liquid pool, and is the difference between the incident total heat flux (due to either convection, solar radiation or a pool fire) and the vapor mass flux of the liquid fuel. Very thin volumes may be assumed to have a uniform temperature throughout their thickness, in which case the pool surface temperature is a function of the net heat flux, or identically, the product of the mass loss rate and the heat of vaporization [21].

1.3.2 Modeling Turbulent Dispersion

A number of turbulent dispersion models are already in use by port authorities, research institutions, and the U.S. Coast Guard. The DEnse GAs DISpersion (DEGADIS) model is used to study the dispersion of denser-than-air gases [22]. It predicts the entrainment of these gases by a prevalent atmospheric wind, and has the ability to capture heat and water transfer from the surface on which the dispersion sits, to the gas. DEGADIS is meant for

ground-level gas releases onto flat water or solid surface. The model has been used previously for estimates on hazard-severity based on distances from flammable hydrocarbon fuel masses.

SLAB, developed by Lawrence Livermore National Laboratory, the USAF Engineering and Services Center, and the American Petroleum Institute, also models the dispersion of denser-than-air gases [23]. SLAB treats continuous releases as a steady state plume, and instantaneous releases as transient puffs. Finite dispersions are modeled as steady state plumes in the presence of a fuel source, and treated as a transient puff once that source is deactivated. Transient turbulent models such as the implantation in this study calls into question the accuracy of these simplifications.

Numerical simulation of turbulent flow is limited by the computational cost of the calculation. Spatially and temporally high-resolution simulations must solve Navier-Stokes equations for macro-scale and micro-scale turbulence. Direct Numerical Simulation (DNS) solvers can resolve large and small turbulent eddies, and thus solve the full Navier-Stokes for all details of the flow. However, solving micro (Kolmogorov) - scale turbulence necessitates smaller time and length scales than would be needed if the computation solved its momentum equations for only large turbulent structures; time increments would be reduced by a factor of approximately $Re^{1/2}$, while length scales would require a $Re^{3/4}$ reduction to account for micro-scale turbulence [24]. DNS calculations are thus restricted to low Reynolds number flows, and must be solved on high-end multiple-processor networks that can facilitate the amount of information a full

Navier-Stokes simulation generates. A DNS treatment of the large scale spill vaporization and dispersion as in the present study is currently not plausible, as the largest length scales for the dispersion calculations can exceed 30 meters.

Simplified numerical flow solvers allow users to discern valuable information from an array of turbulent flow problems. These calculations can include modeling of only smaller length scales, or modeling of all of them. The fidelity of the simulation relies on the number of physical models used to estimate Navier-Stokes quantities, and the method by which the Navier-Stokes equations estimate turbulence at the modeled length scales.

Two methodologies persist for lowering the computational cost of simulating turbulent flows: Reynolds-Averaged Navier Stokes (RANS) and Large Eddy Simulation (LES) CFD modeling. RANS modeling constitutes the closure of a time-averaged system of momentum equations by prediction of a Reynolds stress. The form of the modeled Reynolds-averaged momentum flux is analogous to the form of the average molecular momentum flux tensor, and is thus written as:

$$\overline{u_i u_j} = R_{ij} = \frac{2}{3} K \delta_{ij} - \nu_t \left(\frac{\partial \overline{u_i}}{\partial x_j} + \frac{\partial \overline{u_j}}{\partial x_i} \right), \tag{1.1}$$

where K is the turbulent kinetic energy associated with velocity field fluctuations, $\bar{U}$ is the mean velocity of the field, and ν_t is the eddy viscosity. The varying estimates of the last term on the right-hand side constitute a class of eddy viscosity models (EVMs),

utilized in conjunction with kinetic energy and dissipation rate equations to close the RANS equation [25].

RANS modeling has the lowest computational costs relative to DNS and LES methodologies, but suitably has the lowest level of flow detail; by time-averaging the Navier-Stokes equations, all information pertaining to turbulent fluctuations is lost [24] This is an inadequate level of fidelity in the context of the dispersion and combustion models used is the current study, where turbulent fluctuations are critical for transport of large structures rich in fuel vapor. Although the problem would not need the accuracy on the smallest turbulence length scales, the study of large-scale flow structures does necessitate an intermediate numerical resolution.

Large Eddy Simulations (LES) apply spatial averaging (filtering) techniques for suitably small scales of turbulent motion in a velocity field, while exactly computing large scales of motion using the Navier-Stokes equations. The resolving of these subgrid scales and direct numerical computation of larger scales distinguishes LES numerical simulations from the less accurate RANS models and exact Direct Numerical Simulations, which fully solve all scales of turbulent motion with the Navier Stokes equations [25].

LES determines which size turbulent fluctuations to resolve and which to model by defining a cutoff length scale Δ, which is different from Δ in equations 1.1 and 1.2. The cut-off length scale Δ is a grid-dependent LES parameter whose length is on the order of a grid cell's (i.e. Δx, Δy, and $\Delta z \sim \Delta$). Turbulent fluctuations having length scales larger

than Δ occur in a turbulent kinetic energy (TKE) production zone, where it is assumed turbulent kinetic energy is generated; these turbulent structures would be calculated directly, as in the case of DNS. Turbulent kinetic energy is then redistributed to smaller turbulent structures in an inertial TKE zone, and finally dissipated at the smallest eddy length scales, at which the simulated flow is modeled. The magnitude of the cut-off length scale is very small compared to that of the largest turbulent eddies.

A set of spatially averaged Navier-Stokes equations is used to filter out small (subgrid) scale turbulent fluctuations, and then model those filtered scales with physical relationships. This is accomplished by decomposing the variable quantity (in the case of the momentum equation, the flow field velocities u_i and u_j) into its grid-resolved and subgrid scale components:

$$q(\vec{x},t) = \widetilde{q}(\vec{x},t) + q''(\vec{x},t)\,, \tag{1.2}$$

where q is a scalar variable quantity and the second term on the right-hand side of equation 1.2 is the subgrid scale turbulent fluctuation of the decomposed quantity.

The first term on the right-hand side of equation 1.2 is the spatially-averaged and grid-resolved component of the decomposed quantity. The overhead tilde indicates that variable density is accounted for in the averaging process, a method known as Favre statistical decomposition; it is necessitated by the use of compressible flow conservation equations. The grid-resolved component of the turbulent flow is thus averaged:

$$\tilde{q}(\vec{x},t) = \frac{\overline{\rho q}}{\overline{\rho}} = \frac{\iiint_{\Omega} G_{\Delta}(\vec{x}-\vec{\xi})\rho(\vec{\xi},t)q(\vec{\xi},t)d\vec{\xi}}{\iiint_{\Omega} G_{\Delta}(\vec{x}-\vec{\xi})\rho(\vec{\xi},t)d\vec{\xi}} \tag{1.3}$$

The numerator and denominator in equation 1.3 are volume integrals with limits -in the x, y, and z directions- of (-)Δ/2 and (+)Δ/2. The term $G_{\Delta}(\vec{x}-\vec{\xi})$ is representative of a "filtering kernel", whose form governs how the turbulent flow quantity is resolved on the numerical grid [24]. The software used in the present study utilizes a top hat filter type, which has a magnitude of (1/Δ) in the x, y, or z direction. When utilized for three dimensional simulations, the size of the filter is the product of the one-dimensional kernels, equaling $1/\Delta^3$. The dummy variable $\vec{\xi}$ represents the distance over which the grid-resolved component is being integrated. Given this information, the numerator in equation 1.3 can be written as:

$$\overline{\rho q}(x,y,z,t) = \frac{1}{\Delta^3}\int_{x-\Delta/2}^{x+\Delta/2}\int_{y-\Delta/2}^{y+\Delta/2}\int_{z-\Delta/2}^{z+\Delta/2}\rho(x',y',z',t)q(x',y',z',t)dx'dy'dz' \tag{1.4}$$

The denominator of equation 1.3 can be similarly expressed:

$$\overline{\rho}(x,y,z,t) = \frac{1}{\Delta^3}\int_{x-\Delta/2}^{x+\Delta/2}\int_{y-\Delta/2}^{y+\Delta/2}\int_{z-\Delta/2}^{z+\Delta/2}\rho(x',y',z',t)dx'dy'dz' \tag{1.5}$$

Filtering the Navier-Stokes equation with Favre weight averaging results in a spatially averaged set of momentum equations of the form:

$$\frac{\partial}{\partial t}\left(\overline{\rho}\widetilde{u}_i\right)+\frac{\partial}{\partial x_j}\left(\overline{\rho}\widetilde{u}_i\widetilde{u}_j\right)=-\frac{\partial T_{ij}}{\partial x_j}-\frac{\partial \overline{p}}{\partial x_i}+\frac{\partial \overline{\tau}_{ij}}{\partial x_j}+\overline{\rho}g_i$$
$$T_{ij}=\overline{\rho u_i u_j}-\overline{\rho}\widetilde{u}_i\widetilde{u}_j \tag{1.6}$$

The viscous stress tensor $\overline{\tau}_{ij}$ found in the LES-filtered Navier-Stokes equations requires a model for viscosity, as a result of the removal of the subgrid-scale turbulent structures. Smagorinsky developed a subgrid model for viscosity dependent on the cutoff length scale Δ, as well as the deformation tensor. This Smagorinsky turbulent viscosity is shown in equation 1.7 as [26]:

$$\mu_{LES}=\rho(C_S\Delta)^2\left(2\widetilde{S}_{ij}\cdot\widetilde{S}_{ij}-\frac{2}{3}\left(\nabla\cdot\widetilde{u}_k\right)^2\right)^{1/2} \tag{1.7}$$

The term C_S is known as the Smagorinsky Constant. Values of C_S from .065 to .2 have been calculated, depending on the type of flow being approximated [24]. $\widetilde{S}_{ij}$ is the filtered deformation tensor and has the form:

$$\widetilde{S}_{ij}=\frac{1}{2}\left(\frac{\partial\widetilde{u}_i}{\partial x_j}+\frac{\partial\widetilde{u}_j}{\partial x_i}\right) \tag{1.8}$$

The need to resolve large turbulent structures while balancing computational cost leaves LES the most desirable computing method for the current study.

1.4 Fire Dynamic Simulator (FDS)

All dispersion and combustion calculations for the current work were performed by the Fire Dynamic Simulator, a computational fluid dynamics model developed by NIST [27]. FDS can evaluate numerous fuel dispersion, fire, smoke and heat transport scenarios. The Navier Stokes formulation in FDS is most suited for modeling low Mach number flows driven by thermal convection, and is solved for on a rectilinear grid in three dimensions. The program's hydrodynamic algorithms reflect the solution space for low-speed thermally driven flows, and utilizes either DNS or LES methodology to compute mass, momentum, energy, and species transport at discrete time steps in each grid cell. The hydrodynamic model utilizes a second order predictor-corrector finite difference scheme to solve its conservation equations. Application of either the DNS or LES functionality depends on criteria including physical size of the domain, the size and range of the turbulent length scales, and whether combustion or non-combustion tests are desired.

For the present study, flow features, the domain, and rectilinear objects placed in the domain are on the order of tens of meters in size. This necessitates a LES implementation to capture the features of the large scale dispersion and subsequent combustion.

The most recent publicly released FDS version (FDS 4), can model low-Mach number (< .3) transport and combustion products, radiative and convective heat transfer, pyrolysis, flame spread and the spread of fire throughout the FDS environment, as well as fire prevention methods like smoke detection and suppression by water. FDS calculates various species, heat transfer, and flow outputs. Users can prescribe relevant gas phase

quantities for FDS to record in output files, including but not limited to gas temperature, velocity and species concentrations, density, pressure, and fuel mixture fraction. Heat flux and temperature information can be obtained from simulation domain surfaces.

FDS modeling capabilities are limited due to simplifications in the conservation equation formulations, specialized to most effectively solve fire-related scenarios. As stated previously, low Mach number Navier Stokes equations are ideal for analyzing low-speed flows and heat transfer due to fires. This specialization prevents accurate modeling for high-speed gas flows where compressibility can play a significant role. In particular for the current (choked flow nozzles, detonations, *et cetera*).

Because FDS relies on structured rectilinear meshes, the code has difficulty for implementation in problems where objects in the simulation space are non-rectilinear. Curved surfaces must be approximated by discrete rectilinear slices, generating a 'saw-tooth' effect that becomes more pronounced on course grids. Further discrepancies between the model's predicted results and empirical observations arise if FDS is allowed to predict the heat release rate in a simulation. User-prescribed heat release rates are known quantities due to studies of industrial-scale fires. The accuracy of FDS-predicted heat release is diminished by using a simplified Navier Stokes, radiation and combustion relationships, and the difficulty in duplicating real material and fuel properties.

1.5 Objectives and Approaches

The model in the present study will account for the vaporization of the spilled hydrocarbon fuel, its subsequent vapor dispersion, as well as its possible ignition and deflagration. It is assumed that an atmospheric wind propagates throughout the simulation domain and promotes turbulent mixing in the gas cloud as the flow passes around the structure and over the vaporizing hydrocarbon pool. The liquid spill is first approximated as a having steady-state behavior, so that the pool's vaporization rate equals the rate of hydrocarbon liquid injection; the pool size remains constant. As alluded previously, the study of large-scale chemical spills on water is motivated by the possibility of terrorist attack in or near American sea ports, and by extension, the necessity of harbor safety.

FDS provides the means to simulate the chemical spill problem on water by using assumptions that simplify the vaporization mechanisms. In addition to its combustion capabilities, FDS allows users to implement; mass fluxes from isothermal planar surfaces (such as a cryogenic pool); atmospheric winds; as well as rectilinear objects that can represent cargo tankers. By modeling the problem through FDS and simplifying assumptions, a list of objectives are identified for the present study:

- Implementation of a pool vaporization model for a cryogenic pool on a isothermal surface and the injection of mass flux that is calculated from heat transfer principles

- Visualization of vapor dispersion when subjected to air flow around a prismatic body, and the change in the behavior of dispersion with respect to varying wind speeds
- Implementation of diagnostics that demonstrate time scales for volume-averaged flammable mass and fuel mass fractions, during vapor dispersions
- Determination of the risk of ignition sources for a premixed fuel mass that transitions into a non-premixed (diffusion flame) combustion event.
- Analysis of heat release rate to determine likelihood of transition from premixed flame to diffusion
- Comparison of predicted non-premixed flame height to the flame height calculated by the FDS pool model
- Analysis of incident heat flux diagnostics located downstream of the diffusion flame in order to assess health risks in the vicinity of the fire

The accomplishments towards these objectives will be laid out in the following chapters. Chapter 2 will outline the physical and computer models employed to facilitate vaporization, dispersion, and combustion calculations. Chapter 3 will outline the parameters of the dispersion test, including the pool size, simulation domain size, the temperature and mass flux of methane from the pool, and prevailing wind conditions. Dispersion time scales and flammable mass are graphically illustrated. Chapter 4 discusses the parameters of the subsequent combustion test. Heat release rate, flame height, and radiant flux results are presented. The appendices are related to; the input parameter files for the computer model and the affiliated source code; directions for

implementing a multiple-processor network that facilitates parallel processing; and plots verifying the relationship between the density, temperature, and the mixture fraction of the methane dispersion.

CHAPTER 2 – MODELING TECHNIQUES

2.1 Spill Modeling

The fidelity of the methane pool model relies on the accuracy of components governing its spread, vaporization, cloud dispersion, and combustion. Pool models can characterize transient and steady state spreading behavior. Vaporization models must consider the mass flux of methane gas from the pool due to heat transfer, and which heat transfer mode dominates for the specific problem being studied. Prevailing wind conditions will affect the degree that airborne fuel mass is mixed, as well as its degree of flammability.

2.1.1 Transient Spill Modeling

Dynamic spill models employing the shallow-water (SWE, or shallow-layer) method utilize a set of conservation equations that solve for variables in lateral directions, which are assumed to be much greater than vertical length scales. There is decreased computational cost relative to full Navier-Stokes numerical models, attributable to the ability to model shallow currents with comparatively large length scales. Equations 2.1 and 2.2 provide a generalized SWE formulation [28].

$$\frac{\partial h}{\partial t} + \frac{\partial (hu)}{\partial x} = \frac{\dot{m}_{spill}}{\rho} - \frac{\dot{m}_{vap}}{\rho} \tag{2.1}$$

$$\frac{\partial (uh)}{\partial t} + \frac{\partial (hu^2)}{\partial x} = \frac{\tau_{air}}{\rho} + \frac{\tau_{surf}}{\rho} - hg' \frac{dh}{dx} - \frac{\sigma}{\rho} h \frac{\partial}{\partial x} \left(\frac{\frac{\partial^2 h}{\partial x^2}}{\left[1 + \left(\frac{\partial h}{\partial x} \right)^2 \right]^{3/2}} \right) \tag{2.2}$$

Equation 2.1 is a one-dimensional constant density mass conservation equation. Equation 2.2 is the u-velocity component of the momentum equation, and accounts for the forces acting to impel or inhibit pool spreading. Spreading in the y-direction would necessitate a third equation which governs the momentum in that direction, as well as additional terms in equations 2.1 and 2.2 so as to account for the velocity component *v*.

The shallow-water approach can be difficult to implement without a high-order numerical difference solver. The solution to the SWE must capture the propagation of the modeled spill front across a surface; the boundary between the front and the ground entails nondimensionalization of the numerical shallow water equations so as to avoid singularities at this dry/wet bed interface. The dry bed is sometimes artificially 'wetted' with a thin coat of the spilled liquid to avoid having to normalize the SWE, though errors are incurred that increase in severity with the depth of the wetting [29]. Despite these difficulties the appropriate temporal and spatial numerical difference methods make SWE ideal for scenarios in which fluids of different densities share an interface, as in the case of a spreading chemical spill undercutting the air above it.

In equations 2.1 and 2.2, *h* is the local vertical height of the spill pool in the z-direction. Any modeling of spill propagation across the water must account for the balance of spreading and retarding forces. Additionally, time scales such as spill duration, and quantities such as the volume of the spill, determine which forces feature prominently in the behavior of the spreading pool [18]:

1) Gravity Force – Floating layers of the spilled liquid have an elevated height as they are introduced to the water surface, providing the spill with potential energy due to gravity. The spill height above the water, the difference in water and spill densities, gravity, and a length scale associated with the lateral spread of the pool, result in a pressure gradient that propagates the liquid across the water surface. Gravity potential is represented by the $hg'\frac{dh}{dx}$ term in equation 2.2, where h is the height of the spill above the water and $\frac{dh}{dx}$ is the gradient of h with respect to the later distance x.

2) Inertial Force – As the chemical spreads across the water, the loss in gravity potential energy results in an increase of kinetic energy.

3) Viscous Force – Spill propagation is also arrested by the spill and water viscous forces. The loss in gravity potential or surface tension would be balanced by an internal energy increase due to viscosity. In equation 2.2, $\frac{\tau_{air}}{\rho}$ and $\frac{\tau_{surf}}{\rho}$ are shear forces that account for the energy lost at the air-fuel and water-fuel interfaces, respectively.

4) Surface Tension –A spilled liquid chemical spreading across the water results in a loss of surface tension energy between the water and the air above it. Air-chemical and chemical-water interfaces replace the singular air-water interface as the spill propagates. The change in surface tension energy is negative, and its effect is accounted for by the last term on the right-hand side of equation 2.2. Surface tension-dominated spreading is associated with very long time scales and small inertial forces and spill volumes [18].

Velocity components u is derived by normalizing the momentum equations by h. It can be seen from equation 2.2 that doing so for a very small (or zero-value) spill height would calculate velocities that increase without bound. This leads to significant numerical difficulties and remains a hindrance in dimensionalized CFD shallow-water modeling of dry/wet bed interfaces.

2.1.2 Steady-State Spill Modeling

Fay proceeds to a force magnitude analysis where the relative significance of each spreading and retarding force is estimated for varying time and length scales. By setting the magnitude terms for gravitational and surface tensions forces equal, [18] Fay obtains:

$$h_c = \sqrt{\sigma / \Delta\rho g} \tag{2.3}$$

Where h_c is a critical thickness of the spill and dictates the dominant propagation force, σ represents net surface tension, g is the gravitational acceleration, and $\Delta\rho$ is the net density change in the spilled chemical and water; values of the spread height greater than h_c indicate that gravity potential is the primary spreading force, whereas heights lower than h_c correspond to a surface tension-dominated spreading regime.

By setting the retarding inertial and viscous forces equal, Fay determined that inertia forces are dominant at small length scales and short time scales. As the spill duration increases, the inertial force diminishes by $t^{1/2}$ and $r^{1/2}$, where t and r are the time and radial distance of the spill. From the relationships between retarding and propagating

forces, Fay derives three regimes that govern the spread of a chemical release (Table 1). Gravity-inertial spread/retardation is applicable in short length and time scales, and is independent of chemical's viscosity. Spread under the influence of gravity potential propagation and viscous arrest is the intermediate phase. When the spill height reaches the critical thickness h_c, spill propagation is dominated entirely by the net surface tension; whereas spill retardation remains a function of viscosity. The surface tension-viscous regime is independent of the spill volume. The Δ term in the length scale column of Table 1 is a non-dimensional density term [19], and is given as:

$$\Delta = \frac{\rho_{water} - \rho_{fuel}}{\rho_{water}} \tag{2.4}$$

Spreading Regime	Driving Force	Impeding Force	Magnitude Analysis for length scale (x = …)
Gravitational-Inertial	Potential energy due to pool height, results in horizontal pressure gradient	Inertia of ambient water	$(\Delta g V t^2)^{1/4}$
Gravitational-Viscous	Potential energy due to pool height, results in horizontal pressure gradient	Viscosity of hydrocarbon fuel	$(\Delta g V^2 t^{3/2}/\nu^{1/2})^{1/6}$
Surface Tension-Viscous	Interfacial tension at edge of spill	Viscosity of hydrocarbon fuel	$(\sigma t^3/\rho^{1/2}\nu)^{1/4}$

Table 1: Fay Modeling Spill Regimes

Fay has conducted more recent studies whereby fluid mechanics and empirical observations determined analytical and numerical equations simulating spill dynamics from a breach in hydrocarbon tankers [19]. The dimensions of the ship tanker and the tanker breach – such as the volume of the cargo fluid in the vessel, the hydrostatic head of the cargo fluid above the water, and the area of the rupture in the hull- determine the volume discharge characteristics of the fluid as well as the spreading characteristics of the pool on the water. Fay establishes two limiting pool sizes; very small rupture areas lead to a hydrocarbon pool evaporation rate equal to the discharge rate of the cargo from the hold; large pools result from very large breaches (such as those seen in intentional LNG spill scenarios) where the hydrocarbon fuel is instantaneously discharged.

Dimensionless analytical models for very large and very small rupture areas are derived from equations governing the height of the hydrocarbon fuel on the water, and the rate change of volume and area of the pool, which is assumed to be semicircular. Pool spread behavior for intermediate hull rupture areas was determined numerically. Only large spill volumes were considered, and examples of LNG pool behavior provided by Fay are analogous to instantaneous breaching spill propagation. A magnitude analysis of the spreading and retardation forces listed in Table 2 indicate length scales only in the gravity-inertia regime for large pool volumes (and thus pool areas).

Fay utilizes his analytical and numerical equations in modeling a LNG tanker pool fire, where a hydrocarbon volume of 14,300 m^2 is spilled onto water. The numerical model assumes no vapor cloud dispersion due to the likelihood that a hydrocarbon spill of this

size would be introduced to various ignition sources at the onset of the breaching incident. Incident heat fluxes are calculated from a fraction of the heat release rate and the distance from the center of the pool fire. From the dimensions appropriated to the cargo tank volume and hull breach area, Fay calculates a radiative heat flux of 5 Kw/m^2 nearly 2 kilometers from the spill origin.

2.2 Vaporization and Dispersion Modeling

The boundary conditions of the simulated pool must be determined so as to sufficiently account for the influx of mass due to the vaporization of the cryogenic spill on water. This entails an appropriate description of the vapor flux of the hydrocarbon, which is controlled primarily by the heat transfer behavior between the spill and the water beneath it [17]. FDS is capable of providing an inflow of mass into its simulation domain by delineating an area with prescribed mass flux and isothermal properties. This area will represent the cryogenic pool, and will have a specified mass flow and temperature [26]. This approximation is deemed reasonable because the dominant heat flux from the water to the thin fuel volume causes vaporization.

Subsequent dispersion of the incoming hydrocarbon vapor is calculated using the hydrodynamic equation set in FDS [26]. Navier-Stokes' equations are simplified in FDS to accommodate the low Mach number, buoyancy-driven flows found in fire scenarios; this also reduces the computational cost that arises from a full Navier-Stokes calculation.

2.3 Representative Problem and Boundary Condition

The cryogenic pool in the current study is modeled as a flat, isothermal surface sitting atop a vast, flat, and isothermal heat source representing the quiescent water of a harbor. The primary heat transfer sources into the liquid hydrocarbon spill are; the heat flux from the water directly below the spill due to the temperature difference between the water and the super-cooled liquid; and the total convective and radiative feedback of a diffusion flame pool fire, which would follow in the event of a successful vapor cloud ignition. Air convection along with solar and long-wave radiation also contribute to heating the pool, although the energy input from these modes of heat transfer is small relative to the water and fire sources [16, 17, 21]. The pool is shown in Figure 2.

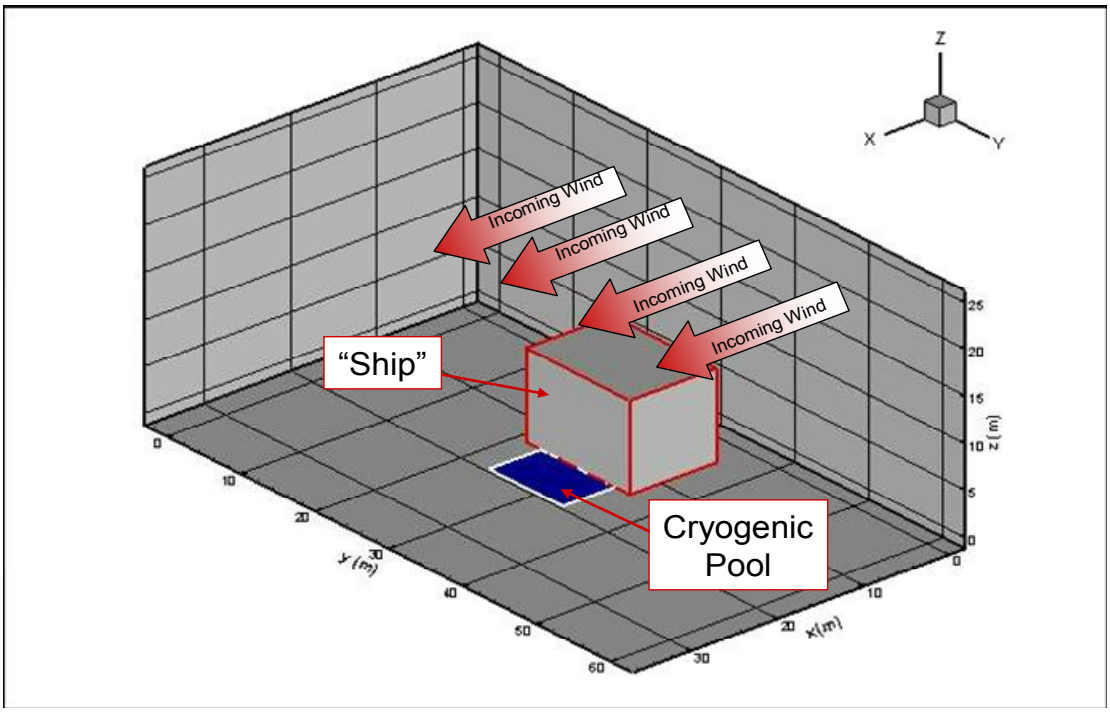

Figure 2: Visualization of the Pool Model As It Appears in Tecplot

It is assumed that the LNG is stored in the seafaring vessel under atmospheric pressure at its atmospheric pressure boiling point. When spilled onto the surface of the water, a convective heat transfer, driven by the temperature difference between the fuel and the water, causes the hydrocarbon to boil off into the atmosphere. Due to the fact that the spill is already at its boiling point temperature, additional heat added to the system drives a mass flux of vapor away from the pool. The mass flow rate of vapor driven away from the pool by the heat loading is dependent on the liquid heat of vaporization. Convection provides the dominant mechanism for transport of the fuel vapor away from the surface. In the absence of radiation heat transfer from the pool, the energy balance is given by:

$$\dot{q}''_{vap} = \dot{m}''_{vap}\Delta h_{fg} = h_{T,w}(T_w - T) \tag{2.5}$$

where $\dot{m}''_{vap}$ [kg/m^2/s] represents the mass flux of a gaseous hydrocarbon vaporizing from the liquid spill in SI units of kg/m^2/s, and Δh_{fg} [J/kg] is the enthalpy needed to change from a liquid to a gaseous state. The convective heat transfer coefficient is given by $h_{T,w}$[W/m^2/K], while T_w and T represent the temperature of the water and isothermal temperature of the cryogenic liquid spill, respectively [16, 17]. The heat loss due to the incoming heat flux, $\dot{q}''_{vap}$, has units of W/m^2. It is assumed that water temperature is maintained at 20 °C, while LNG is shipped at its atmospheric boiling point, -162.2 °C.

The convection through the water-spill interface would cause an increase in the hydrocarbon temperature; the assumption of an isothermal spill is maintained by the fact that new LNG at the boiling point temperature is continuously injected, counteracting the

rise in pool temperature [30]. Ice formation on the water surface has been postulated due to the heat transfer derived from the difference in water and cryogen temperature [17]. However, unconfined water surfaces should posses enough thermal inertia, and the spread of the hydrocarbon spill should produce enough interfacial turbulence, to prevent ice formation. Empirical evidence of ice formation emanates from experiments involving confined and shallow water tanks, unlike the present study's harbor scenario.

The coefficient $h_{T,w}$ is assumed to be a constant in the present study, where its value depends on the boiling regime of the cryogenic liquid on the water. Liquid methane boils on water with a superheat ($\Delta T = T_w - T$) of approximately 190 K. This is above the 161 K minimum point (or Leidenfrost) temperature required for the transition to a film boiling regime [17]. Additionally, the temperature and composition of the pool would remain constant despite vaporization and heating, due to the constant introduction of fresh liquid methane [30]; the Leidenfrost temperature would not change.

The mass flux from the spill would increase in the event of cloud ignition, as the ensuing diffusion flame would produce a convective and radiative feedback to the pool, $\dot{q}''_{feedback}$. The energy balance due to both vaporization and radiative heat feedback from the flame is given by equation 2.6:

$$\dot{q}''_{vap} = \dot{m}''_{vap}\Delta h_{fg} = h_T(T_w - T) + \dot{q}''_{feedback} \tag{2.6}$$

The total flux can be attributed to both heat transfer mechanisms, and when multiplied by the heat of combustion Δh_c [kJ/kg] produce the maximum steady-state heat release rate from the vaporization and combustion:

$$\dot{q}''_{fire} = \dot{m}''_{vap} \Delta h_c \tag{2.7}$$

The total mass flux $\dot{m}''$ has been empirically determined for numerous hydrocarbon fuels, including cryogens such as LNG, LPG, and liquid hydrogen (H_2) [31]. LNG is estimated to have a .078 kg/m^2/s mass flux in the event of a diffusion flame.

The severity and the behavior of the mixing for the fuel and air are largely affected by geometries within the vicinity of the vaporizing pool. As in a number channel flow experiments, the air stream is subjected to a rectangular obstacle (often referred to as a prism or bluff body), around which the flow may exhibit recirculation and vortical structures. For the current study, the air flow over and around the obstruction in the domain is that encountered for low-aspect ratio (cross-stream length to obstacle height) bodies subjected to channel flow. Martinuzzi and Tropea [32] produced a schematic representation of the flow around low-aspect ratio obstacles, which was later diagramed by Krajnović and Davidson [33].

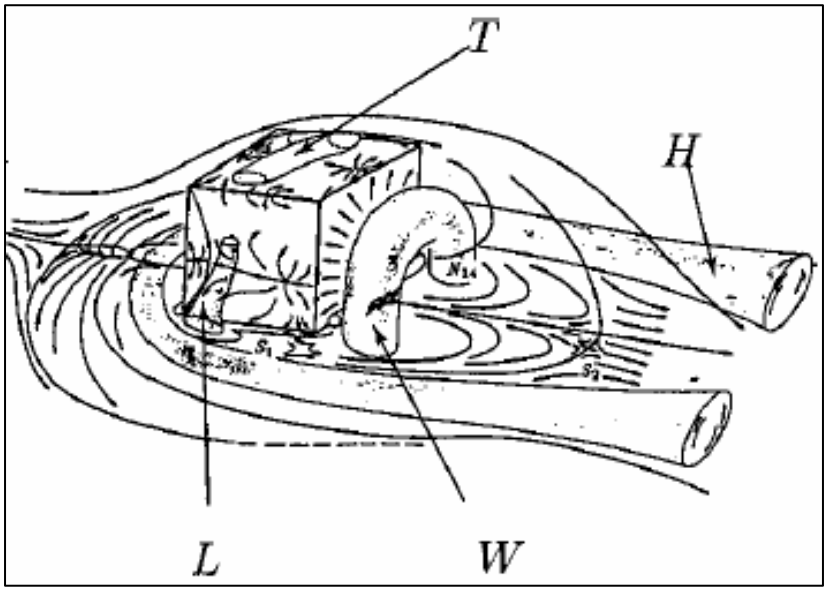

Figure 3: Flow Around a Low-aspect Ratio Obstacle [32, 33]

Figure 3 illustrates the flow around the body for the present problem to exhibit horseshoe (***H***) vortices stemming from the windward side of the obstruction and propagate downstream on either side of the centerline. Vortices are also observed on the sides and atop the obstruction (***L*** and ***T***). For the flow field illustrated in figure 3, a separation should be observed forming from the top of the prism, as well as recirculation back towards the 'ship' along the ground level surface.

Fuel-air mixing is governed by the large-scale turbulent eddies; this can be ascertained by the Reynolds number which, for the present study, is based on the wind velocity, ship height, and dynamic viscosity of air. Re ranges from 3.4×10^5 to 1.4×10^6, and indicate that inertia is the dominant mixing mechanism relative to viscous forces. Kogaki et. al [34] cite a value of 2.2×10^4 as a high Reynolds number for a turbulent flow around a rectangular cylinder; it stands to reason that the three Reynolds numbers calculated for the present study indicate a flow well within the turbulent range.

2.4 Reaction Modeling

The turbulent mixing mechanism discussed in section 2.2.3 facilitates the combustion process by providing a flammable fuel air mixture above the pool. Two burning regimes occur during after ignition; premixed and then non-premixed (diffusion) combustion. In the premixed flame scenario the flammable premixed gas sits above a methane-rich fuel mixture, which in turn is positioned above the fuel source. The amount of premixed flammable mass sitting above the pool depends on the dispersion behavior [35]. When

subjected to an ignition source the cloud burns as a premixed flame. Once all of the premixed reactants are consumed, there is a transition from premixed to diffusion-flame fire behavior where the fuel and air come together from opposite sides of the reaction front. Such a flame is referred to as a pool fire. The pool fire consumes reactants from inside of the flame, and oxygen from outside of the flame. The transition from premixed to non-premixed flames has been an outstanding challenge to computational modelers, and the current work sought to implement a recent method developed by Hu et. al [36].

For large-sale, grid-intensive calculations as in this study, combustion of a hydrocarbon fuel and oxygen is usually modeled as a one-step, global chemical reaction. The LES combustion model in the distributed version of FDS has premixed and diffusion (non-premixed) flame capabilities, but this version cannot model the transition between the two combustion regimes.

Diffusion flame combustion is defined in FDS by a mixture fraction (Z), a conserved scalar quantity that gives the amount of gas in the flow originating from the fuel source:

$$Z = \frac{sY_F - (Y_O - Y_O^\infty)}{sY_F^I + Y_O^\infty}, s = \frac{v_O M_O}{v_F M_F} \tag{2.8}$$

Y_F^I refers to the mass fraction of fuel originating from the fuel stream. Y_O^∞ is the ambient mass fraction of oxygen, while Z_f is the stoichiometric mixture fraction, while v_O and v_F are the oxygen and fuel stoichiometric coefficients, respectively. M_O and M_F are the molecular weights of oxygen and fuel. Mixture fraction combustion models cannot directly calculate the diffusion of the fuel and oxygen reactants, and so assume an infinitely fast reaction.

For diffusion flames, fuel and oxidizer concentrations go to zero at the flame sheet as predicted by the mixture fraction model. The flame surface is identified by the location of the stoichiometric mixture fraction. As Z decreases from its stoichiometric value, the oxidizer mass fraction linearly increases from 0 to its ambient value (this value refers to the mass fraction of oxygen in air, which has an ambient mass fraction of 0.23). The fuel mass fraction linearly increases from 0 at the stoichiometric mixture fraction; the fuel mass fraction is equal to 1 for a mixture fraction of unity, i.e. all of the gas for a unity mixture fraction originates from the fuel source. Products such as carbon dioxide and water are maximized at the flame sheet. Both linearly decrease to 0 as Z goes to 0 or 1. The correlation of product and reactant mass fractions with mixture fraction defines the "state relations" for mixture composition.

The behavior of the mixture fraction can now be interpreted by an equation based on the state relations for oxygen and fuel. The state relations for hydrocarbon fuel and oxygen will respectively be:

$$Y_F(Z) = \begin{cases} 0, Z < Z_f \\ \dfrac{(Z - Z_f)}{1 - Z_f}, Z > Z_f \end{cases}, Y_O(Z) = \begin{cases} Y_O^{\infty}(1 - Z / Z_f), Z < Z_f \\ 0, Z > Z_f \end{cases} \qquad (2.9)$$

As previously stated, the flame sheet model requires that Y_F and Y_O linearly decrease to zero as the mixture fractions approaches its stoichiometric value. We can write Z_f as:

$$Z_f = \frac{Y_O^\infty}{sY_F^I + Y_O^\infty} \tag{2.10}$$

The state relations for combustion products such as nitrogen, carbon dioxide and water, are obtained by relating the mixture fraction to a stoichiometric reaction parameter. This is given as η in the FDS Technical Reference Guide (equation 2.11) [26], and its value ranges from 0 for a region of pure fuel, to infinity for a region of pure oxygen. The parameter η equals 1 when $Z = Z_f$.

$$C_xH_y + \eta(x + y/4)(O_2 + 3.76N_2) \rightarrow \max(0,1-\eta)C_xH_y + \min(1,\eta)xCO_2$$
$$+ \min(1,\eta)(y/2)H_2O + \max(0,\eta-1)(x + y/4)O_2 + \eta(x + y/4)3.76N_2 \tag{2.11}$$

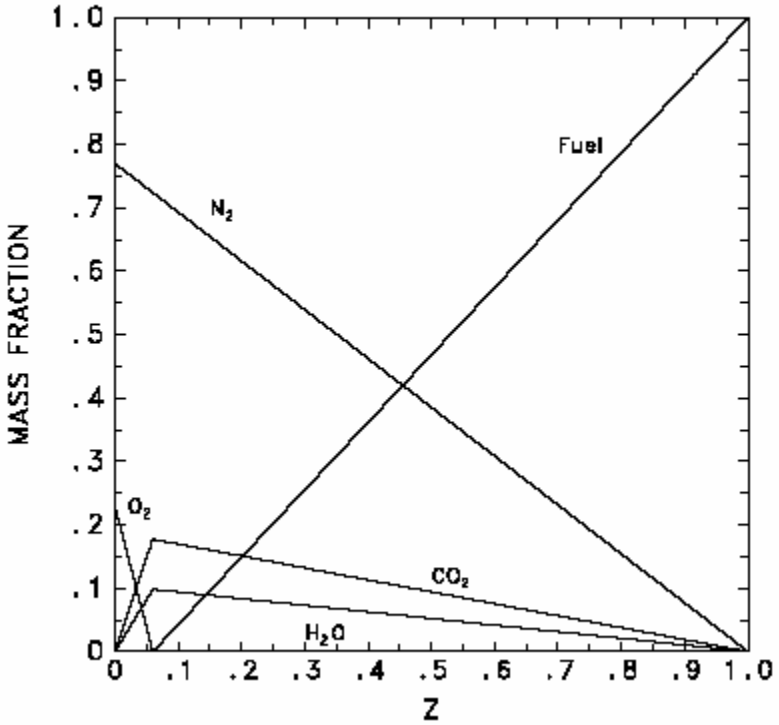

Figure 4: Mass fraction/Mixture fraction relationships for diffusion flame combustion (from FDS Technical Reference Guide [27])

The diffusion flame heat release rate in each computational cell is determined by first assuming that its value is related to the heat release per unit mass of oxygen consumed (ΔH_o) and the mass reaction rate of oxygen consumption:

$$\dot{q}''' = \Delta H_{O_2} \dot{m}_O''' \tag{2.12}$$

Equation 2.12 gives the heat release rate per unit volume for the diffusion flame. The term $\dot{m}_O'''$ is the oxygen mass consumption rate. Hu et. al [36] present a detailed discussion of the FDS combustion model. These terms must undergo spatial filtering so that they are applicable to the LES model utilized in mixture fraction combustion. Burke-Schumann theory provides the expression for the unfiltered fuel mass reaction rate, which is shown in equation 2.13:

$$\dot{m}_F''' = s\dot{m}_O''' = -\left(\frac{Y_F^\infty}{1-Z_f}\right)\left(\frac{1}{2}\rho\chi\right)\delta(Z-Z_f) \tag{2.13}$$

Equation 2.13 has the same units as the volumetric rate of oxygen consumption. The term ρ is the mass density of the gas, while χ represents the scalar dissipation rate:

$$\chi = 2D\left|\nabla Z\right|^2 \tag{2.14}$$

where D is the mass molecular diffusion coefficient with units of m^2/s. The term χ has units of 1/s. The delta function δ is the Krnocker symbol and equal to 0 for all values of Z

different than Z_f, and equal to 1 when $Z = Z_f$. This is in compliance with the infinitely fast chemistry model, in which all reactions occur at the flame sheet, i.e. where there is a stoichiometric mixture fraction. Otherwise, there is no chemical reaction from either the fuel or oxygen reactants.

Hu et. al [36] adopt probability density functions and simplifications for the scalar dissipation rate in order to derive an expression for the LES-filtered volumetric fuel consumption rate, which they give as:

$$\overline{\dot{m}}_F''' = -\left(\frac{Y_F^{\infty}}{1-Z_f}\right)\left(\overline{\rho}\frac{v_t}{Sc_t}\left|\nabla\widetilde{Z}\right|^2\right)\delta(\widetilde{Z}-Z_f) \tag{2.15}$$

Over-bar denotes LES quantities that are arrived at through the use of spatial filtering. Over-tilde (~) quantities are Favre-averaged, i.e., mass-density weighted. The turbulent viscosity (v_t) and the turbulent Schmidt number Sc_t are used to model the LES-filtered scalar dissipation rate χ.

The resulting expressions for the LES-filtered oxygen mass consumption rate and heat release rate per unit volume, are given by equations 2.16 and 2.17:

$$\overline{\dot{m}}_{O_2}''' = -\left(\frac{Y_{O_2}^{\infty}}{Z_f}\right)\left(\overline{\rho}\frac{v_t}{Sc_t}\left|\nabla\widetilde{Z}\right|^2\right)\delta(\widetilde{Z}-Z_f) \tag{2.16}$$

$$\bar{\dot{q}}_d''' = \left(\frac{Y_{O_2}^{\infty}}{Z_f}\right)\left(\bar{\rho}\frac{\nu_t}{Sc_t}\left|\nabla\tilde{Z}\right|^2\right)\delta(\tilde{Z}-Z_f)\times\Delta H_{O_2} \tag{2.17}$$

Williamson et. al [35] have further modified FDS to include a LES turbulent premixed combustion model in addition to the existing non-premixed model. Premixed combustion is essential for modeling ignition and transient combustion in LNG pools; such cases may be subject to flammable proportions of fuel-air mixing. In this case, a deflagration wave would propagate from the ignition source, consuming unburned reactants and leaving burnt combustion products downstream. This propagation is modeled by a reaction progress variable which is traditionally denoted *c*. The reaction progress variable has a value of 0 in fresh reactants, and is equal to 1 in burnt products. The conservation equation used to predict *c* in the FDS combustion model must also be filtered so that it is adequate resolved by the LES grid. This will determine a filtered progress variable $\tilde{c}$.

The conditions that define the value of c in burnt products and unburned reactants allow the progress variable to be expressed in terms of species mass fractions:

$$c = \frac{(Y_F^u - Y_F)}{(Y_F^u - Y_F^b)} = \frac{(Y_{O_2}^u - Y_{O_2})}{(Y_{O_2}^u - Y_{O_2}^b)} = \frac{Y_{CO_2}}{Y_{CO_2}^b} = \frac{Y_{H_2O}}{Y_{H_2O}^b} \tag{2.18}$$

Equation 2.18 assumes that the molecular diffusion coefficients of the reactive species are equal. This is assumed reasonable in high-turbulence flame regions. However, a closure model for molecular diffusion in the governing filtered *c* equation must account

for the increased significance of diffusion in low-turbulence regions; the realizibility condition is that in laminar flow a flame would propagate at the laminar flame speed [35]. The superscript *u* represents the mass fraction of the unburned species, while superscript *b* refers to the burned species mass fraction. From equation 2.18 it is seen that a fuel mass fraction equal to the unburned fuel mass fraction will set the reaction progress variable to 0, while a fuel mass fraction equal to the burned fuel mass fraction results in *c* being equal to 1. This is in keeping with the definition of the reaction progress variable.

The mass fraction relationships are delineated by way of a mass balance equation for the reaction progress variable, given by equation 2.19:

$$\frac{\partial}{\partial t}(\rho c) + \frac{\partial}{\partial x_i}(\rho u_i c) = \frac{\partial}{\partial x_i}(\rho D \frac{\partial c}{\partial x_i}) + \dot{\omega}_c \tag{2.19}$$

The first term on the right-hand side of equation 2.21 is the molecular transport of *c* due to diffusion. The last term on the right-hand side of 2.16, $\dot{\omega}_c$, is the production rate of the reaction progress variable per unit volume (kg/s/m^3). Williamson et. al modify equation 2.19 to its LES-filtered form, suitable for modeling turbulent premixed flames:

$$\frac{\partial}{\partial t}(\overline{\rho}\widetilde{c}) + \frac{\partial}{\partial x_i}(\overline{\rho}\widetilde{u}_i\widetilde{c}) = -\frac{\partial}{\partial x_i}(\overline{\rho u_i c} - \overline{\rho}\widetilde{u}_i\widetilde{c}) + \frac{\partial}{\partial x_i}(\overline{\rho D \frac{\partial c}{\partial x_i}}) + \overline{\dot{\omega}}_c \tag{2.20}$$

The turbulent eddy viscosity concept is used to model the first term on the right-hand side of equation 2.20, representing the convective transport of the filtered reaction progress

variable due to unresolved turbulent fluctuations. Straight LES-filtered values are represented by over-bars; Favre-weighted LES filtering is represented by over-tildes.

The filtered volumetric chemical reaction rate, $\overline{\dot{\omega}}_c$, and the filtered diffusion transport term must also be modeled The production of *c* is a product of the unburned gas density (ρ_u), the laminar flame speed (s_L), and a LES-filtered flame surface-to-volume ratio (Σ):

$$\overline{\dot{\omega}}_c = (\rho_u s_L) \times \Sigma \tag{2.21}$$

where Σ is the flame surface-to-volume and is dependent on a subgrid-scale wrinkling factor greater than or equal to 1, a LES filter size greater than the computational grid cell size, and the filtered progress variable. Σ is equal to zero for values of $\widetilde{c}$ equal to 0 or 1. The molecular transport of the filtered progress variable is modeled by equation 2.22:

$$\overline{\rho D \frac{\partial c}{\partial x_i}} = \frac{\rho_u s_L \Delta_c}{16\sqrt{6/\pi}} \frac{\partial \widetilde{c}}{\partial x_i} \tag{2.22}$$

The term Δ_c represents the thickness of the LES-filtered flame, and is accepted as the computational grid cell size Δ (the grid cell volume to the 1/3 power) multiplied by a factor of 5; this is necessary in order to adequately resolve the thickness of the LES-filtered flame. For this reason, the LES filter size for the flame, Δ_c, is also different from the filter size for LES turbulence flows, which is denoted Δ_u. Setting Δ_u to Δ_c would result in flame calculations with a computational cost 125 times greater than non-

combustion calculations. By decoupling the flame and turbulent flow filter sizes, the progress variable-controlled flame thickness can be adequately resolved for relatively coarse grids in FDS.

When all transport and production models are incorporated into the conservation equation for the filtered progress variable, the following is obtained:

$$\frac{\partial}{\partial t}(\overline{\rho}\widetilde{c}) + \frac{\partial}{\partial x_i}(\overline{\rho}\widetilde{u}_i\widetilde{c}) = \frac{\partial}{\partial x_i}\left(\overline{\rho}\frac{\nu_t}{Sc_t}\frac{\partial \widetilde{c}}{\partial x_i}\right) + \frac{\partial}{\partial x_i}\left(\frac{\rho_u s_L \Delta_c}{16\sqrt{6/\pi}}\frac{\partial \widetilde{c}}{\partial x_i}\right) + (\rho_u s_L)\Xi \times 4\sqrt{\frac{6}{\pi}}\frac{\widetilde{c}(1-\widetilde{c})}{\Delta_c} \qquad (2.23)$$

The right-hand side of equation 2.23 models the convective transport of c due to subgrid-scale turbulence fluctuations, molecular transport of c due to molecular diffusion, and volumetric production of c due to reactions, respectively.

The original diffusion flame model in FDS must be coupled to the premixed combustion modifications, which were not in the released version of FDS 4. This is accomplished by defining the heat release rate per unit volume for premixed combustion, and then using a partially-premixed combustion interface formulation to couple the diffusion flame and premixed combustion heat release rates [37]. The HRR per unit volume of premixed combustion relies on the production of the filtered progress variable due not only to chemical reaction, but also to ignition. To this end, a volumetric production term is added to the right-hand side of equation 2.24, and accounts for a premixed ignition event:

$$\frac{\partial}{\partial t}(\overline{\rho}\widetilde{c}) + \frac{\partial}{\partial x_i}(\overline{\rho}\widetilde{u}_i\widetilde{c}) = \frac{\partial}{\partial x_i}\left(\overline{\rho}\frac{v_t}{Sc_t}\frac{\partial \widetilde{c}}{\partial x_i}\right)$$

$$+ \frac{\partial}{\partial x_i}\left(\frac{\rho_u s_L \Delta_c}{16\sqrt{6/\pi}}\frac{\partial \widetilde{c}}{\partial x_i}\right) + (\rho_u s_L)\Xi \times 4\sqrt{\frac{6}{\pi}}\frac{\widetilde{c}(1-\widetilde{c})}{\Delta_c} + \overline{\dot{\omega}'''_{ign}} \qquad (2.24)$$

The last term on the right hand side of equation 2.24 represents the production of the filtered progress variable due to ignition. Any premixed combustion volumetric heat release relies on the amount of progress variable *c* generated by ignition and chemical reaction, the change in the fuel mass fraction in the transition from unburned to burnt gases, and also the heat of combustion:

$$\overline{\dot{q}'''_p} = (\overline{\dot{\omega}'''_c} + \overline{\dot{\omega}'''_{ign}}) \times (Y_F^u - Y_F^b)\Delta H_F \qquad (2.25)$$

When taking into account the closure model for the chemical production rate (equation 2.21), equation 2.25 becomes:

$$\overline{\dot{q}'''_p} = (4\rho_u s_L \Xi\sqrt{\frac{6}{\pi}}\frac{\widetilde{c}(1-\widetilde{c})}{\Delta_c} + \overline{\dot{\omega}'''_{ign}}) \times (Y_F^u - Y_F^b)\Delta H_F \qquad (2.26)$$

The partially-premixed combustion interface is then used to couple the heat release rates for premixed and diffusion flames. This coupling is based on the flame index concept:

$$FI = \frac{1}{2}\left(\frac{\nabla \widetilde{Y}_F . \nabla \widetilde{Y}_{O_2}}{\left|\nabla \widetilde{Y}_F\right| + \left|\nabla \widetilde{Y}_{O_2}\right|} + 1 \right) \tag{2.27}$$

From this expression, it is evident the flame index is equal to 0 if the unit vector for the filtered fuel ($\nabla \widetilde{Y}_F$) mass fraction gradient is opposed to the unit vector for the filtered oxygen ($\nabla \widetilde{Y}_{O_2}$) mass fraction gradient. This corresponds to the orientation of fuel and oxidizer reactants with respect to a flame sheet during a non-premixed combustion event; it was explained previously that fuel and oxidizer meet at the flame, which is defined by the stoichiometric mixture fraction Z_f. In contrast, the oxygen and fuel gradient unit vectors are mostly aligned in the event of premixed combustion, so that the flame index equals 1. The flame index coupling interface then acts as a weighted coefficient so as to determine the appropriate combustion regime and by extension the correct volumetric heat release rate:

$$\overline{\dot{q}}''' = FI \times \overline{\dot{q}}_p''' + (1 - FI) \times f_{ign} \times \overline{\dot{q}}_d''' \tag{2.28}$$

Notice that the total heat release rate corresponds to premixed combustion when the flame index is equal to 1, and to non-premixed combustion when FI = 0. The ignition factor f_{ign} is instituted to prevent non-premixed heat release due to inert mixing of the fuel and oxidizer [37]. FI also equals 0 during inert mixing scenarios, in order to keep the ignition factor equal to 0. Non-premixed combustion requires f_{ign} = 1. In FDS, the ignition factor has the form of a hyperbolic tangent:

$$f_{ign} = 0.5 + 0.5\tanh((\widetilde{c} - 0.6)/0.05) \tag{2.29}$$

The ignition factor ensures that there is no non-premixed combustion when the filtered reaction progress variable is 0, i.e., during pure mixing or pure premixed combustion scenarios. Both of these cases assume $f_{ign} = 0$.

2.5 Implementation of Models

2.5.1 Input and Model Set-Up

Domain sizes of interest for the current study are contingent on large scales associated with the size of chemical spills on ships, and also the size of the turbulent structures that control the mixing of the fuel and air. Studies for LNG spills investigate intentional breaching events, wherein pool diameters can be as large as 512 meters, and incident radiation is measured from as far as 1920 meters [4]. Pool, obstacle, and domain scales have been reduced from real-world values in the current study in order to facilitate reasonable simulation times.

Long simulation times can be further reduced by utilizing the model's parallel processing capabilities. This is accomplished with the Message Passing Interface (MPI) parallel processing software that is implemented as MPICH for machines with a Windows operating system. MPICH was developed by the Mathematics and Computer Science Division of Argonne National Laboratories [38]. The use of MPI allows a single FDS simulation to be divided into multiple blocks that generate and distribute information to

the other meshes. Computers participating in the simulation are identified by their IP addresses and the number of partitions dedicated to the FDS job. Special care must also be given to each machine's working directory, which, ideally, are identical and house a copy of the compiled FDS executable (see Appendix B.1 for details on the implementation of MPICH2).

Users specify all pertinent information for their simulation through a data file. This includes boundary conditions; the reaction properties (if any) of rectilinear surfaces and objects; vents that act as open doors or windows with mass fluxes, velocities, or heat release rates prescribed to them. The information prescribed in the data file is interpreted by subroutines found in the read.f module of FDS.

2.5.2 Output and Analysis

FDS has diagnostic functionalities that record, among other properties, a simulation's wind and flow velocities, mass densities, temperatures, and heat release rates due either to the influx of vapor or a combustion event. FDS records pertinent information through the use of output, including boundary files, thermocouple files, slice files, and Plot 3D files. The namelist for these outputs gives users access to heat flux and temperature information, heat release rates per unit area and unit volume, density, mixture fraction and wind velocity [27].

Boundary diagnostics provide quantities at the surfaces of solid obstructions. Thermocouple files act as physical thermocouples, in that information can be gathered at

a finite point in the FDS domain. Thermocouple diagnostics also provide surface and volumetric quantities. The example FDS data file in Appendix A.3 defines a thermocouple diagnostic that records the mass flow of methane through a 2 m^2 area normal to the K-Plane. Slice file output provides intrinsic or extrinsic properties in planar sheets for each of the three Cartesian coordinates [27].

Most beneficial to the current work is the plot 3D line, which provides information for selected quantities for every point on the Cartesian grid. Users can manipulate the data using software such as Tecplot to create planar representations of selected quantities (similar to the slice file diagnostic), or iso-surfaces that can be viewed in three dimensions. Images in Chapters 3 and 4 were generated using plot 3D files which were then uploaded into Tecplot [27].

CHAPTER 3 – LNG SPILL/DISPERSION MODELS

3.1 Pool Model

The scenario selected for the present study is derived from that of a breached LNG tanker spilling the cryogenic liquid onto a quiescent water surface of a harbor. As delineated, pool spread and vaporization, the mixing behavior of the cloud are complexities that require sophisticated modeling techniques. In order to understand the basic physics of this complex problem, geometry, mass flow, heat transfer, and dispersion have been idealized for the current study. It is hoped that the results from this simplified model may be applied to future sophisticated models that more accurately duplicate the dynamic behavior of a harbor spill, dispersion and fire.

The computational test space created for the present study is a set of four rectilinear grids that employ the MPICH2 parallel processing software; this is the image in figure 5. The dimensions for the test domain in all cases in this study are 35 x 60 x 25 m^3. The right and left-hand, and upper-center test blocks have grid resolutions (Δ) of .5 meters per cell. The pool -and hence the dispersion calculation- sits in the lower-center (green) mesh, which is resolved at .25 meters per cell. The choice in grid resolution is a compromise between fidelity and speed. The overall height of the domain was chosen so as to adequately capture the calculated maximum height of the predicted diffusion flame pool fire. The stream-wise (x = 0 to 35 meters) and the cross-stream (y = 0 to 60 meters) lengths were selected to accommodate the maximum flammable mass, which was observed from trial dispersion simulations in FDS. To resolve these scales in a

computationally efficient manner, a coarser grid would increase the inaccuracies of many of the diagnostic tools for the current study, such as flame height and the amount of flammable material generated by the injection and dispersion of gas.

The pool is a prescribed in the FDS data file as a `VENT` with a '`Leak`' surface area that injects a mass flux of vapor into the simulation domain. The vaporization rate from the vent is prescribed as a constant mass flux of .05537 kg/s/m^2 emanating from the vent. This boundary condition is derived from equation 2.5, and his based on the constant heat transfer coefficient $h_{T,w}$ discussed in section 2.3. Because FDS requires rectilinear meshes, vents and obstructions cannot be curvilinear, though cornered surfaces or edges can only be approximated by prescribing vents with discreetly different lengths with respect to adjacent vents.

For the sake of simplicity, the pool is rectangular in shape, although this assumption may not be inaccurate; acetone spills downstream from rectangular obstructions were performed by Bohl and Jackson [39], who observed significant lateral spreading along the leeward edge of the prism. The effective diameter for rectangular objects is used anytime a calculation -such as pool fire flame height- calls for a radial dimension.

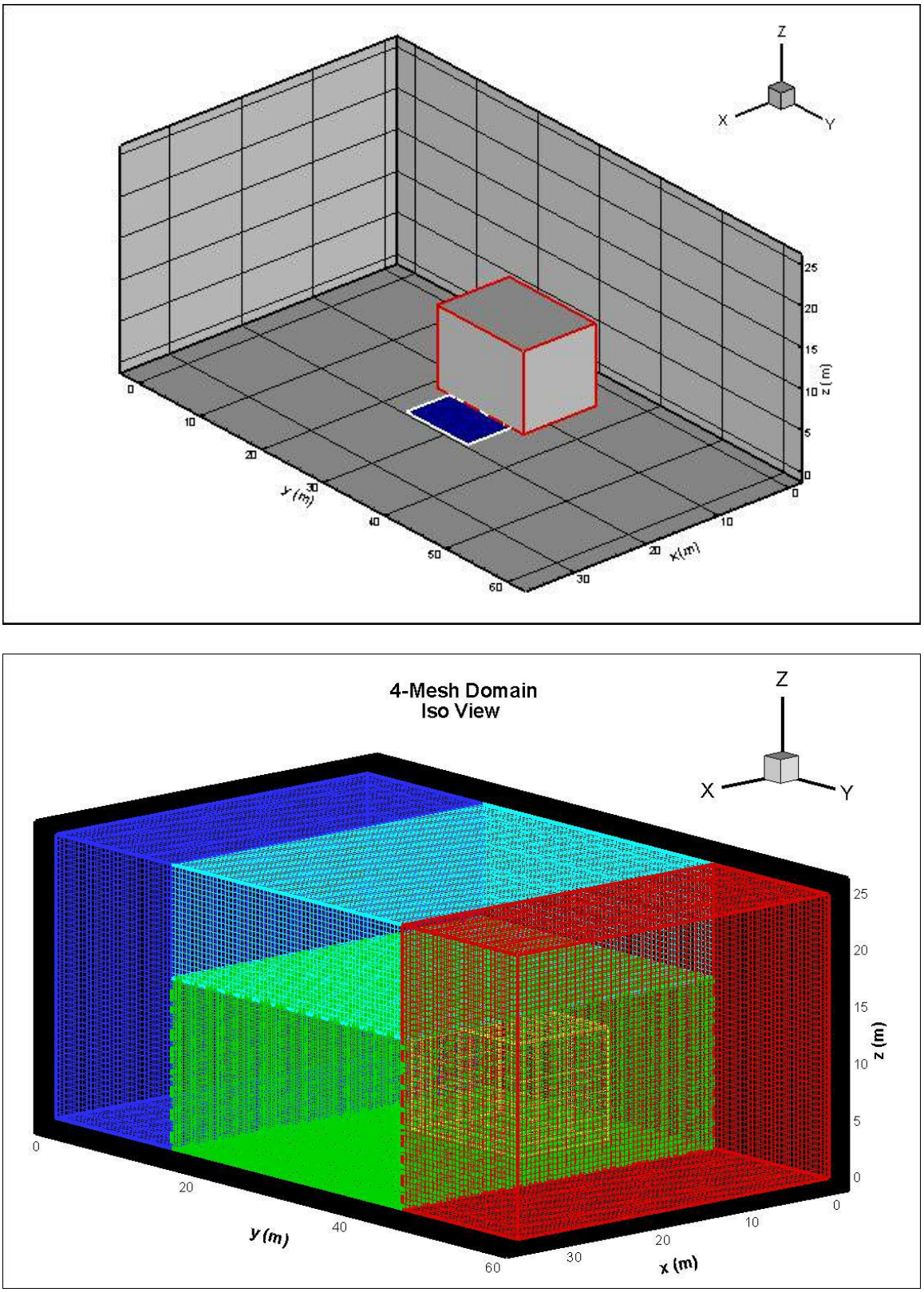

Figure 5: Test Domain geometry (a); and Multiple Block Test Domain to Facilitate Parallel Processing (b)

The ship from which the cryogen issues forth is modeled as a rectilinear obstruction created with the `OBST` feature in the FDS data file. Its dimensions are 10 x 14 x 10 m^3, and sits 5 meters off of the x-axis. The decision to model a low-aspect ratio as opposed to a high-aspect ratio obstruction (LNG tankers are typically 290 to 304 meters long) is a consequence of moderating computational cost while a attempting to capture the basic physics of the flow. For example, a grid resolution of Δ = .25 m/cell and a 300-meter long obstacle would necessitate 9.072 x 10^6 additional cells in the bottom-center mesh alone. The cryogenic spill sits at the base of the obstruction, as would a pool in the event of an actual cargo hold breach.

The pool is leeward of a 0.5, 1.0, or 2.0 m/s atmospheric wind prescribed at one of the simulation boundaries. The pool has a 60 m^2 area, and is positioned so that it is symmetrical with respect to the centerline in the domain.

3.2 FDS Dispersion Results

Three tests are performed during the dispersion phase of the present study. The 0.5, 1.0, and 2.0 m/s wind velocity conditions comprise Cases 1, 2, and 3, respectively. Otherwise, all three cases exhibit identical test conditions. The ambient temperature in the domain is 20 C. A number of diagnostics have been implemented to characterize the dispersion tests. The size of the flammable mass is a determining factor in the strength of an explosion for many commercial codes. Using FDS thermocouple capabilities, flammable mass and fuel mass fraction data is averaged over the volume of the lower-center mesh.

This data can be coupled with subsequent combustion data, and compared to the results of commercial convective-diffusion models. Additionally, the flammable mass and fuel mass diagnostic can be used to determine time scales for when the dispersion has achieved a steady state, predictable behavior. The data is also key in placing probable ignition sources for premixed combustion events. Appendix A.3 is an example data file for the Case 1 (0.5 m/s wind velocity) dispersion, and prescribes the test and diagnostic parameters. This pre-processed data is conditioned through Tecplot to yield relationships between different test outputs.

Mixture fraction iso-surfaces and iso-contours are generated to visualize the shape and size of the flammable cloud, while determining how the wind velocity conditions affect the mixing of the fuel in the domain. Mixture fraction illustrations demonstrate the effect of vortices, and stratification within the cloud. U-Velocity iso-contours visualize vortices on the side and downstream of the obstacle, and delineate recirculation zones; comparison of the flow patterns for different wind speeds is facilitated.

Temperature-mixture fraction scatter plots serve to ensure the correct fuel mass density is being calculated, by way of hand calculations for the weighted average fuel molecular weight and ideal gas law. This and the mixture fraction diagnostics are supplemented with temperature iso-contours; temperature and mixture fraction relationships with respect to position in the simulation domain can be ascertained by correlating these three data visualization tools.

As discussed in section 2.2.1, the value of the spill's mass flux is a function of the temperature difference between the cryogen and the water, the coefficient of convection heat transfer between the cryogen and water, as well as the enthalpy of vaporization. An additional heat source term must be added to the energy balance in the event of a pool fire [21]. Long-wave radiation and air-to-pool convection are very small energy terms with respect to water-to-pool convection and heat feedback from the diffusion flame [17].

The LNG pool is assumed to be pure liquid methane in the current study as the FDS combustion models are more compatible with pure fuels; Conrado and Vesovic [17] state a working composition of 90% methane and 10% ethane. Lehr and Simecek-Beatty [16] assume a 95% methane composition, while Hightower et. al state a 95%-97% methane composition for imported LNG [4]. However, FDS is not well suited for the handling of preferential vaporization of more volatile fuel components, in this case, as discussed by Conrado and Vesovic [17].

If no source is present, the predominant heat transfer mode is the water-to-pool convection, in which case equation 2.3 can be used to derive the mass flux of vapor being driven from the spill. The water is assumed to be an isothermal heat source (20 C) with sufficient thermal inertia and interfacial turbulence with the cryogen to prevent ice formation [17]. LNG would be injected into the pool at its boiling point temperature of -162 C, while the enthalpy of vaporization for pure liquid methane is 509 kJ/kg. The convection coefficient h_T is given by Conrado and Vesovic as approximately .155 kW/m^2/K for both LNG and pure liquid methane [4, 17, 21]. Thus, $\dot{q}''_{vap}$ is calculated to

be 28.21 kW/m^2, calculated from the convection coefficient and ΔT (182 C, K), the difference between the methane boiling temperature and the pool temperature. Dividing $\dot{q}''_{vap}$ by the enthalpy of vaporization yields an approximate mass vaporization flux of .05542 kg/m^2/s. This number is in good agreement with the value for $\dot{m}''_{vap}$ of an LNG spill on water, .05 kg/m^2/s, given by Opschoor [30].

3.2.1 Total Flammable Fuel Mass and Fuel Mass Fraction

FDS thermocouple diagnostics were used to determine time scales at which the methane cloud achieved steady state flammable fuel mass and average fuel mass fraction quantities. A fuel mass fraction is averaged over the volume of the lower-center block in the domain, where the vast majority of the fuel mass is located. Knowledge of the steady state time scale is essential in the placement of the ignition source during the combustion phase of the simulation. The results from the Cases 1-3 have been graphically illustrated and tabulated. Table 2 lists pertinent flammable mass and fuel mass fraction data from the 3 dispersion cases.

The maximum total flammable mass was found to have existed at the 265-second mark during the 0.5 m/s wind velocity dispersion. A maximum flammable fuel mass fraction of 0.160 kg/kg was found at the same time during the Case 1 dispersion. Although Case 1 exhibits the highest peak flammable mass, it falls back to a steady state flammable mass similar to the higher wind velocity Case 2. Table 2, summarizes pertinent flammable mass and time scale data from the three dispersion cases, while figures 6 and 7 demonstrate dispersion results graphically. The information suggests that for higher wind

conditions, the amount of flammable mass surrounding the obstruction decreases. Cases 1 and 2 exhibit very similar flammable fuel mass and fuel mass fractions. There also appear to be shorter steady-state time scales for the flammable mass dispersion of Case 3 relative to the 0.5 and 1.0 m/s wind velocity conditions. Mixture fraction visualization of the flammable mass is illustrated in Chapter 3.

Case #	Steady State Time (s)	Steady State Flammable Mass (kg)	Steady State Fuel Mass Fraction (kg/kg)	Time for Maximum Value (s)	Maximum Flammable Mass (kg)	Maximum Fuel Mass Fraction (kg/kg)
1	300	237	.01463	265	259	.016
2	300	235	.01448	290	247	.0152
3	245	121	.00743	145	130	.00803

Table 2: Time Scales, Mass Fractions, and Fuel Masses for Dispersions 1-3

Case 3 exhibits much lower fuel mass and mass fraction numbers relative to Cases 1 and 2. Steady state values for the 2 m/s wind velocity test are .00743 kg/kg fuel mass fraction, and 121 kg of flammable mass. Steady state was achieved in Case 3 earlier than in the previous two tests, at 245 seconds.

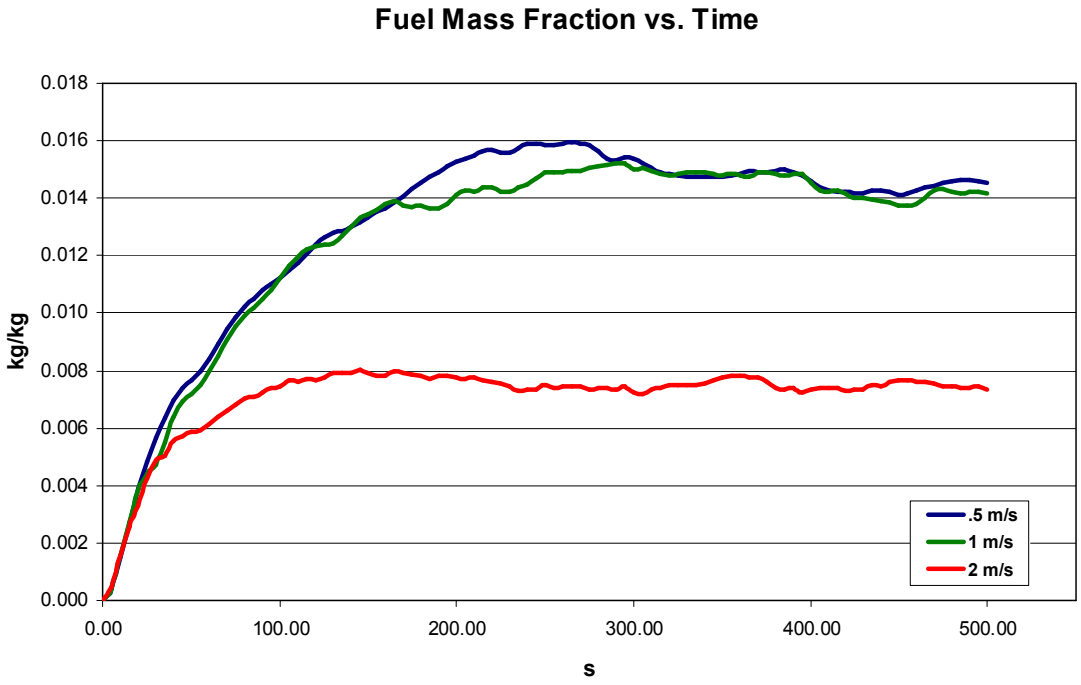

Figure 6: Methane Fuel Mass Fraction Versus Time

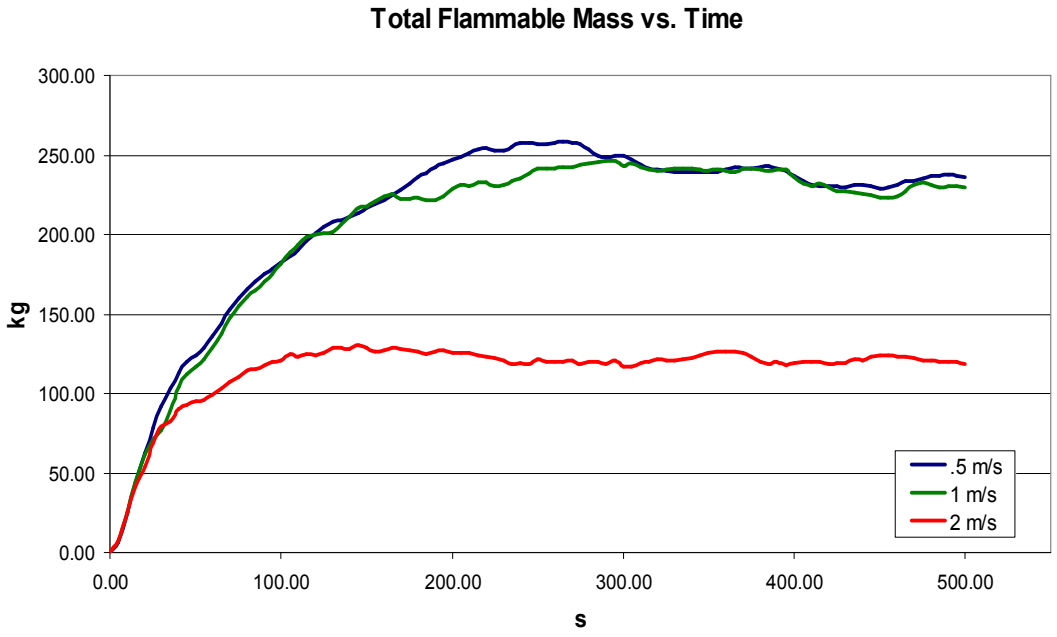

Figure 7: Flammable Mass of Methane Versus Time

3.2.2 Lower Flammability Limit Methane Cloud

The amount of flammable material existing in the test domain can be qualitatively viewed by the constant-mixture fraction methane iso-surfaces. Figures 8 through 10 display the flammable clouds for Cases 1 through 3, whose surfaces represent the extent of the methane dispersion at its lower flammability limit (5% by volume or 0.0288 kg/kg for CH_4). Figures 11 through 13 are 2-dimensional mixture fraction iso-contours for all three cases. The limits of the illustration are the upper and lower flammability limits for methane on a mass ratio basis.

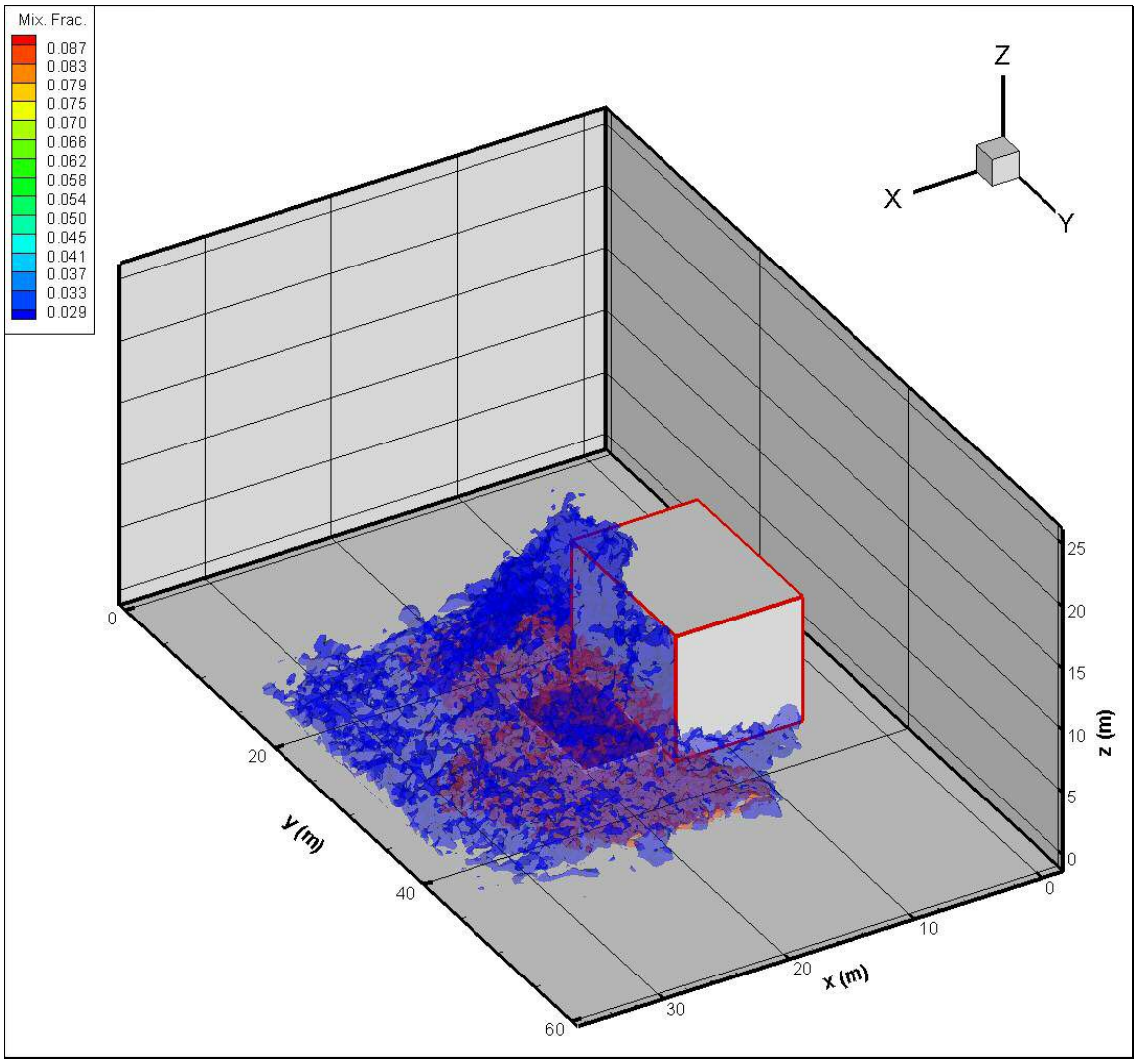

Figure 8: Mixture Fraction Cloud with Lower Flammability Limit Iso-Surface for 0.5 m/s wind velocity

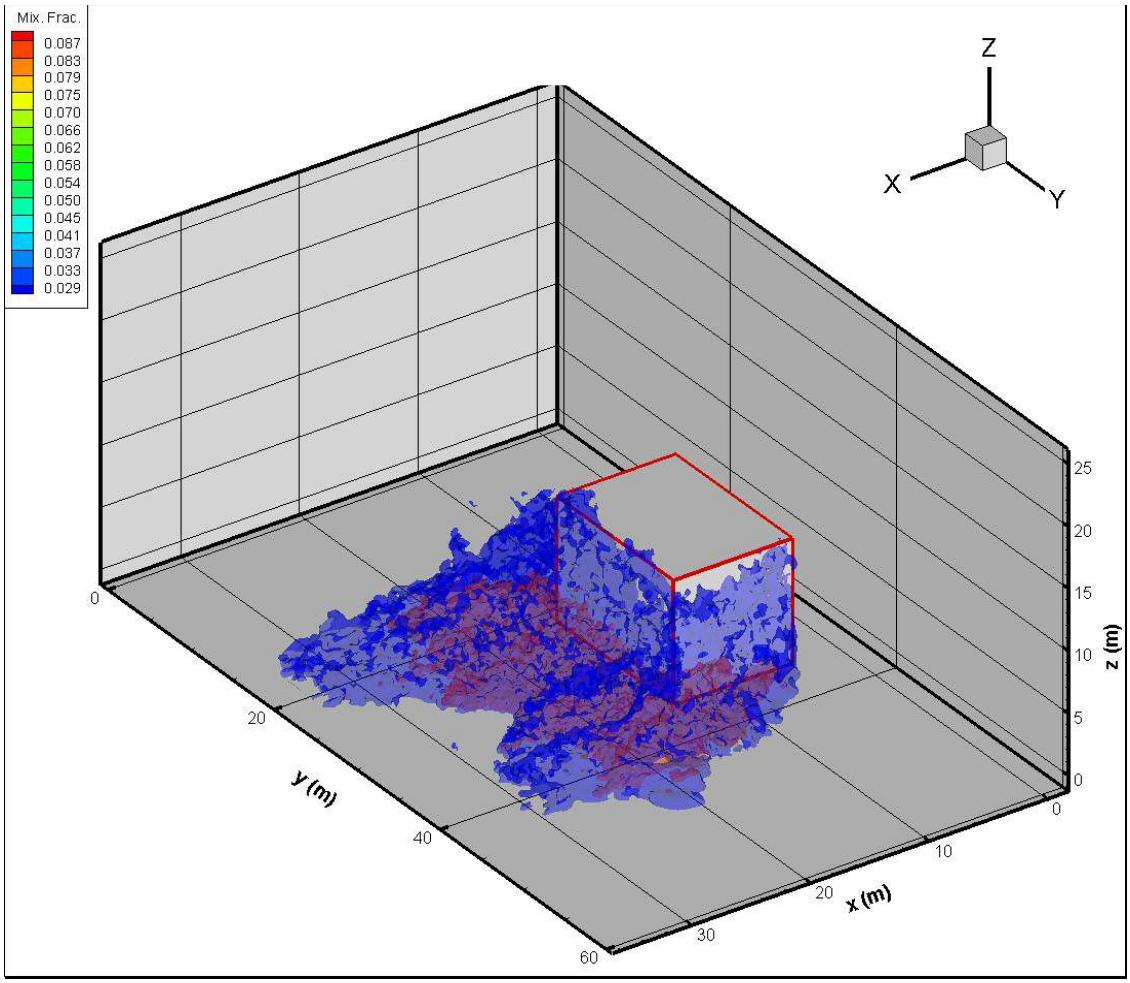

Figure 9: Mixture Fraction Cloud with Lower Flammability Limit Iso-Surface for 1.0 m/s wind velocity

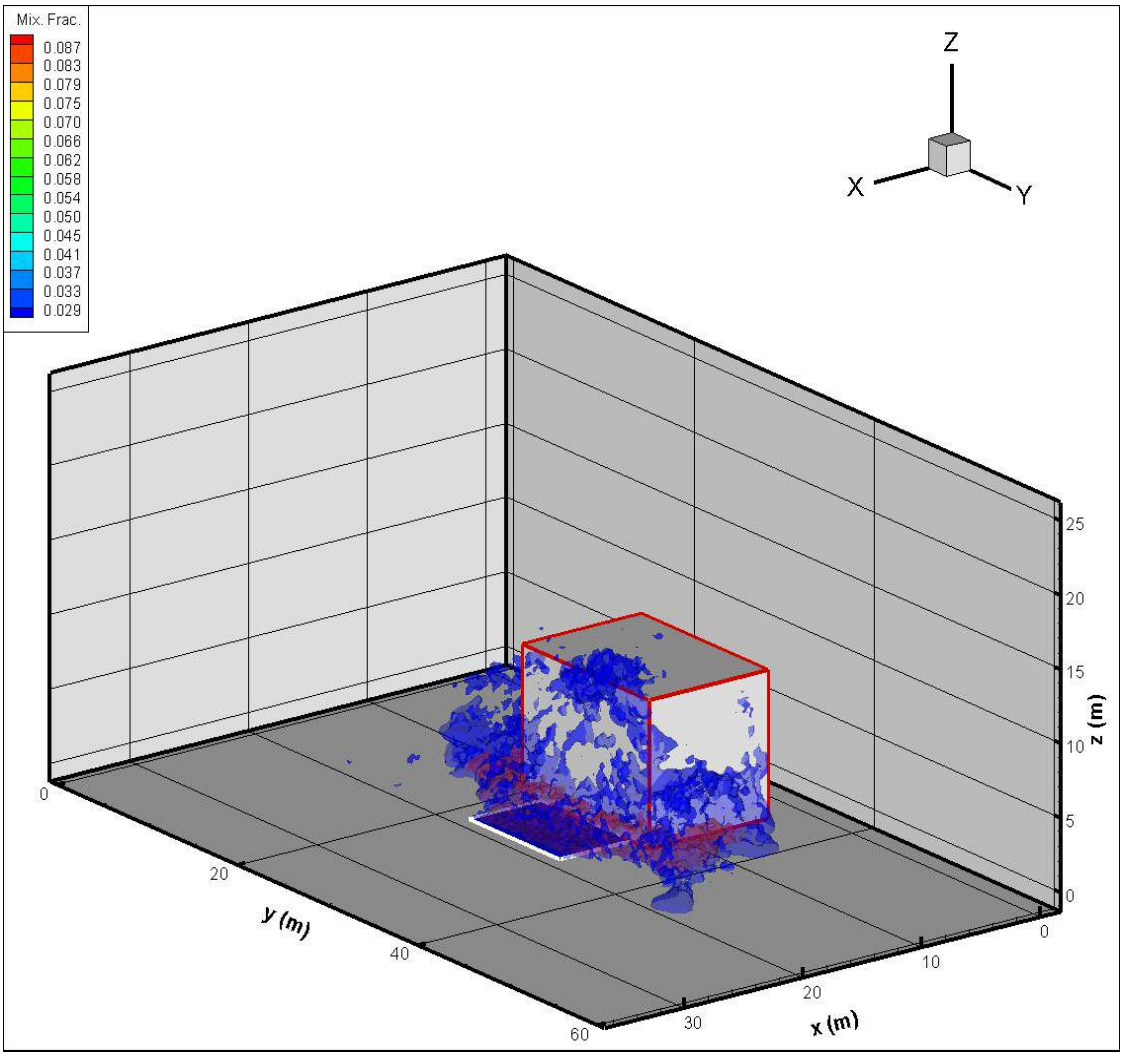

Figure 10: Mixture Fraction Cloud with Lower Flammability Limit Iso-Surface for 2.0 m/s wind velocity

In Dispersion Cases 1 and 2, the mass of flammable material encompasses much of the lower center mesh and exists on the leeward side of the low-aspect ratio obstruction. Case 1 can be seen to have the largest mass of flammable methane gas sitting directly above the pool relative to the other dispersion tests. Case 1's mixture fraction iso-contours show large stratified methane dispersions, where flammable portions of the cloud sit directly atop fuel rich methane gas. The methane buildup sits atop the injection of methane fuel emanating from the pool. Fuel rich mixture (with mixture fraction greater than .087 kg/kg) has spread out from the boundaries of the methane pool in the stream-wise and cross-stream directions on the simulation floor.

The effects of the higher average wind speed in Case 2 are noticeable in the tapering methane cloud on either side of the leeward face of the ship, as well as in the decreased flammable mass sitting directly atop the pool. The 1.0 m/s wind velocity dispersion also exhibits x and y-direction spread of methane rich gas across the floor of the test domain. As discussed in section 3.2.1, the mass of the Case 1 and Case 2 clouds are nearly identical; the shape of the clouds has changed due to the difference in flow speed.

There is a radical change in the shape and size of the Case 3 dispersion cloud compared to those of Cases 1 and 2. The 2.0 m/s wind dispersion illustrates sparse flammable material spread along the side and leeward face of the obstacle, consistent with the comparatively small flammable mass of Case 3 discussed in section 3.2.1. It is observed from figure 10 that much of the fuel-rich cloud that had covered the floor in Cases 1 and 2 is largely absent in Case 3, with the existing fuel-rich mass pushed against the sides and

leeward face of the obstruction. There is no stream-wise or cross-stream spread of methane gas from the pool. Further flow visualization variables such as the u-velocity magnitude give insight into the behavior of the methane cloud for the three dispersions.

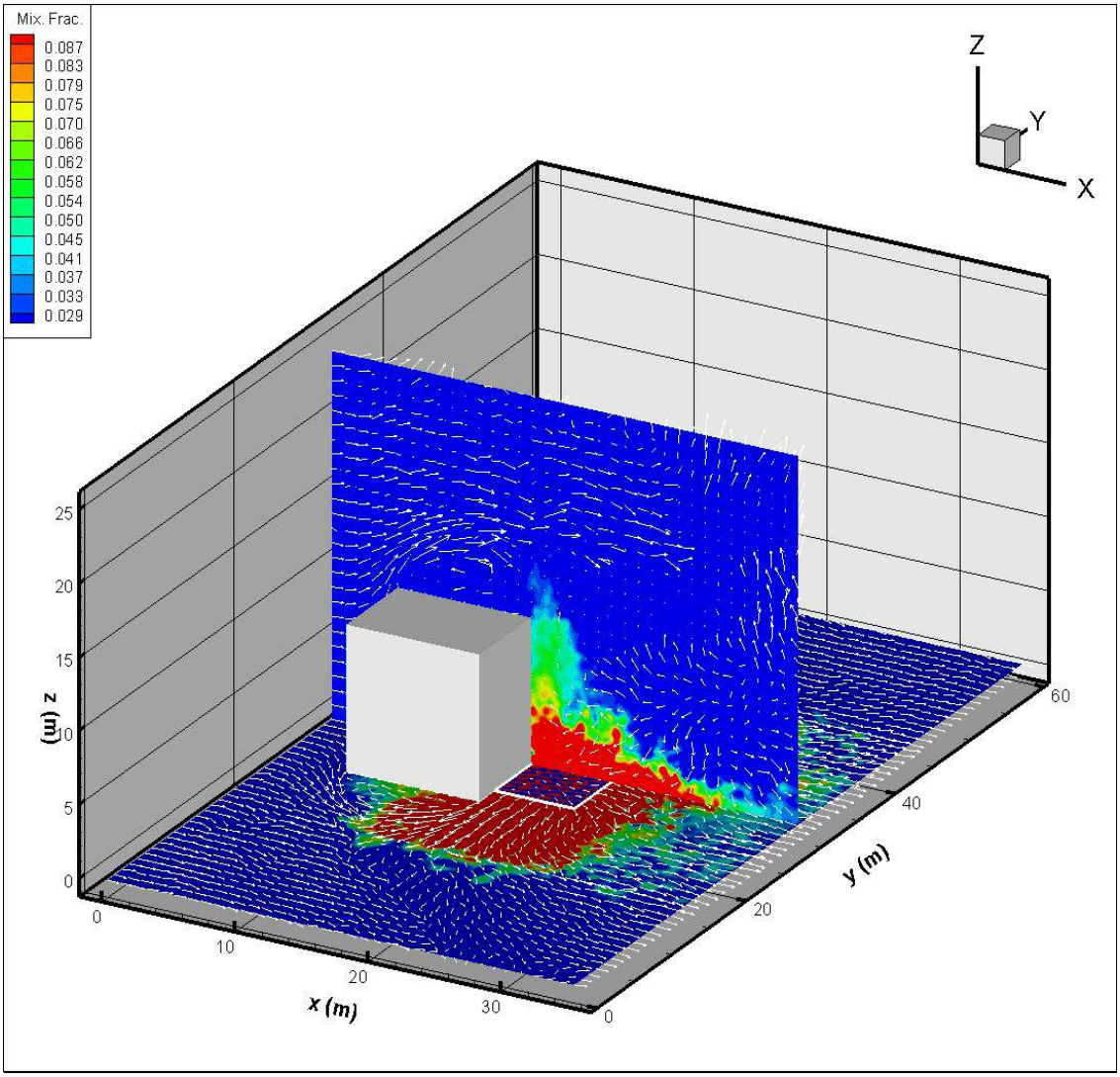

Figure 11: Mixture Fraction Mid-Plane and Floor Iso-Contours for 0.5 m/s wind

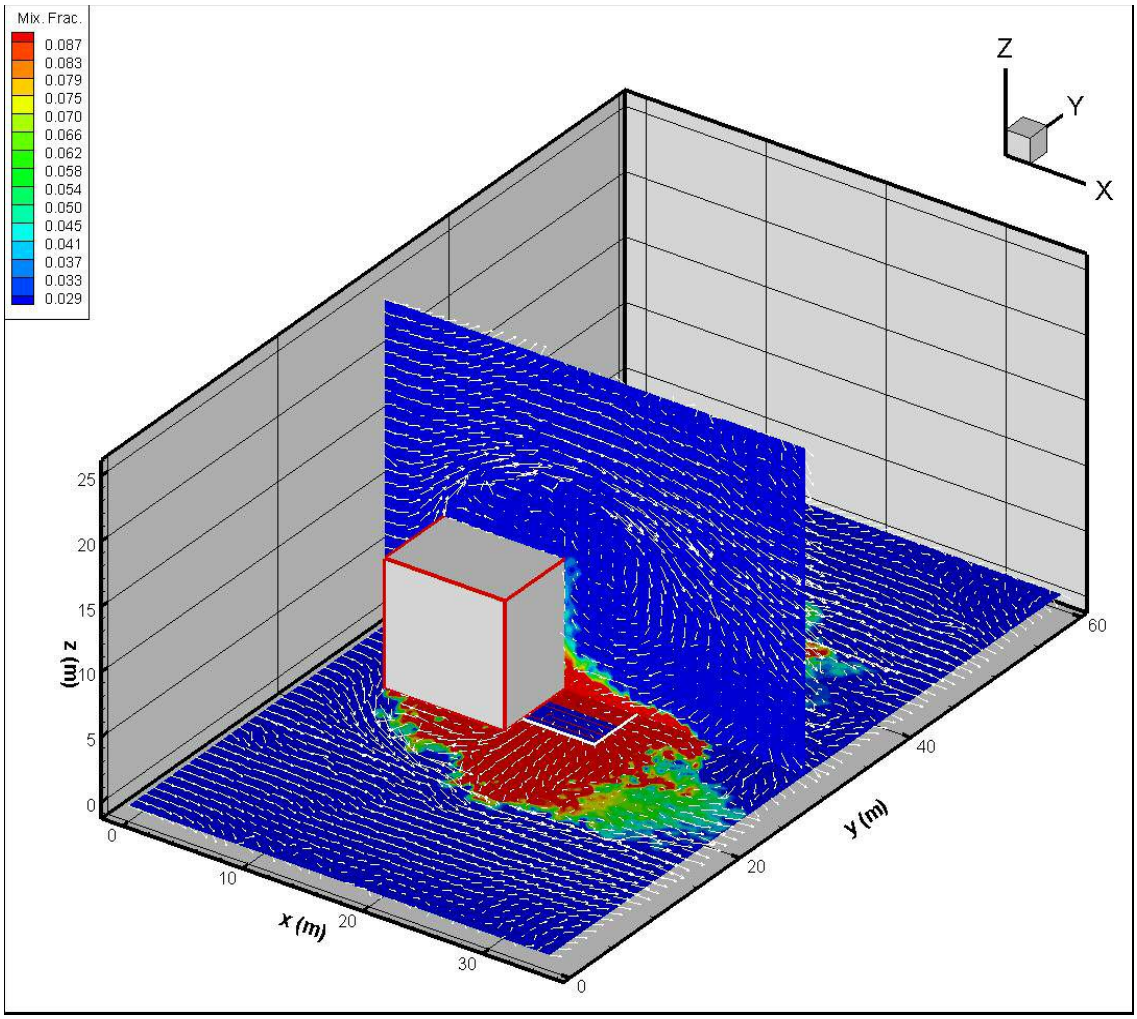

Figure 12: Mixture Fraction Mid-Plane and Floor Iso-Contours for 1.0 m/s wind

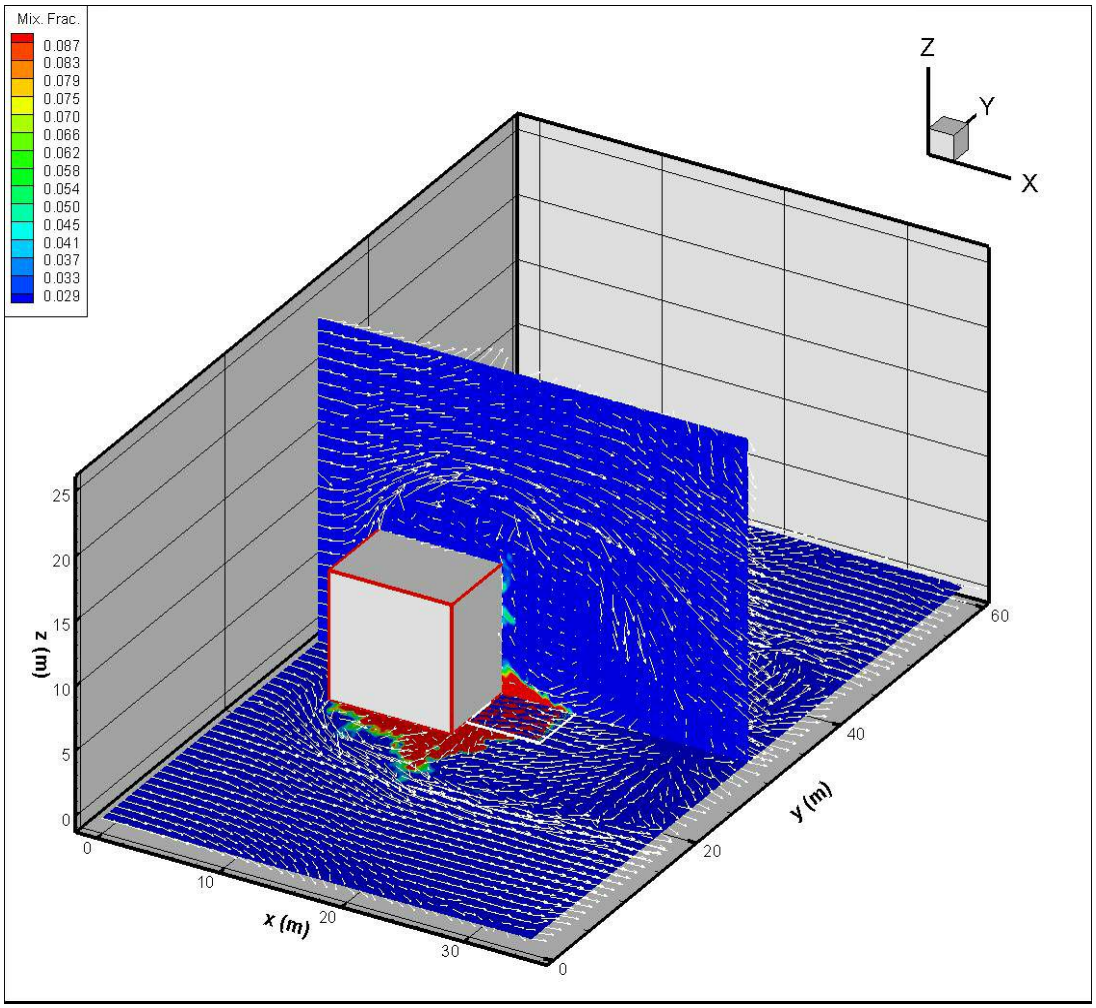

Figure 13: Mixture Fraction Mid-Plane and Floor Iso-Contours for 2.0 m/s wind

3.2.3 U-Velocity Iso-Contours and Velocity Vectors

Constant-value contours of the x-velocity component are illustrated in figures 14 through 25 along with a velocity vector overlay, and provide explanation for the behavior of the methane cloud dispersion in Cases 1-3.

Recall from figures 8 and 11 the large flammable mass sitting directly over the methane pool for the 0.5 m/s wind velocity dispersion. Figure 14 demonstrates lower velocity magnitude immediately downstream of the leeward face of the obstruction; there is no strong recirculation downstream of the obstacle, and the mass of injected methane gas sits directly over the pool.

Figure 14 also demonstrates the spreading of the cool methane mass close to the floor of the domain, out and away from the fuel source. The velocity vectors at the leeward corners of the obstruction curl back towards the sides of the obstacles; this is consistent with the behavior of the low-lying methane-rich cloud in figures 8 and 11.

Relationships can be similarly made clear between the velocity data and methane cloud behavior for Cases 2 and 3. It can be gleaned from figure 15 that flow structures illustrated in figure 3 are more prominent in the 1.0 m/s than in the 0.5 m/s wind dispersion. There is noticeable downstream recirculation pushing the methane cloud out and away from the center of the obstruction. Weak recirculation regions that existed on the side and top of the obstacle in Case 1 are stronger in Case 2. The horseshoe vortices illustrated in figure 3 also appear in figures 15 and 20 through 22. The structure of the velocity flow in figure 15 matches the features in figures 9 and 12.

Case 3 demonstrates the largest recirculation zones among the three dispersion tests. Recirculation zones on the side, top, and downstream of the obstruction are clearly defined, as are the horseshoe vortices propagating in the x-direction. The methane cloud for Case 3 is the most dilute of the dispersion cases (see figures 10, 13 and 16), as strong negative u-velocity components push the flammable mass towards either horseshoe vortex, where it is further mixed to fuel-lean portions.

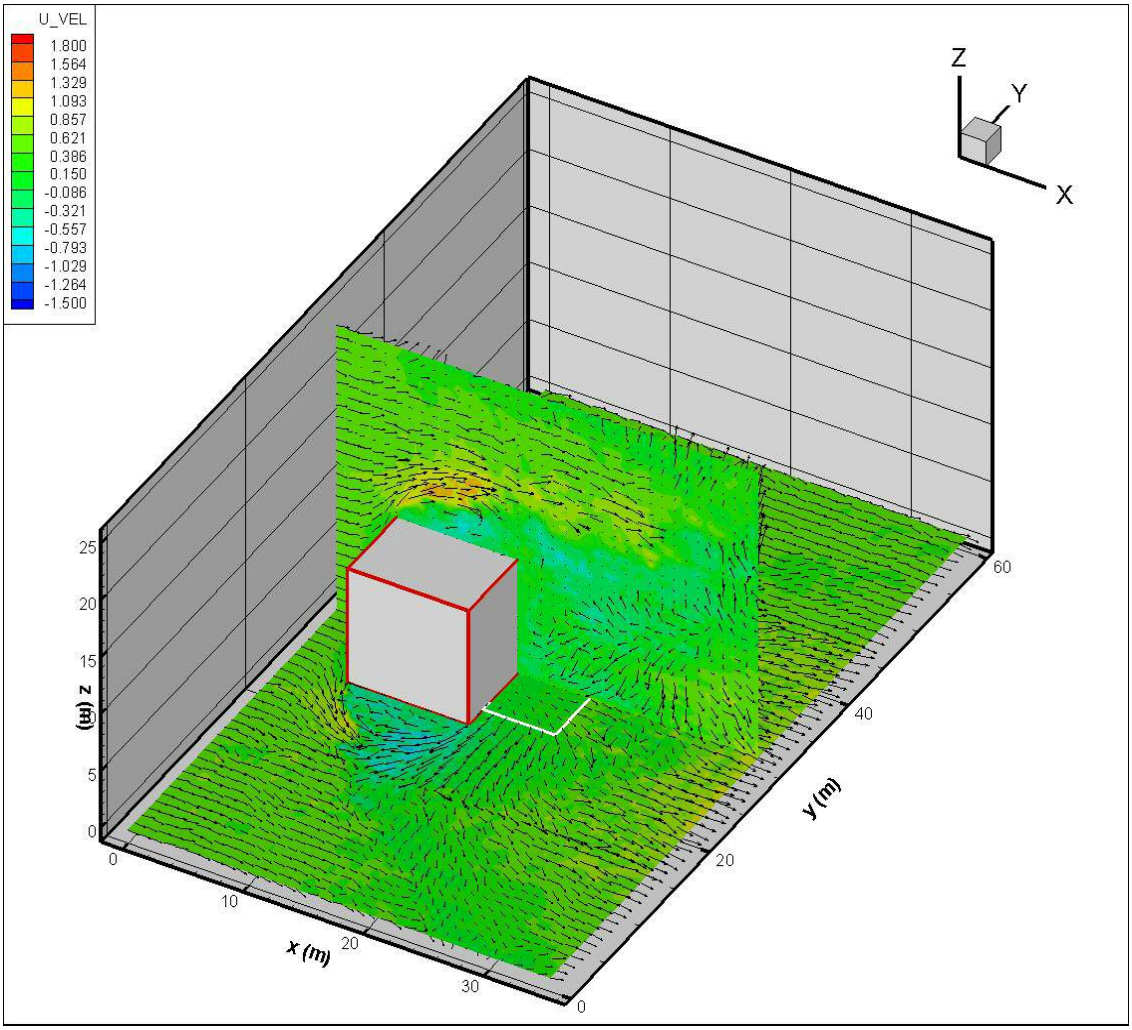

Figure 14: U-Velocity Iso-Contours with Velocity Vector Overlay for 0.5 m/s wind

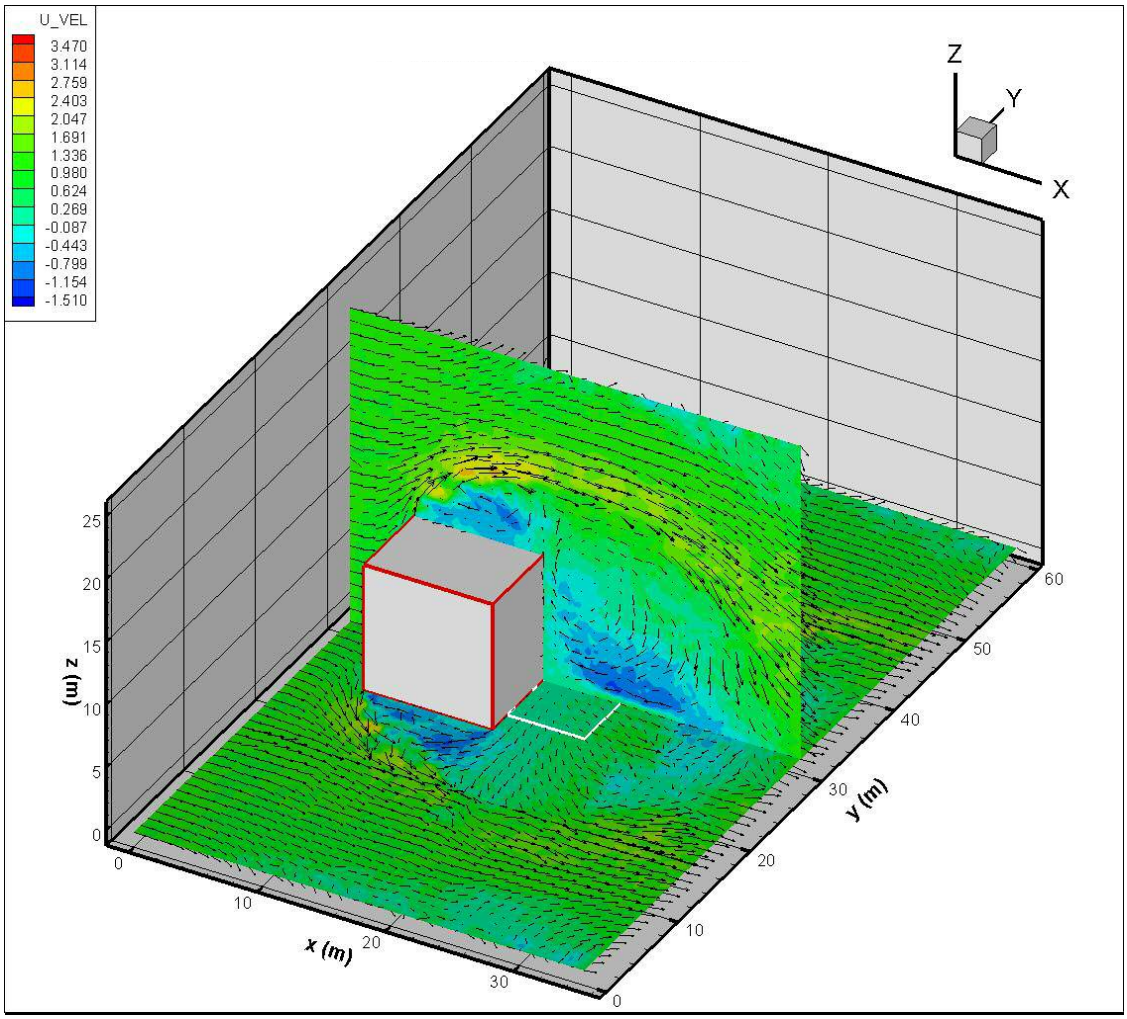

Figure 15: U-Velocity Iso-Contours with Velocity Vector Overlay for 1.0 m/s wind

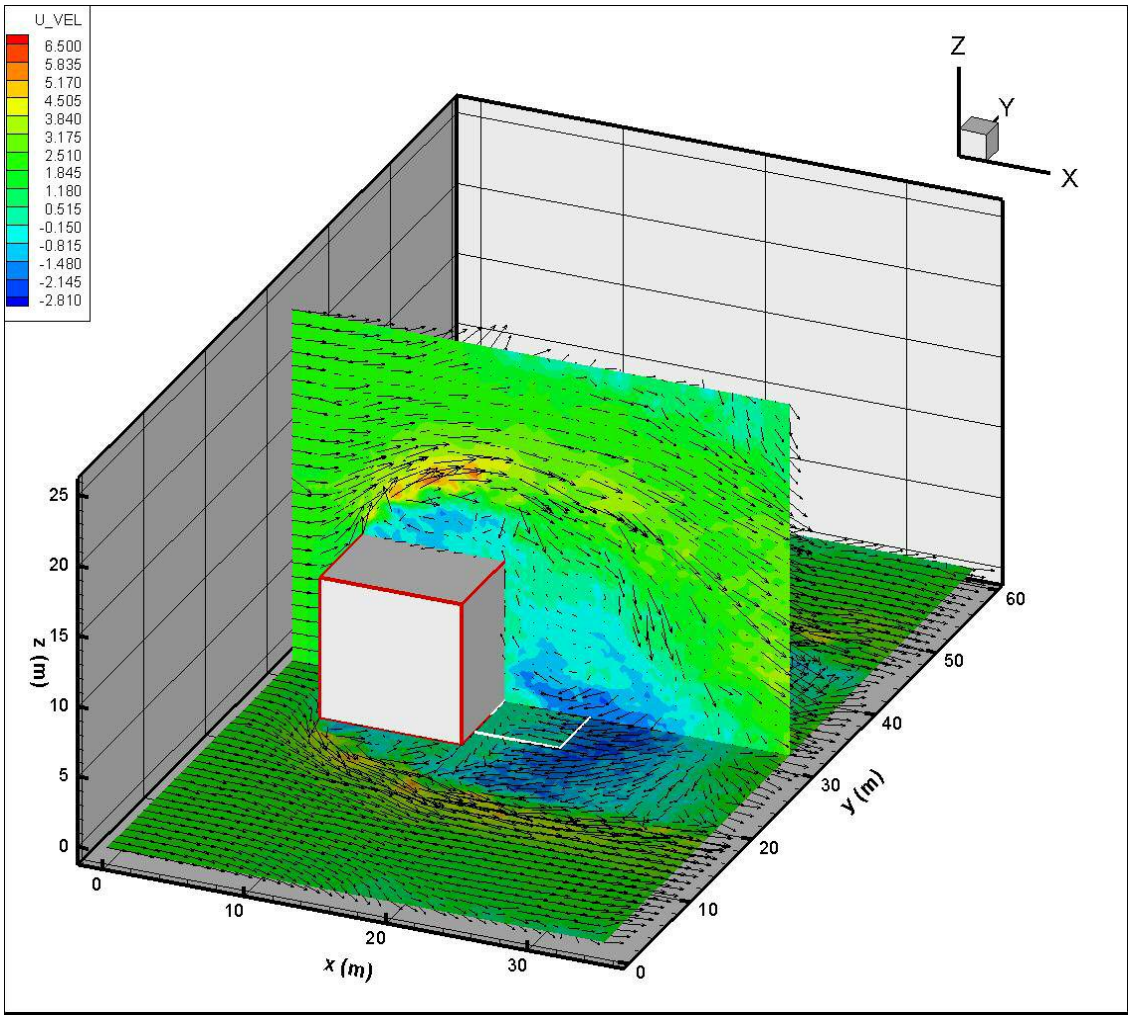

Figure 16: U-Velocity Iso-Contours with Velocity Vector Overlay for 2.0 m/s wind

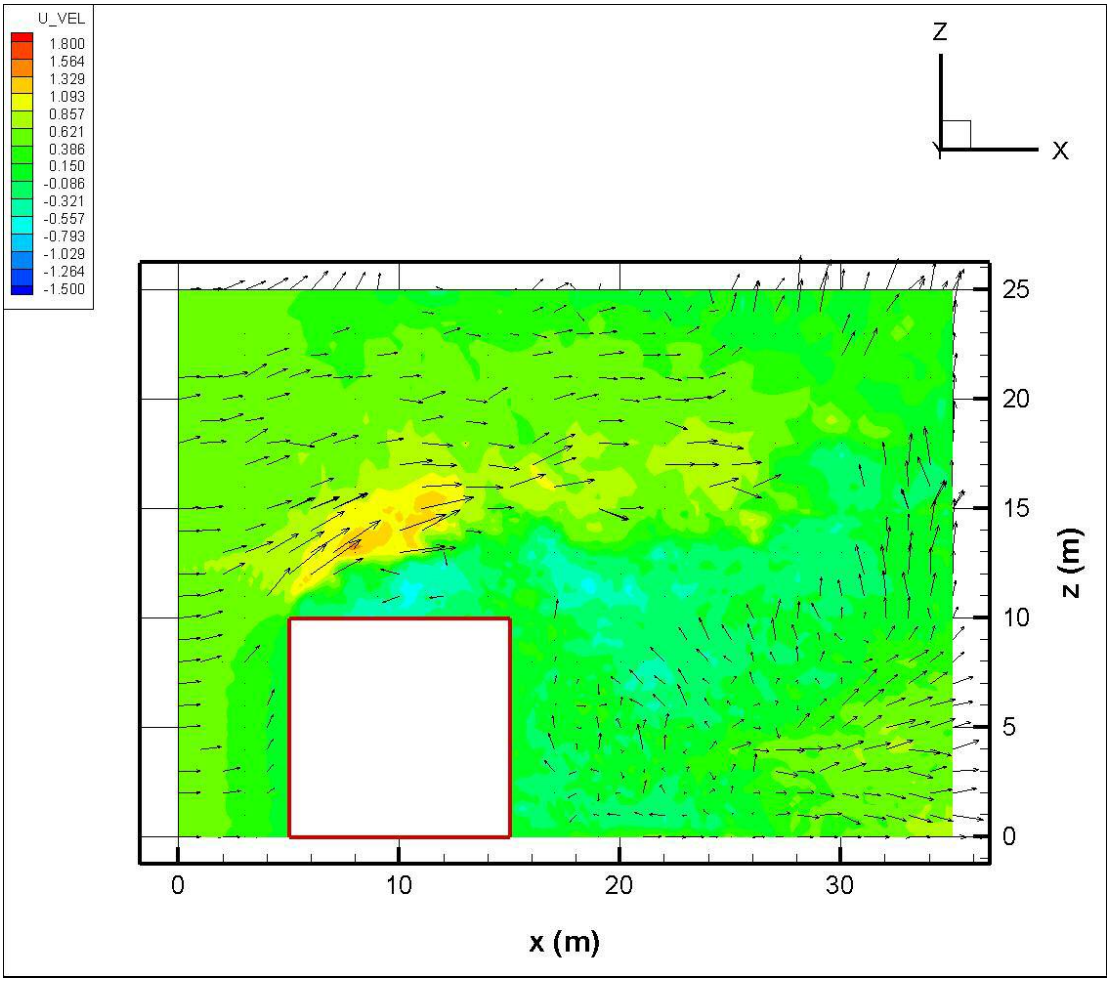

Figure 17: Side Profile (y = 30.0 m Plane) for 0.5 m/s Wind Dispersion

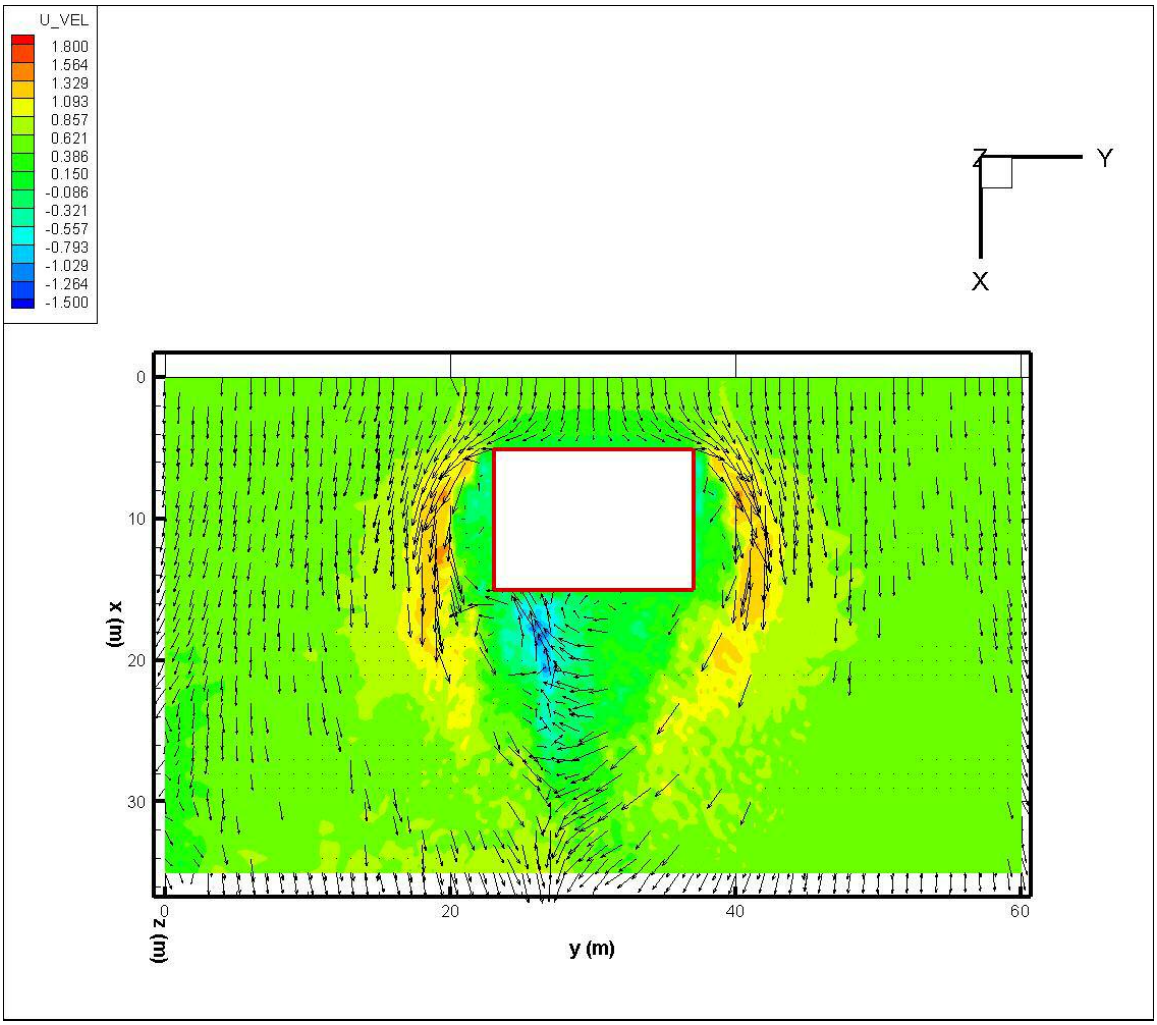

Figure 18: Top Profile (z = 5.0 m Plane) for 0.5 m/s Wind Dispersion

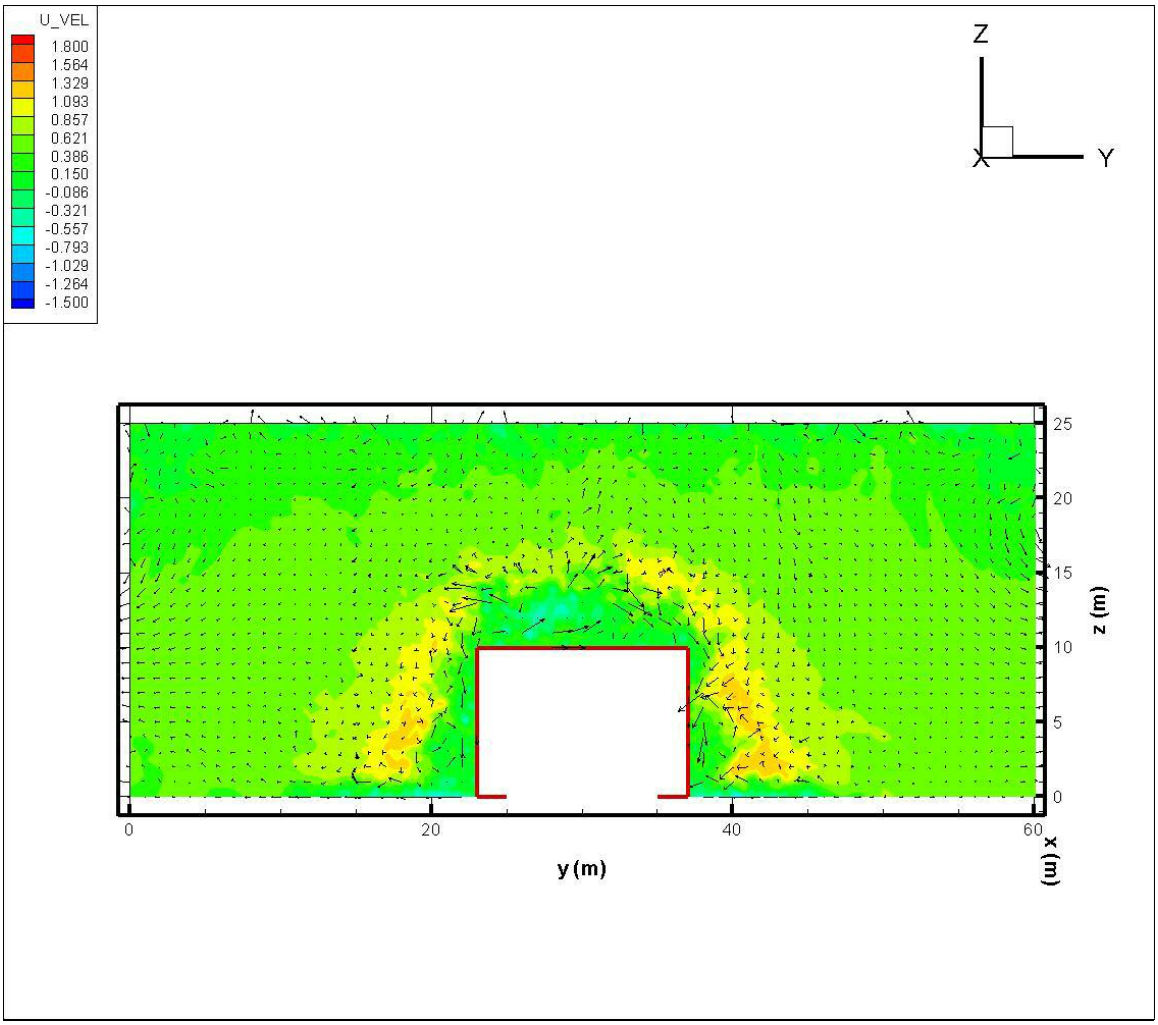

Figure 19: Front Profile (x = 15.0 m Plane) for 0.5 m/s Wind Dispersion

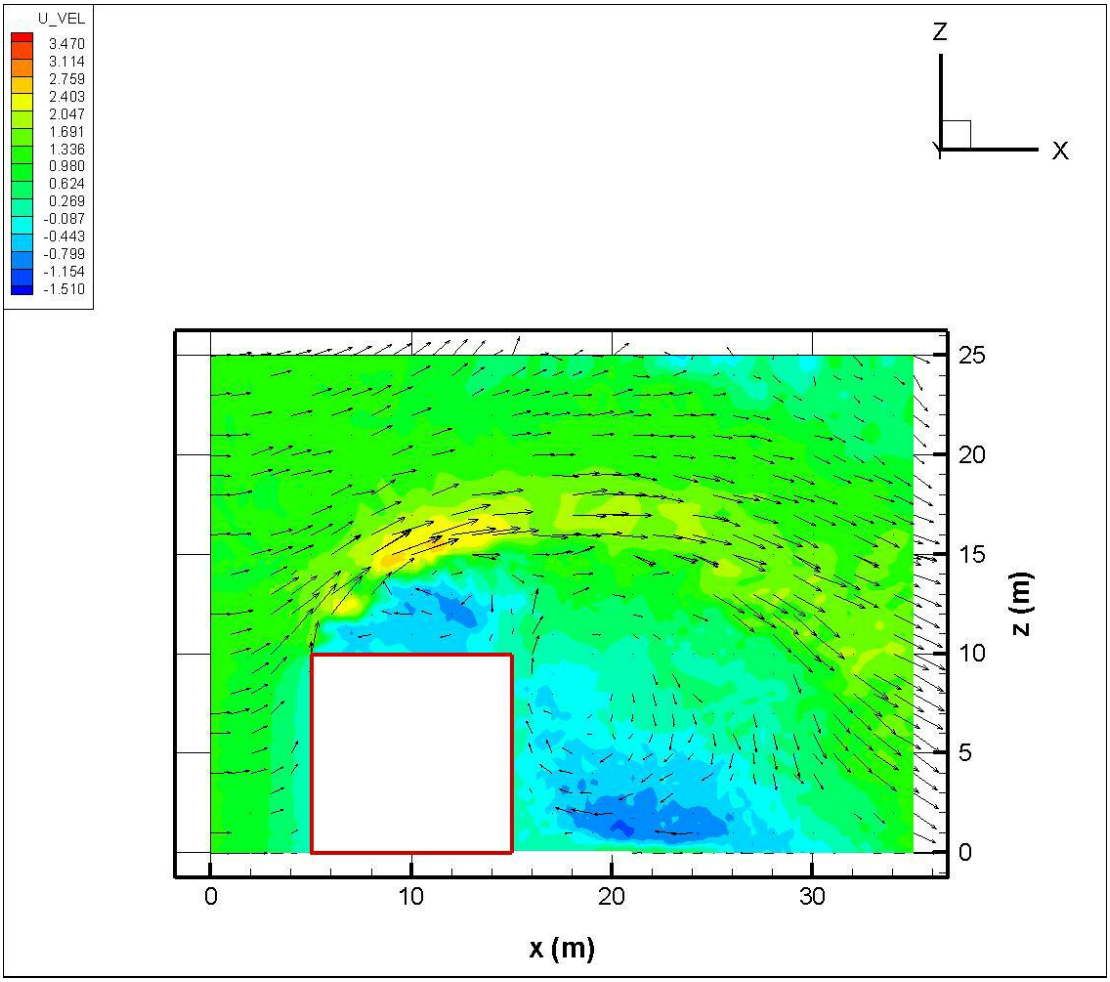

Figure 20: Side Profile (y = 30.0 m Plane) for 1.0 m/s Wind Dispersion

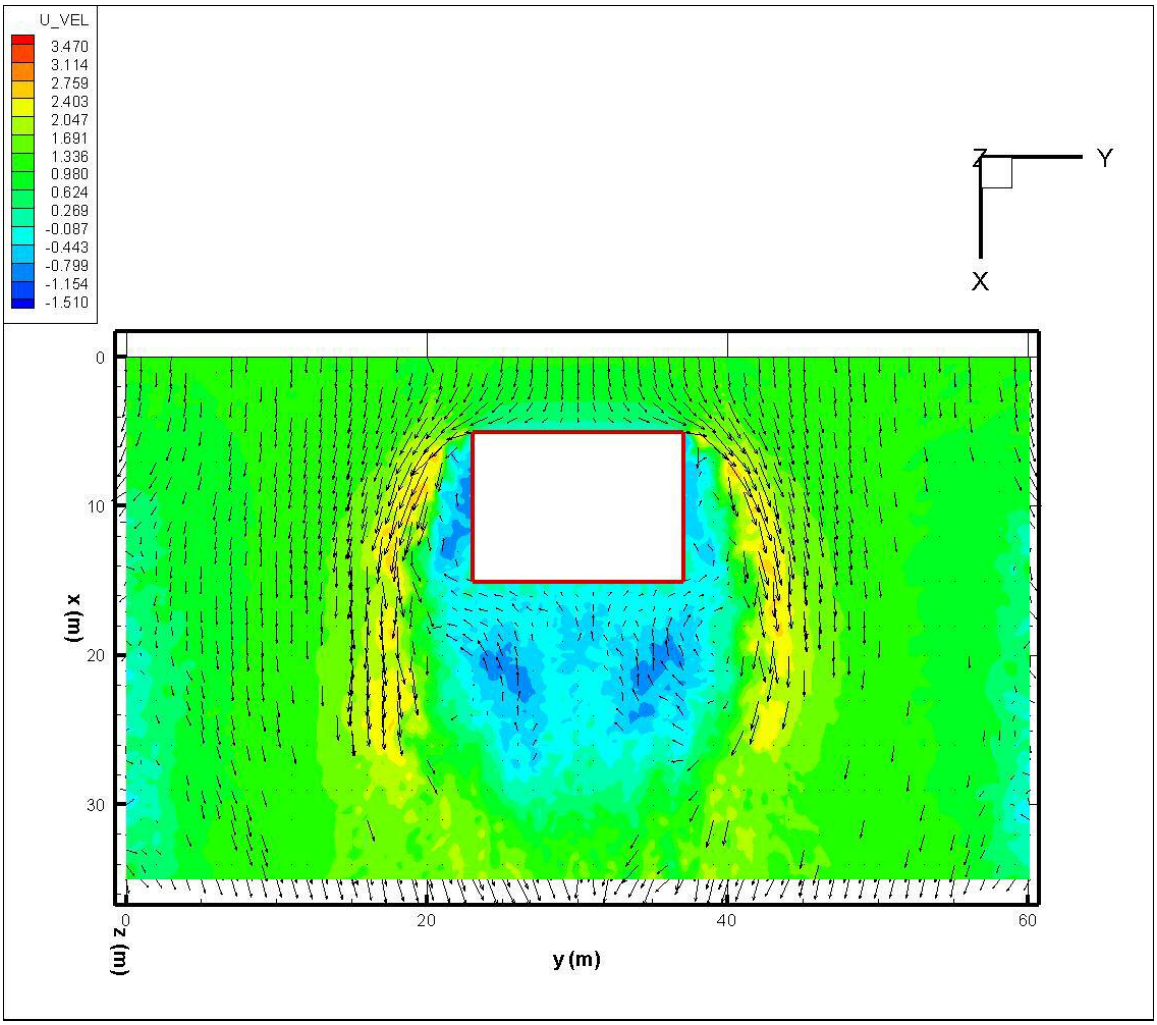

Figure 21: Top Profile (z = 5.0 m Plane) for 1.0 m/s Wind Dispersion

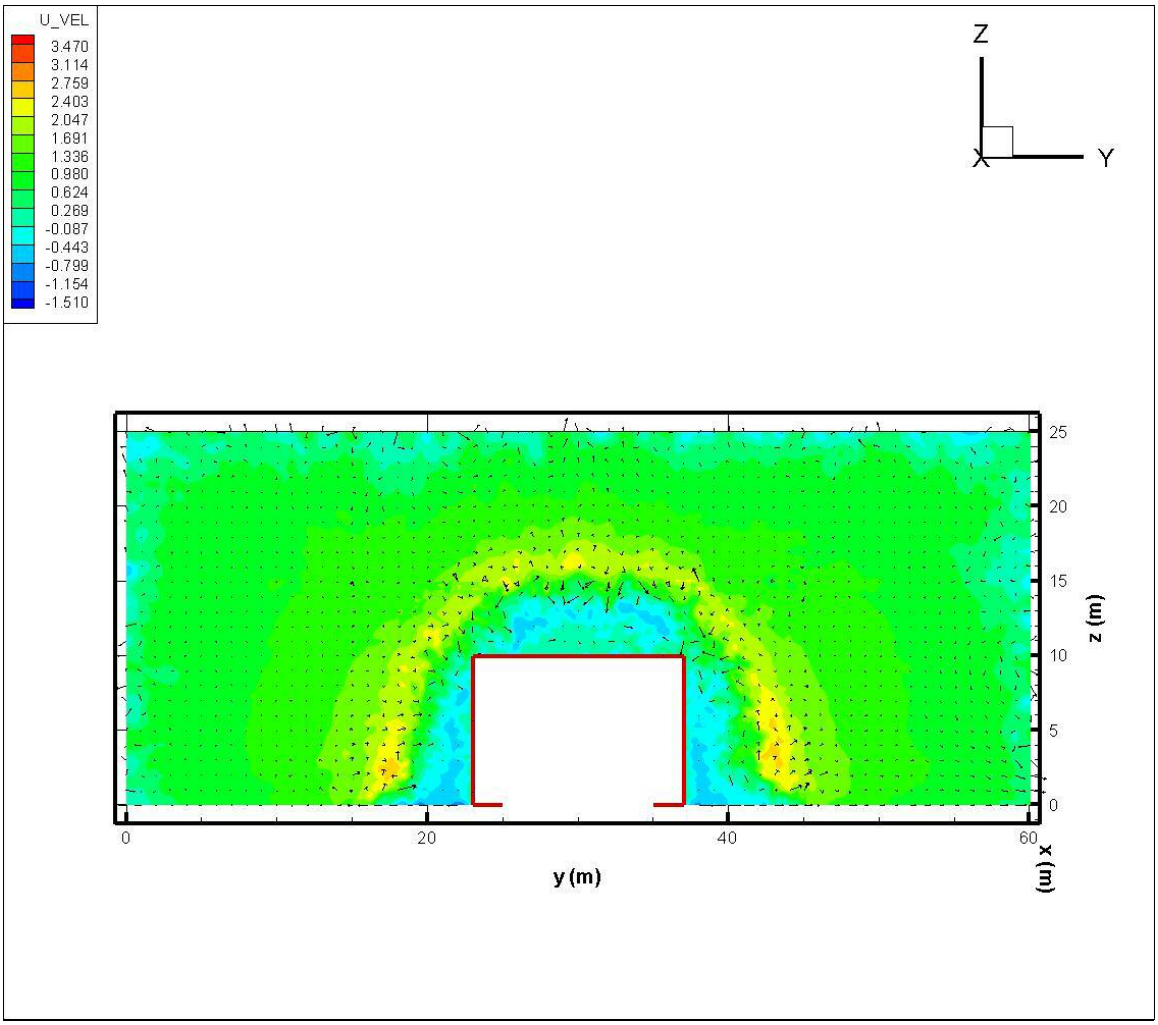

Figure 22: Front Profile (x = 15.0 m Plane) for 1.0 m/s Wind Dispersion

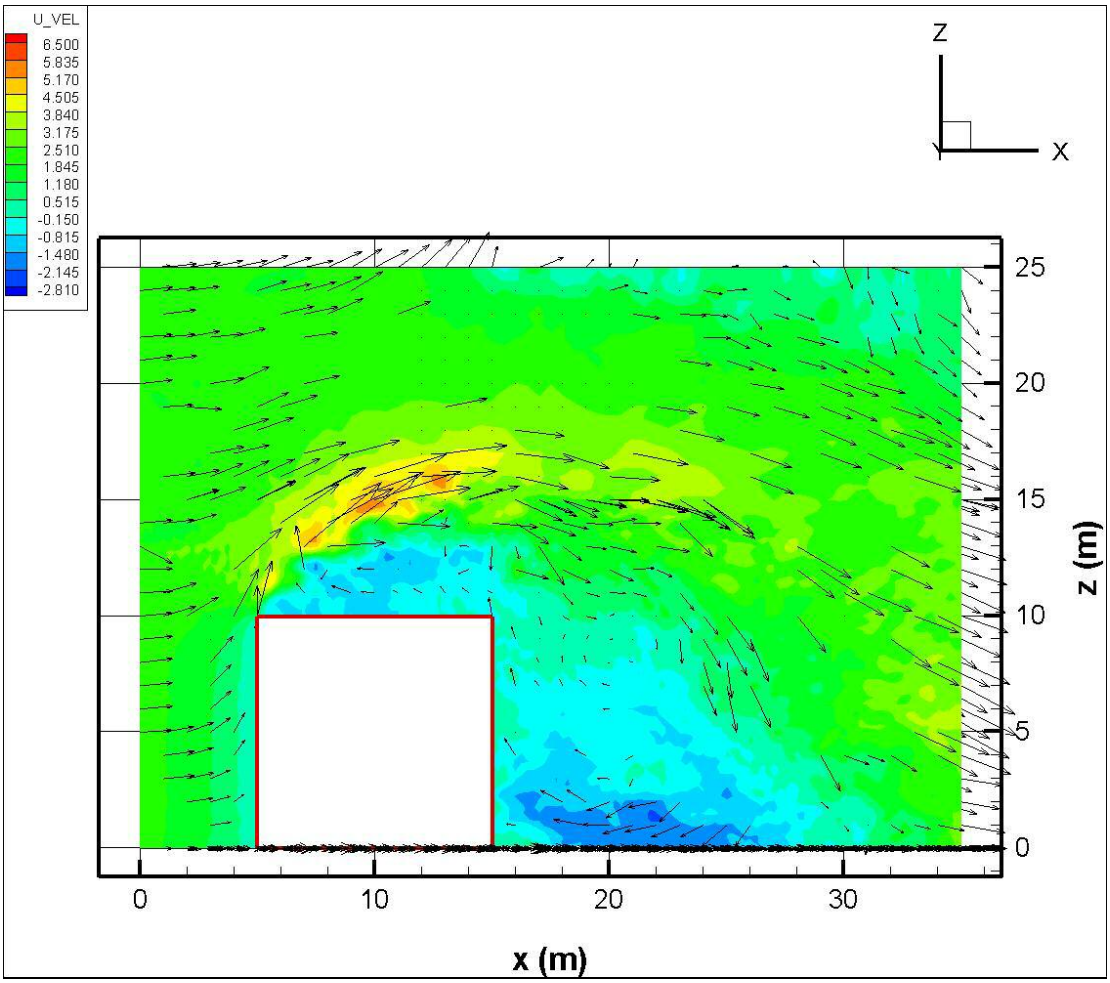

Figure 23: Side Profile (y = 30.0 m Plane) for 2.0 m/s Wind Dispersion

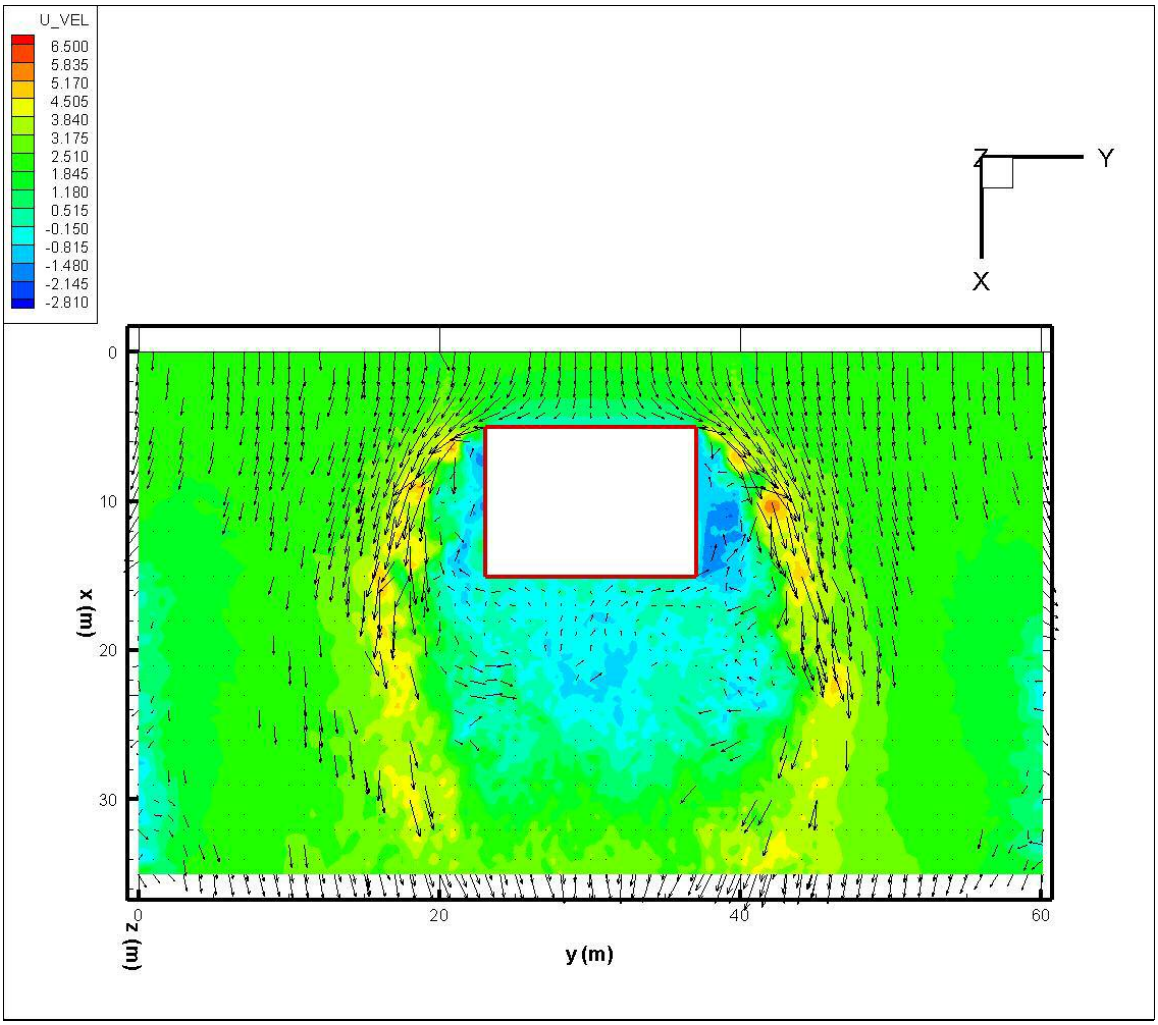

Figure 24: Top Profile (z = 5.0 m Plane) for 2.0 m/s Wind Dispersion

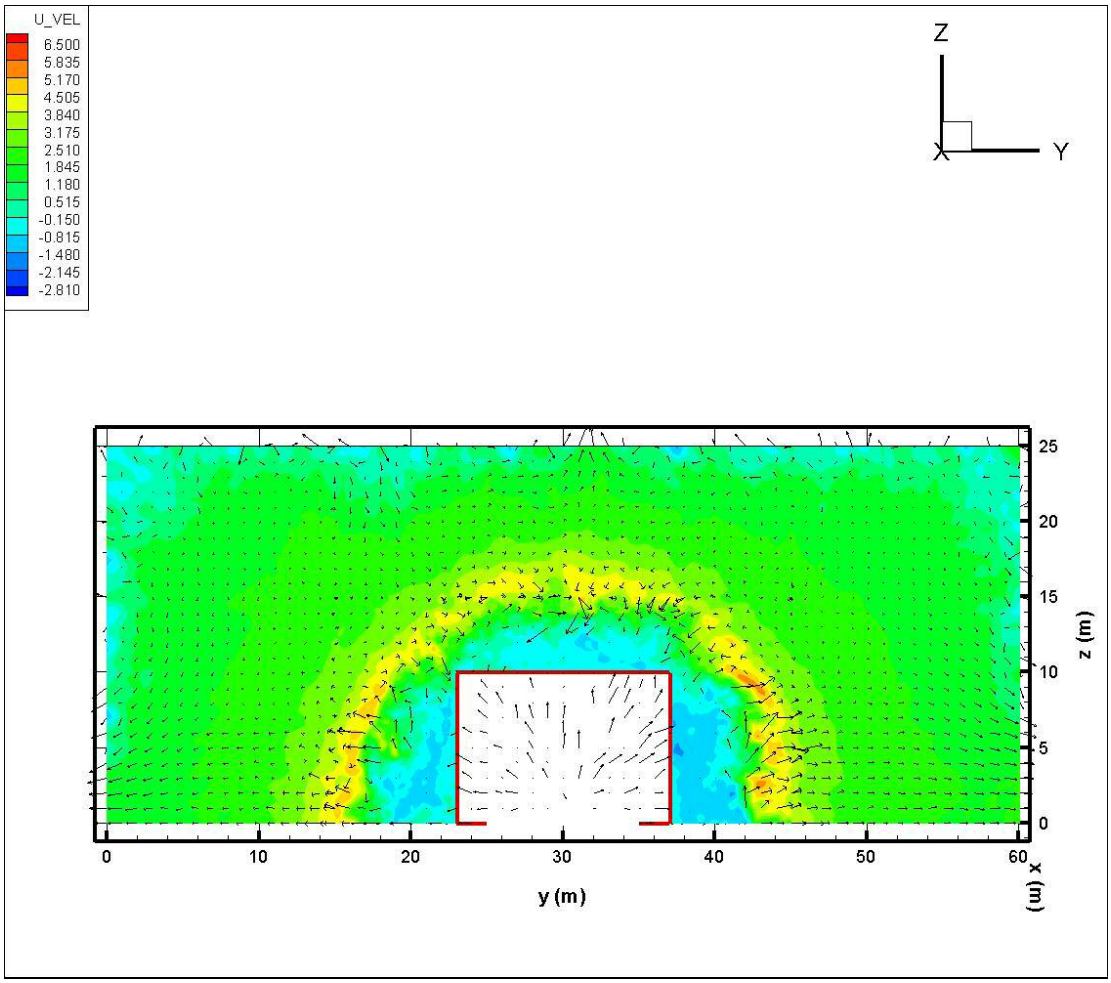

Figure 25: Front Profile (x = 15.0 m Plane) for 2.0 m/s Wind Dispersion

3.2.4 Mixture Fraction-Temperature Relationship

Mixture fraction-temperature scatter plots serve to verify that the appropriate fuel mixture density is calculated by FDS. Figure 26 is the scatter plot for the 0.5 m/s wind dispersion. Point values at high temperatures and low mixture fractions are associated with fuel-lean regions away from the pool, while low-temperature/high mixture fractions are attributed to fuel-rich regions very close to the pool. Figure 26 shows that at a mixture fraction of 0.8 kg/kg, the temperature is approximately -140 C. This data point is likely near or directly above the super-cooled fuel source.

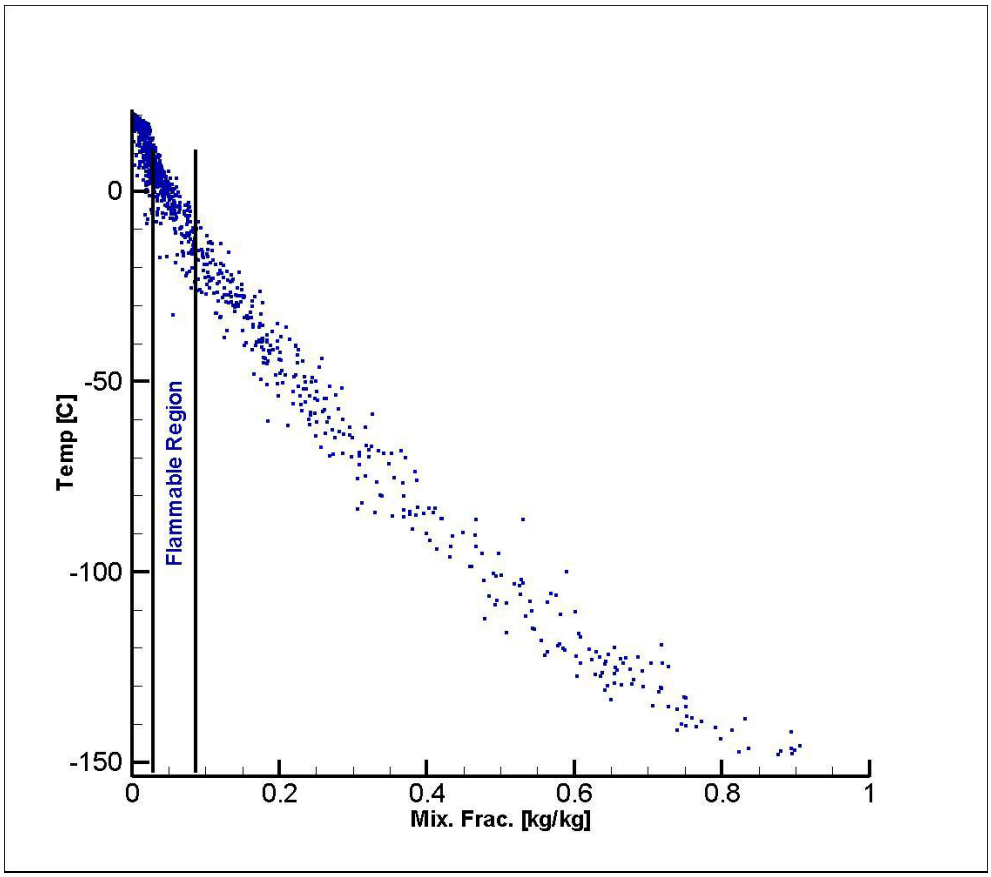

Figure 26: Mixture Fraction-Temperature Scatter for Case 1 (0.5 m/s Wind) Dispersion

The scatter plot for Case 2 demonstrates nearly identical correlation between the temperature and mixture fraction. The 2.0 m/s wind velocity scenario results in lower maximum mixture fractions and a higher minimum temperature. This is attributable to the stronger recirculation observed in the mixture fraction and u-velocity iso-contours for Case 3, in addition to the flammable mass illustrations in figures 6 and 7.

Temperature iso-contours compliment the scatter plot and mixture fraction iso-contour data. Figure 27 demonstrates that temperatures approaching -150 C occur at the floor of the domain and within the methane pool boundaries. It is seen clearly from figure 26 that these temperatures are associated with mixture fractions approaching 0.9 kg/kg. Similar scatter plot/temperature relationships are observed in corresponding Case 2 and 3.

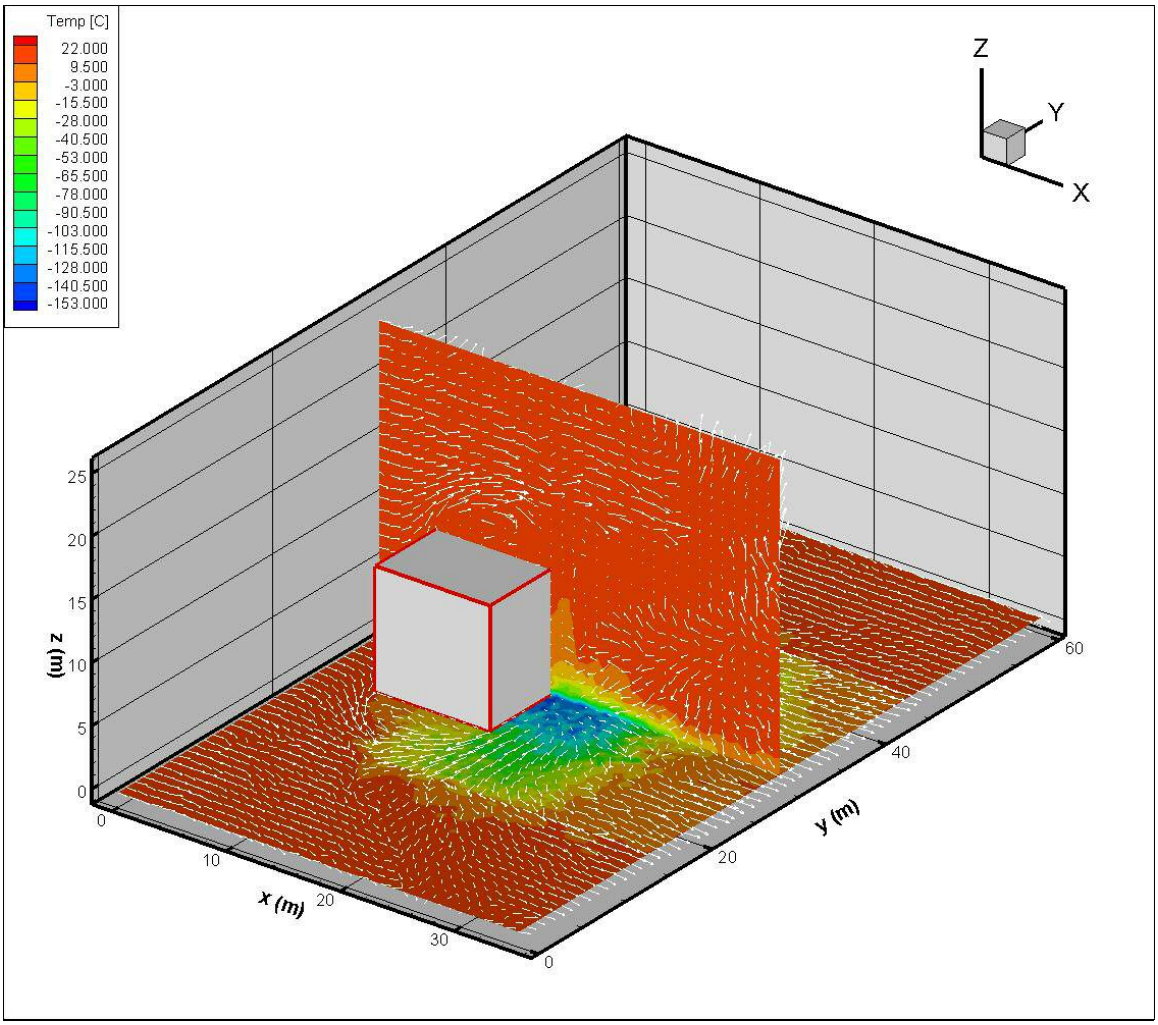

Figure 27: Temperature Mid-Plane and Floor Iso-Contours for 0.5 m/s wind

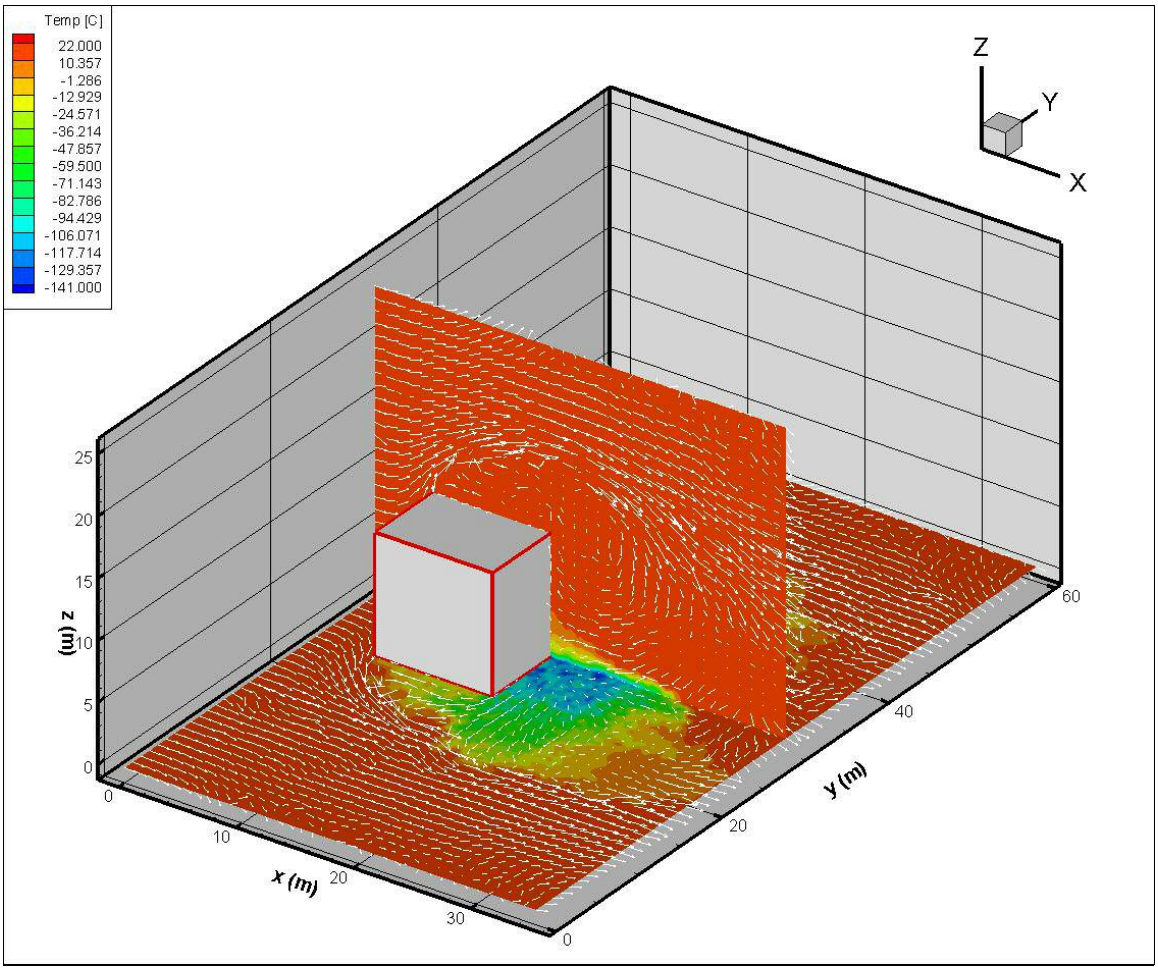

Figure 28: Temperature Mid-Plane and Floor Iso-Contours for 1.0 m/s wind

CHAPTER 4 COMBUSTION MODEL

4.1 Combustion Modeling Results

Dispersion modeling results provided initial conditions for simulating ignition and subsequent flame development of the fuel vapor cloud. Several diagnostics were assembled to evaluate the combustion simulation results. For example, heat release rate is tracked and compared to the predicted value based on the prescribed burn rate and heat of combustion for the cryogenic fuel. Similarly, the flame height predicted from empirical relationships is compared to the FDS-calculated height, which is visualized as an iso-surface of the stoichiometric mixture fraction. Flame height is also validated by mixture fraction iso-contours generated after a successful transition to a diffusion flame. The relative position of burnt and unburnt reactants is illustrated by iso-contours of the reaction progress variable.

New analysis of the flame and heat transfer assesses the danger to human beings within the vicinity of the fire. The National Fire Protection Association has set forth guidelines for acceptable exposure to incident heat flux. Temperature measurement devices have been added to the floor of the domain during the combustion event. In order to evaluate this heat transfer, each thermocouple is located downstream of the pool, to record the incident heat flux in 1-meter increments.

The Case 1 (0.5 m/s wind) dispersion warranted an ignition trial of its large flammable mass. Although Case 2 has similar flammable mass, Case 1 was chosen due to its lower wind speed, and the favorable location of its flammable mass, which can be seen from

figure 8 to be directly over the vaporizing pool. The FDS ignition model (the $\overline{\dot{\omega}_{ign}'''}$ source term in equation 2.24) initiates a premixed combustion event with a spherical kernel defined by its radius, position in the test domain, and activation and deactivation times (see Appendix A.3).

A successful ignition of the flammable cloud generates a premixed combustion event, which would transition to a diffusion flame event once the premixed reactants have been consumed. Subsequently, the energy balance at the pool surface includes the diffusion flame heat feedback to the cryogenic pool in addition to the water-to-spill temperature-driven convection as in equation 2.6. Babrauskas lists an empirically-determined mass flux for an LNG pool fire, given as .078 kg/m^2/s [31]. The total heat flux from the flame, $\dot{q}''_{fire}$ [kW/m^2], is then the summation of heat flux due to mass flux from the convection at the LNG/water interface, and the heat flux due to the mass flux caused by the flame heat feedback. The calculated total fire heat flux is approximately 4.06 MW, and from equation 2.7, this sets the heat feedback at .02258 kg/m^2/s. The expected maximum heat release rate for the non-premixed methane flame is 172.64 MW. In FDS, the steady state diffusion flame model predicts 100% combustion efficiency; the rate of fuel mass ejection is equal to the volume integral of the rate of fuel consumption at the flame sheet [36]. The feedback mass flux is ignored in the present study as a manner of simplification, and can be implemented in future work involving LNG spill models.

4.1.1 Methane Cloud Ignition

The flammable fuel cloud from Case 1 ignited and transitioned from a premixed combustion phase to a diffusion flame, but the average non-premixed heat release rate calculated by FDS was .349 MW; this is one order magnitude smaller than that predicted by the product of the burn rate and the by-mass heat of combustion for methane (a heat release rate of 172 MW).

It can be seen from figures 8 and 11 that although a large flammable mass sits above the pool, stratification near the pool leads to a large intermediary of fuel-rich methane. This fuel-rich region extends nearly to the floor of the domain, and insulates the fuel source (the methane pool) from the ignited premixed combustion event above it. Thus, the premixed flame cannot propagate downward to the pool and transition into a diffusion flame event; the burn rate of the methane fuel does not equal the rate of vaporization and the heat release rate is incorrectly predicted.

This result demonstrates that igniting the largest flammable mass of the three dispersions is still limited by insufficient mixing. Case 2 has comparable flammable mass, and a similarly stratified cloud, in which fuel-rich methane separates flammable cloud portions from the pool needed for diffusion flame transition. The 2.0 m/s wind dispersion mixes too fast, and its flammable mass is half that of Cases 1 and 2.The flammable mass in the vicinity of the vaporizing pool is not only significantly smaller than the two earlier cases, but also broken into smaller segregated domains.

For the purpose of studying the resulting diffusion flame, the upper flammability limit of methane was set to 0.7 (up from its actual value of 0.087) in the FDS database so as to facilitate a premixed combustion event. Prediction of the premixed heat release rate (equation 2.26) would be altered, as the FDS approximation for the laminar flame speed relies on the flammability limits. Non-premixed combustion, however, depends only on the stoichiometric mixture fraction (Z_f), the fuel-mass ratio found at the diffusion flame sheet. Z_f is not affected by any alteration to the flammability limits, which are scalar multiples of the calculated stoichiometric mixture fraction. This can be seen from the relationship for Z_f - equation 2.10. From equation 2.17 it is shown that the heat release rate calculated by FDS for non-premixed combustion is dependant on the stoichiometric mixture fraction, but neither of the flammability limits. Thus, diffusion flame heat release rates are unaffected by any arbitrary changes to the flammability limits.

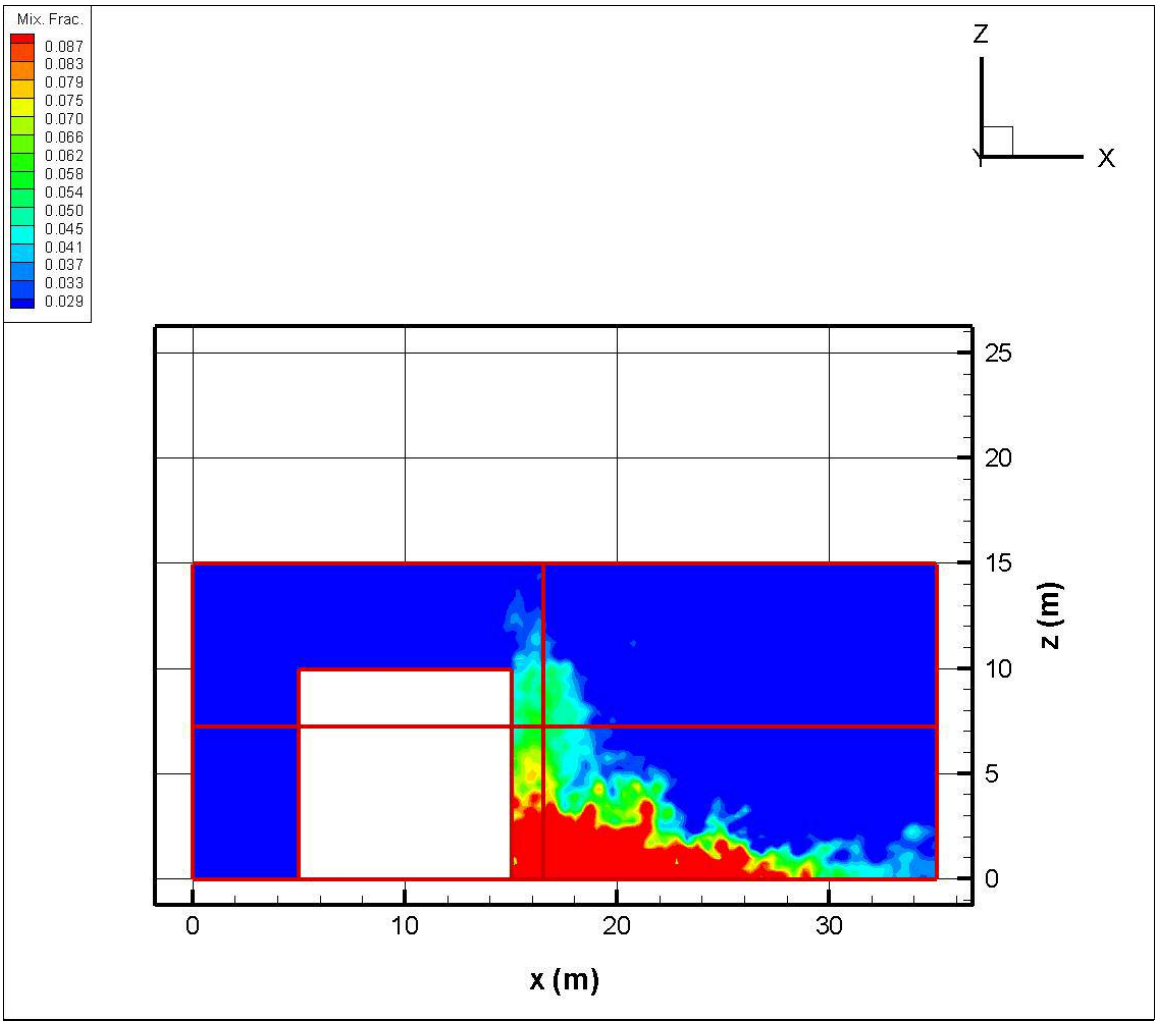

Figure 29: Crosshair Intersection of the Ignition Point Candidate for Case 1, Side View

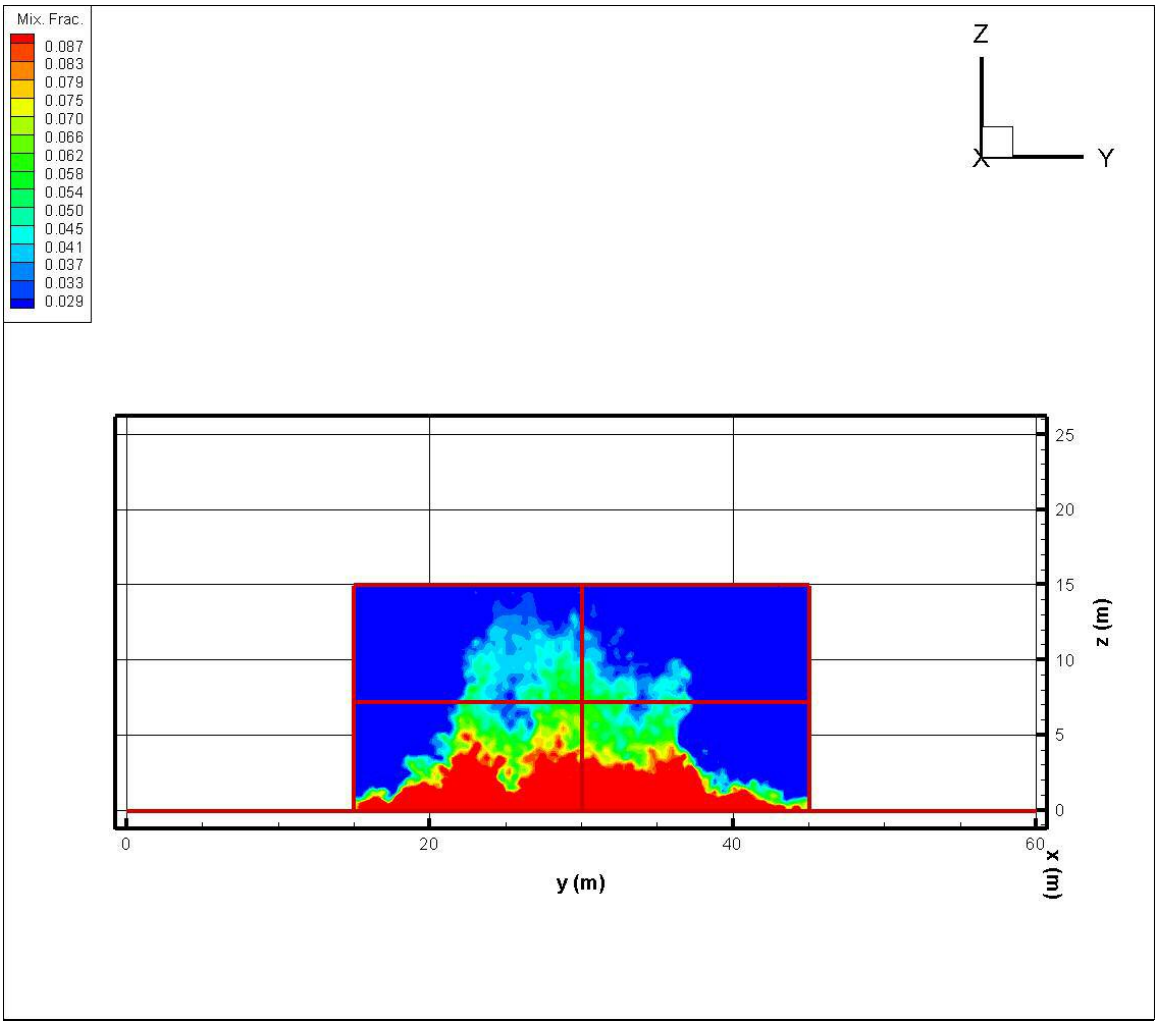

Figure 30: Crosshair Intersection of the Ignition Point Candidate for Case 1, Front View

4.1.2 Heat Release Rate

Diffusion flame heat release rates were attained by expanding the upper flammability limit for methane, and activating an ignition kernel at the 260-second mark (see Appendix A.3). The flame exhibits a burst of energy immediately after the ignition event, and achieves a maximum heat release rate of 464 MW. The premixed combustion event is accompanied by a buoyant plume of hot gases that are ejected at the top of the domain. Transition from a premixed to non-premixed combustion appears to occur at 263 seconds, or 3 seconds after ignition. Kolmogorov-Petrovskii-Piskonov (KPP) theory

provides an estimate on the turbulent flame speed based on the laminar flame speed, the molecular diffusion Schimdt number, the progress variable filter size (Δ_c), and characteristic velocity and length scales [24]. The KPP-estimated flame speed for Case 1's combustion run was 6.8 m/s, or 17.7 times that of the laminar flame speed. The range of acceptable ratios for turbulent to laminar flame speed is 10 to 20. Twenty seconds after ignition, transition from a premixed to a non-premixed combustion state has since occurred, with the heat release rate achieving a steady state average of 158 MW. This is 8.14% less than the 172 MW value calculated from the product of the mass burn rate and the heat of combustion for methane. The difference in predicted maximum and FDS-calculated heat release rates is also observed in the latest publicly released version of FDS, and is thus attributable to the base model. Regardless, this value is reasonable for a burn rate of 3.32 kg/s, and is an improvement over the poor estimate given by the initial ignition attempt using the true flammability limits for methane.

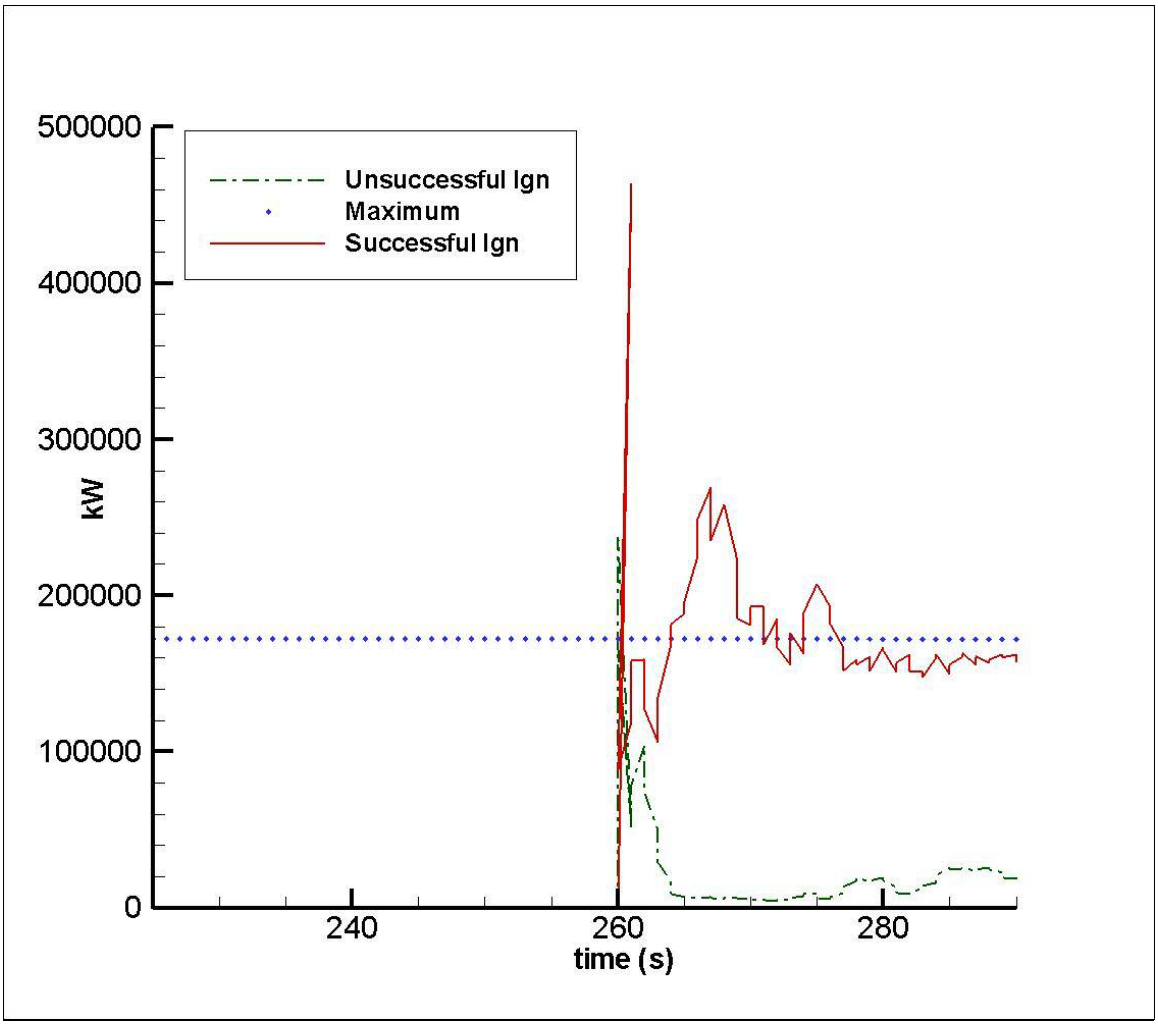

Figure 31: Calculated Heat Release Rate for Partially Premixed Combustion of Case 1 Dispersion; Successful and Unsuccessful Ignition with Maximum Predicted HRR

4.1.3 Diffusion Flame Height

The non-premixed flame height calculated by the FDS combustion test is 18.5 meters; this is determined by visualization of the steady state non-premixed combustion flame sheet, whose iso-surface is the extent of the stoichiometric mixture fraction (figure 32). Empirical correlations for the flame height depend on the predicted heat release rate and the diameter of the pool fire [40]. The pool in the present study is a 60 m^2 rectangle, and necessitates the use of the effective diameter concept. Predicted flame height from the empirical correlation for steady state non-premixed combustion is 20.92 meters and based on the expected 172 MW heat release rate and a 7.5-meter effective diameter. This value is also apparent in the mid-plane mixture fraction iso-contour plot in figures 33 and 34.

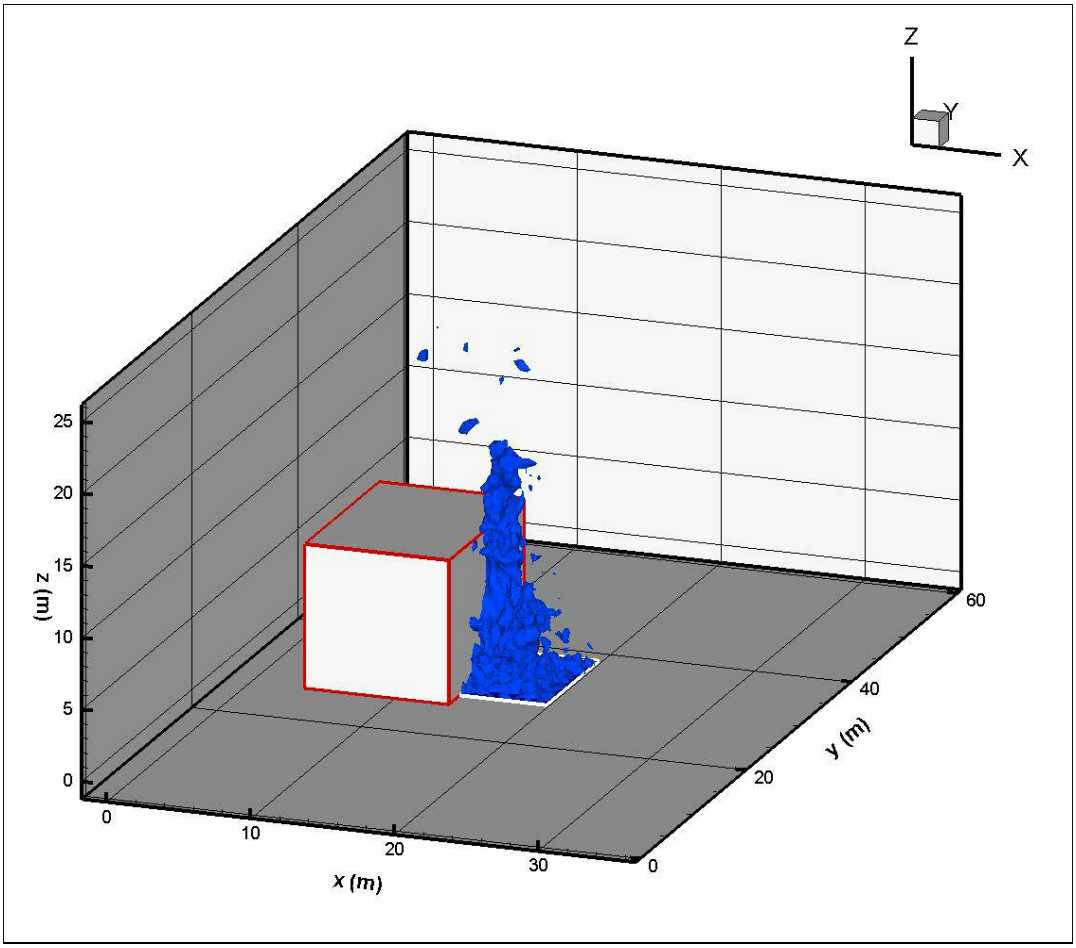

Figure 32: Iso-Surface of the FDS-Calculated Flame Height for Isometric View

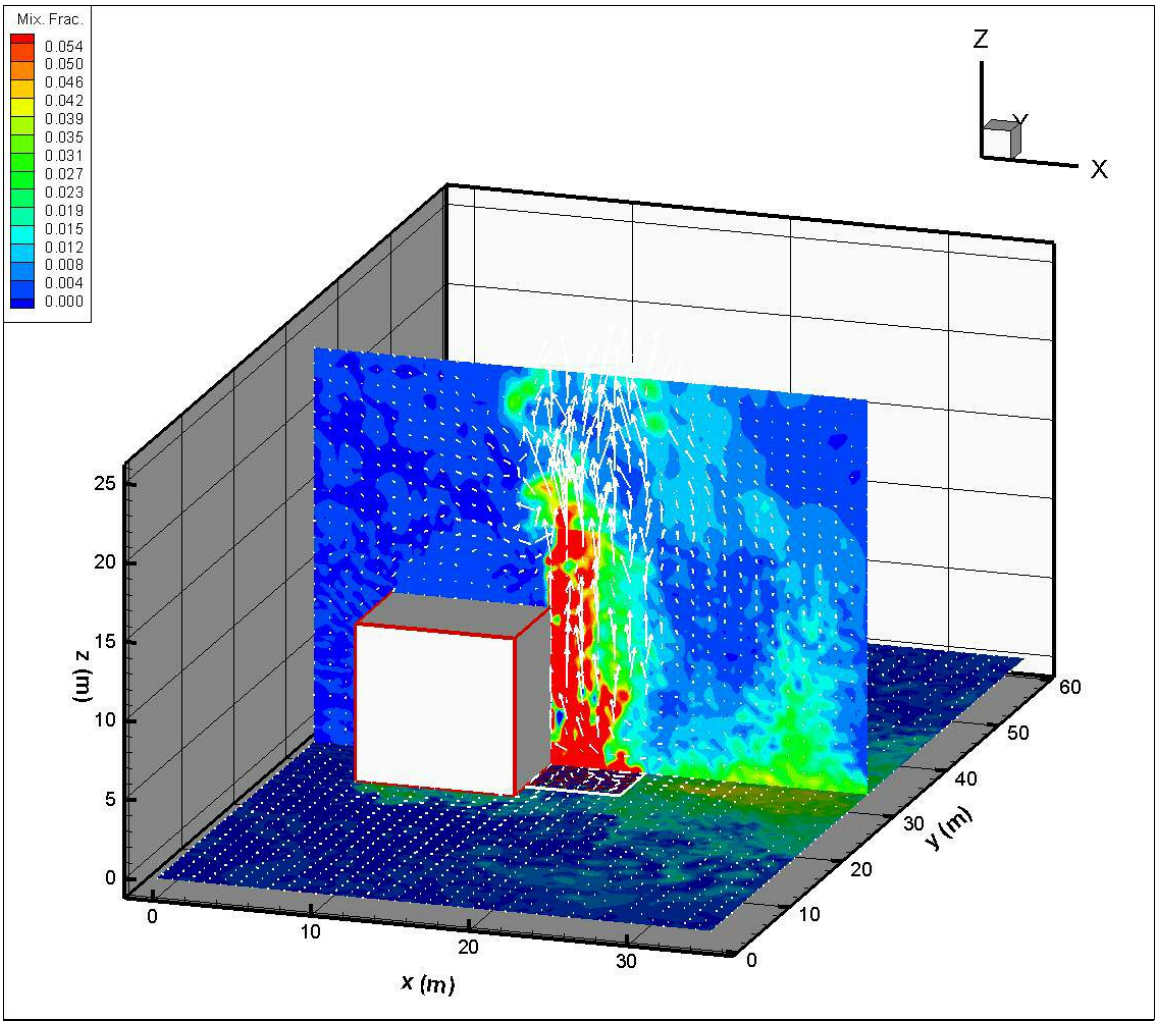

Figure 33: Mixture Fraction Iso-Contour of FDS-Calculated Flame Height at 280 seconds (Isometric View)

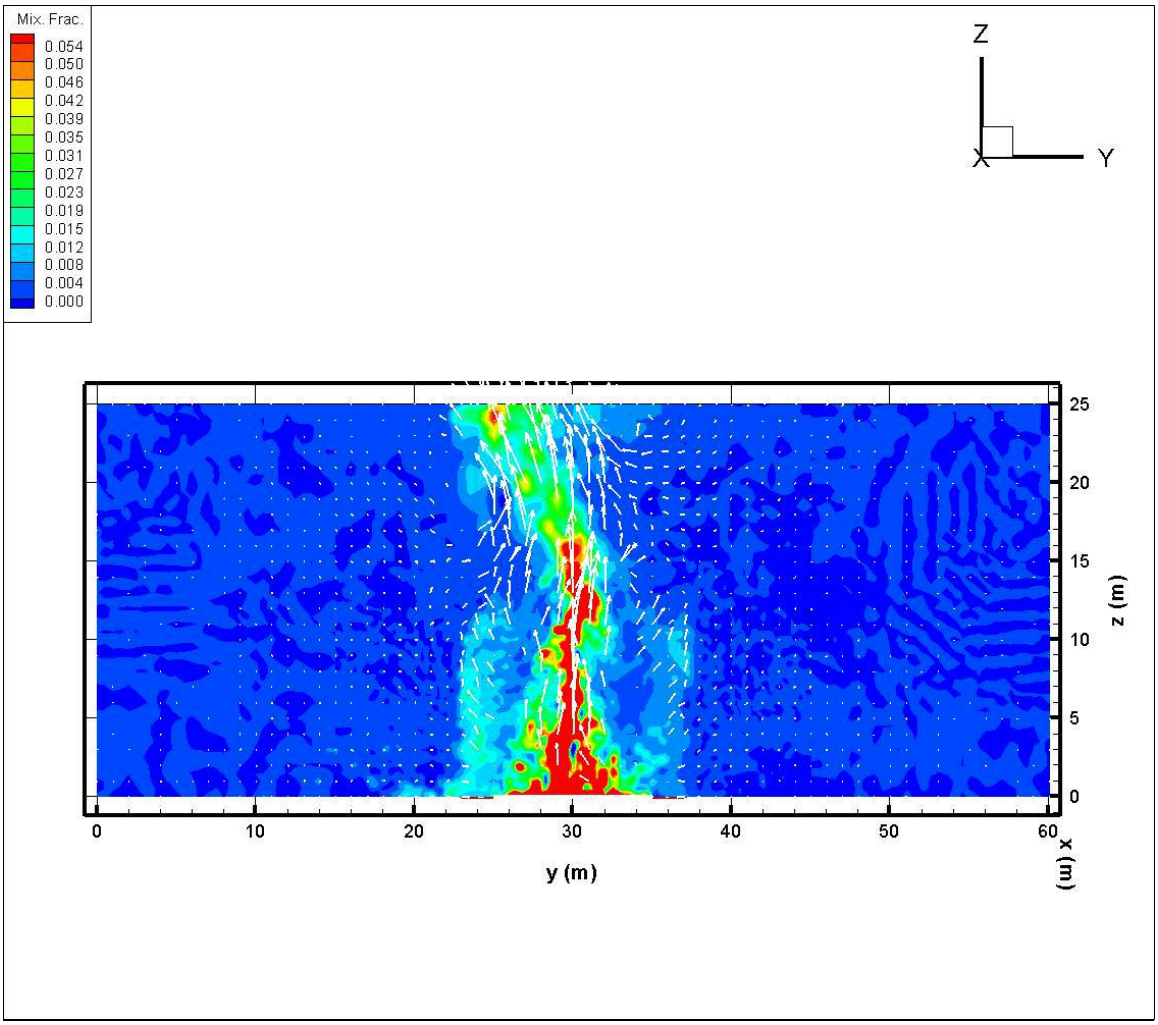

Figure 34: Mixture Fraction Iso-Contour of FDS-Calculated Flame Height at 280 seconds (Front View)

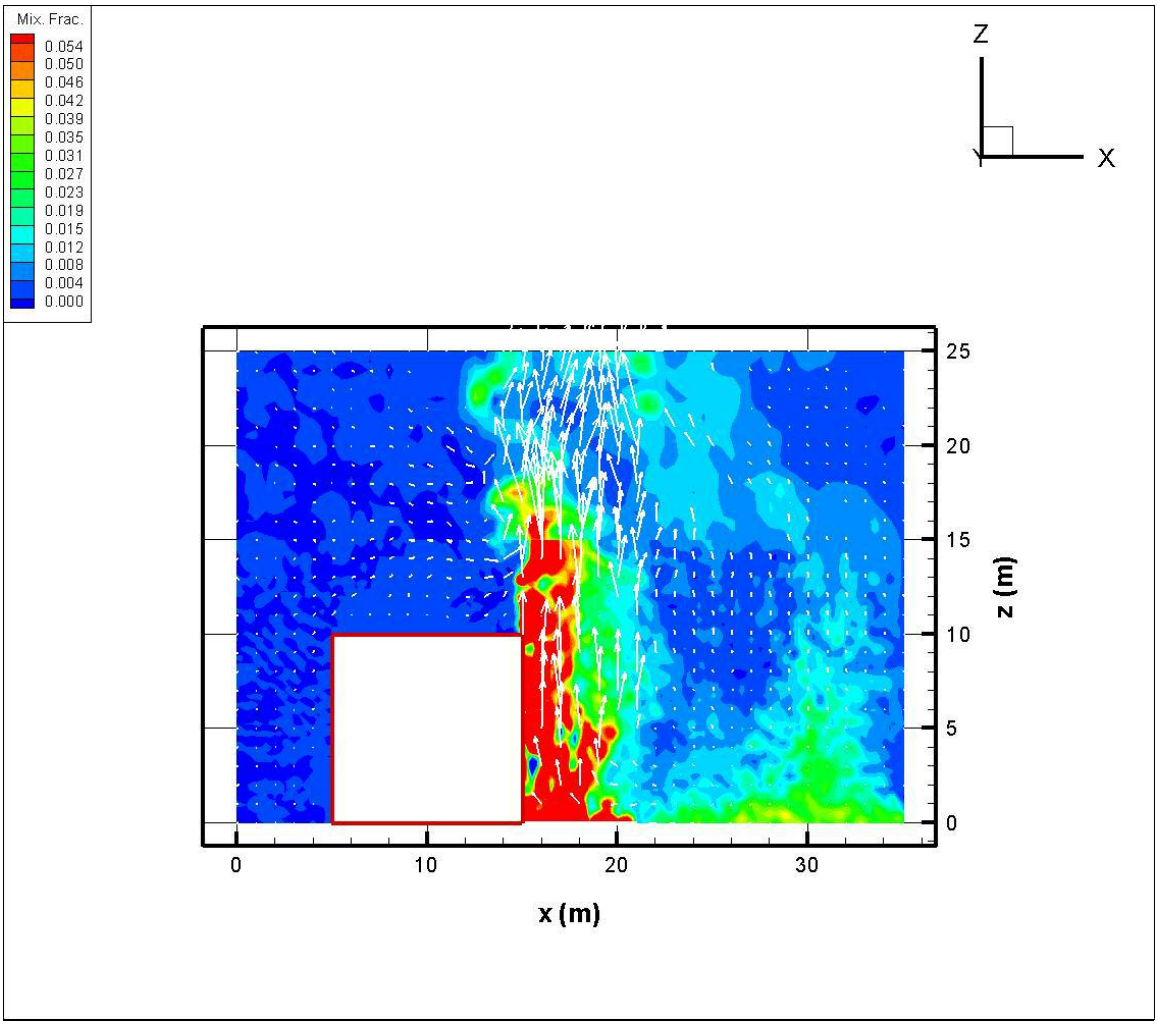

Figure 35: Mixture Fraction Iso-Contour of the FDS-Calculated Flame Height at 280 seconds (Side View)

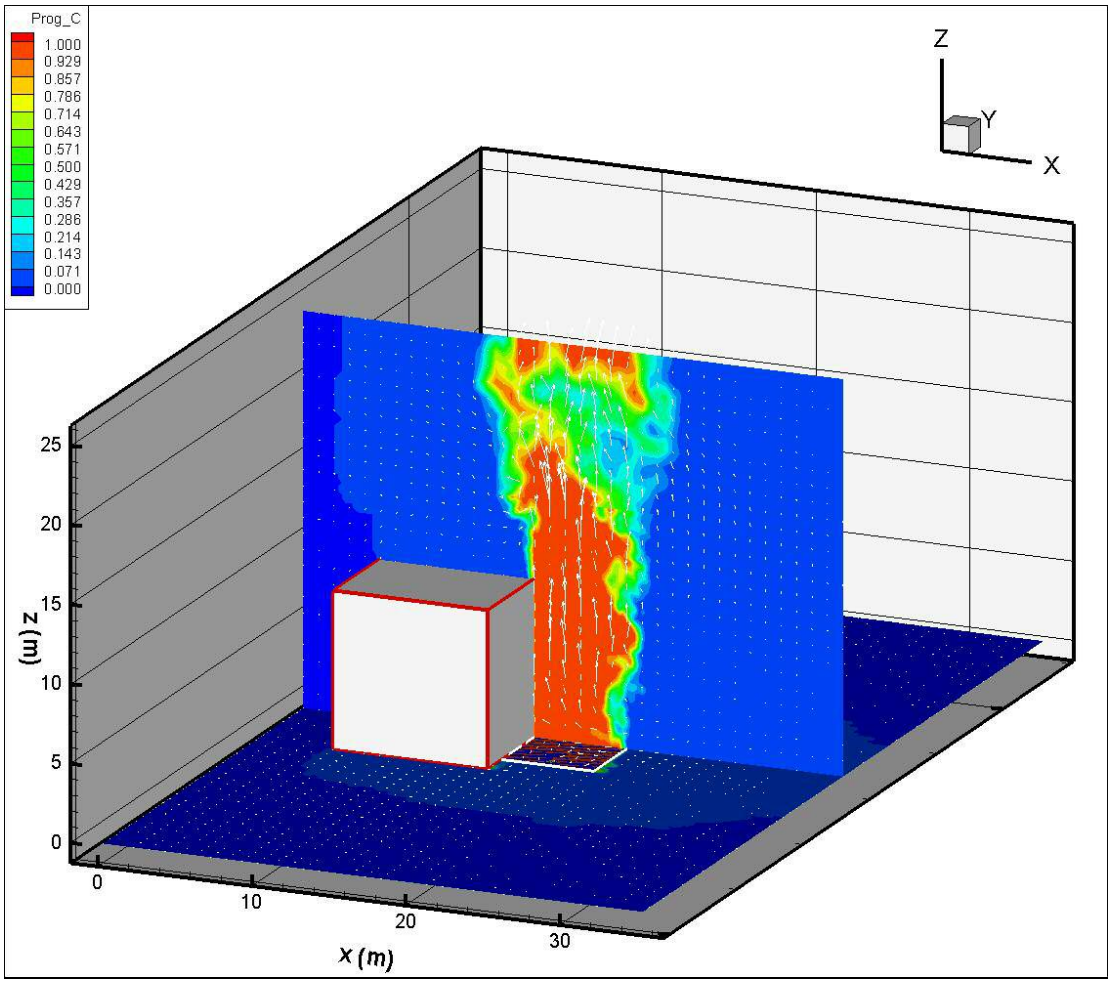

Figure 36: Iso-Contour of the FDS-Calculated Progress Variable at 280 seconds (Isometric View)

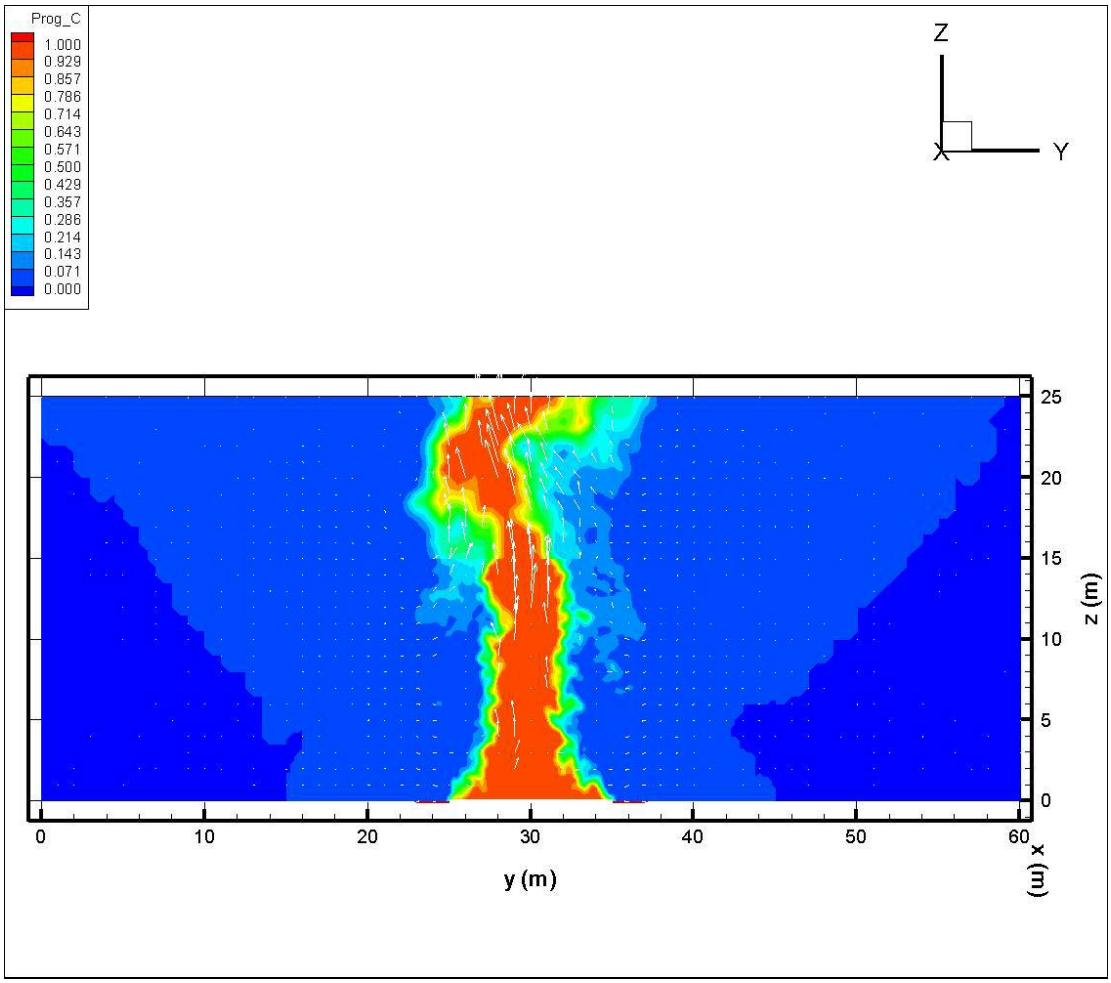

Figure 37: Iso-Contour of the FDS-Calculated Progress Variable at 280 seconds (Front View)

4.1.4 Incident Heat Flux

The National Fire Protection Association has designated incident heat fluxes of 5 kW/m^2 as a standard for estimating fire protection distances for people [4]. Incident heat flux measurements have consequently been taken during the combustion of dispersion Case 1 to ascertain the danger that persons in the vicinity of the fire would be subjected to.

The incident heat flux for finite distances downstream of the steady state pool fire can be approximated with the thermocouple incident heat flux input parameter. Point heat flux measurements were taken at 1-meter increments from the leeward edge of the methane leak. The size of the of the grid cells used in the current study (.25 and .5 meters) inhibits the accuracy of the radiation transport equation in FDS, which necessitates a prescribed radiant fraction to approximate the incident heat flux from the non-premixed flame.

The downstream incident heat flux plotted in figure 38 employs a radiative fraction of .3, which is twice the accepted value for a methane diffusion flame [41]; this action is meant to offset the radiative energy that is lost by reabsorption when the radiative fraction parameter is employed. At steady state time scales, the standard IHF value of 5 kW/m^2 is estimated to occur at approximately 10 meters.

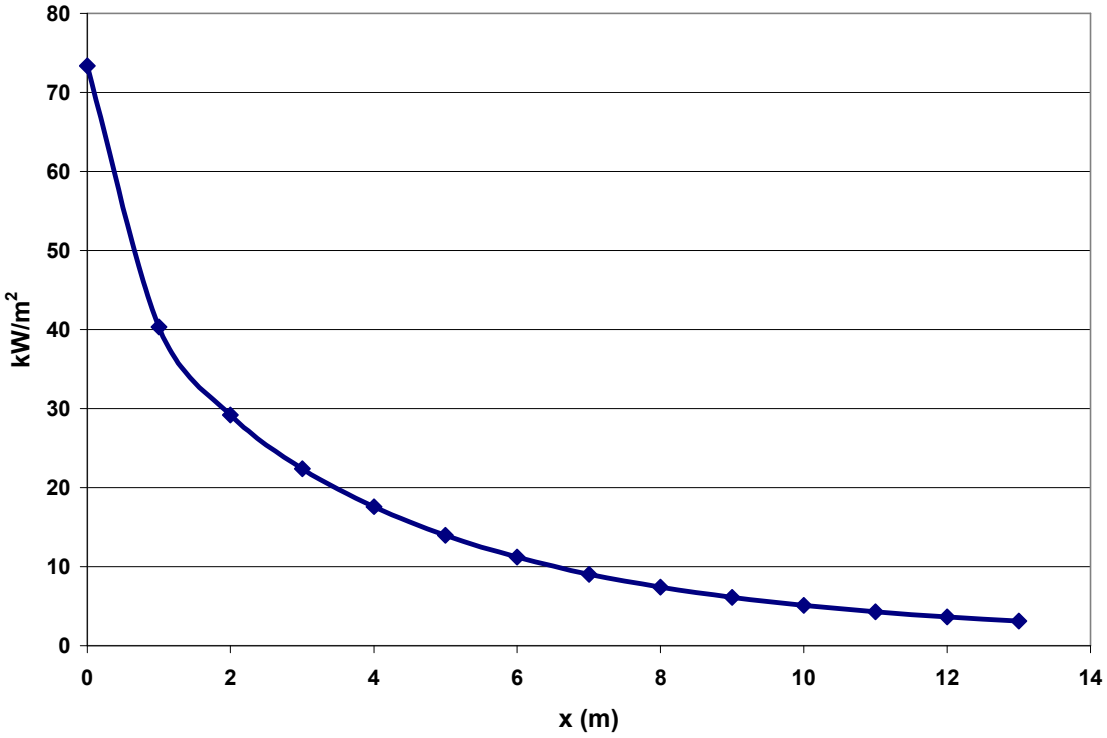

Figure 38: Incident Heat Flux Downstream of Methane Leak

CONCLUSION

5.1 Summary of Findings

The present study models the dispersion and combustion of a methane pool with a prescribed mass flux, emanating from a vaporizing liquid methane spill on top of a quiescent isothermal water surface.

The model was implemented in FDS, and used a rectilinear vent to simulate the vaporizing liquid methane pool with the appropriate cryogenic temperature and mass flux. A low aspect-ratio obstacle was placed between the vaporizing pool and an atmospheric wind blowing downstream in the positive x-direction. Different dispersion cases were defined by the magnitude of the wind velocity; 0.5 (Case 1), 1.0 (Case 2), and 2.0 (Case 3) m/s.

The Case 1 and Case 2 yielded similarly-sized flammable masses at steady state time scales; they reveal stratified masses of fuel-air mixture, where fuel-rich vapor sits between the pool and the flammable portions of the cloud. Case 3 produces a flammable methane mass roughly half of those found in the first 2 dispersions. U-velocity iso-contours demonstrate that for the 2.0 m/s velocity case, recirculation downstream of the obstacle is sufficiently strong to dilute the flammable mass above the pool surface. Dispersions for the lower wind velocity conditions allow for large flammable clouds directly above the pool. The dispersion model correctly predicts the density of the methane cloud, which can be observed by mixture fraction-temperature scatter plots.

Initial attempts to ignite the flammable cloud in Case 1 were unsuccessful. This is attributable to insufficient grid resolution and the inability of the reaction progress variable to propagate in a coarse grid. Consideration must also be given to the stratification of the methane cloud, where fuel-rich layers of mixture may have prevented the premixed flame from traveling to the vaporizing pool and transitioning into a diffusion flame event.

Although combustion for the dispersion cases in the present study is unlikely, changes were made to the methane flammability limits for the purpose of studying the diffusion flame. The heat release rate of a pure diffusion flame is unaffected by changes to the fuel's flammability limits.

Ignition of the flammable cloud from the Case 1 dispersion leads to an under-prediction in the steady state diffusion flame heat release rate. The non-premixed combustion flame height was similarly underestimated, yet reasonable. Incident heat flux values were also recorded using the point-measurement thermocouple diagnostic found in FDS.

5.2 Recommendations

Future work should expand the test matrix employed for the model outlined in this study. Liquid methane pool simulations should explore the effect of a greater array of wind speeds. Although the scope of the current study is to explore the effect of wind speed on methane cloud dispersion and combustion, a 'zero-velocity wind' test is advisable. Changes in wind direction and acceleration should be considered in a broadened scope.

The length, width, and height of the 3-dimensional obstacle should be varied, as changes in its size and shape affect the behavior of air flow around it, and by extension the mixing behavior of the gas dispersion [32, 33]. Consideration should be given to the position of the pool relative to the obstacle (for example, placement on the leeward versus the windward side of the prism, and placement in the center of the prism versus placement at the prism's corners). Enhanced grid resolution may capture smaller turbulent length scales that would otherwise be filtered out; it may also improve the reaction progress variable's ability to track the premixed flame sheet.

Dispersion and combustion tests should be conducted for different hydrocarbon cryogenic fuels, such as propane (the primary component of Liquefied Petroleum Gas, or LPG) and hydrogen (H_2). Propane specifically has a wider flammability limit than methane and may be more amenable to transition from a premixed to a diffusion flame.

Dispersing and burning different fuels, in addition to the difference in molecular weight, implies various fuel mass fluxes which also affects the amount of flammable mass in the test domain and time to a steady state flammable mass and hence the propensity for non-premixed combustion. Future work would also account for the mass flux of hydrocarbon fuel from the pool due to the heat feedback from the diffusion flame sitting above it.

A form of the shallow water equations can be implemented to model the spread of a vaporizing hydrocarbon pool. This implies high order temporal and spatial derivatives to solve for the height of the chemical spill, as well as its x and y velocity components; FDS uses a second-order predictor-corrector scheme in space and time to solve its hydrodynamic equations. A decision must also be made whether or not to pursue non-dimensional (normalized) solutions to the shallow water equations.

APPENDIX

A.1 Source Files for the Fire Dynamics Simulator

The following is a table listing the FDS source files [27]. FDS is written in Fortran 90 and can be compiled in Mac OS X, Unix/Linux, or Windows environments. The present work utilizes 14 Windows-based FDS source files that are compiled with Intel Fortran in Microsoft Visual Studio .Net 2003. The files handle governing equations, input file interpretation, output file data dumps and initialization, among other things.

In the case of a single process simulation, subroutines are called by main.f. Subroutines in a multiple process simulation are called by main_mpi.f, regardless of the existence of a message passing software such as MPICH.

File Name	Description
mods.f	Global arrays and constants
misc.f	Miscellaneous Routines
pois.f	Poisson (pressure) solver
radi.f	Radiation solver
sprk.f	Lagrangian particle transport and sprinkler activation
read.f	Read input parameters
init.f	Initialize variable and Poisson solver
divg.f	Compute the flow divergence
pres.f	Spatial discretization of pressure (Poisson) equation
mass.f	Mass equation(s) and thermal boundary conditions
velo.f	Momentum equations
dump.f	Dumps output data into files
isob.c	C Routine for computing iso-surface triangles
main.f, main_mpi.f	Main programs, serial and parallel versions

Table 3: FDS Source Code Files [27]

A.2 Optional FDS Input Quantities

Users specify all pertinent information for their simulation through a data file. This includes boundary conditions; the volatility or inertness of rectilinear surfaces and objects; vents that act as open doors or windows with mass fluxes, velocities, or heat release rates prescribed to them. The information prescribed in the data file is interpreted by subroutines found in the read.f module of FDS:

&HEAD: The **HEAD** input line in the **FDS** data file gives the name of all output file extensions. A simulation with the name 'CHID' entered on the **HEAD** line will have an output and end filenames of CHID.out and CHID.end, respectively.

&GRID: The **GRID** line allows the user to set the resolution of an individual block for the FDS job. The coarseness or smoothness of a single mesh is controlled by the **IBAR**, **JBAR**, and **KBAR** modifiers; increasing the numerical value of each improves the resolution of the grid in Cartesian coordinates. Simulations that utilize the MPI for multiple block processors require multiple GRID lines, i.e. a three-block job would need three **GRID** lines.

&PDIM: There is a **PDIM** line associated with every grid that prescribes the physical dimensions of the block to which it pertains. Minimum and maximum values are given in the x, y, and z directions.

&TWFIN: The user prescribes the total time of the FDS simulation, pertaining to all meshes (hence, **T**ime **W**hen **FIN**ished). FDS also allows users to set the time step (**DT**) for each incremental calculation.

&MISC: The miscellaneous line can be used to access the database (**DATABASE**), which is a list of material and fuel properties FDS calls on to calculate pertinent reactions. Information located in the database includes molecular weights for fuel, lower and upper flammability limits, laminar flame speeds, and the stoichiometric coefficients for hydrocarbon reactants and products. Users can also prescribe, among other parameters, the velocity of a wind in the domain, the domain's ambient temperature, and the number of output dumps per calculation.

&SPEC: Users can specify additional species on the **SPEC** line. FDS has the ability to track and transport these gases, with or without combustion. Non-zero values for the mass fraction of these extra gases must be prescribed. If the properties of these additional gases are not in the FDS database, they must also be assigned on the **REAC** line.

&REAC: FDS data files allow for users to prescribe the reaction of gases not included in **DATABASE**. Criteria found in the database file (molecular weights, stoichiometric coefficients, *et cetera*) would be listed here. A FDS data file will only one reaction line.

&SURF: This pertains to the surface line. All vents and objects must have some surface identification prescribed to it. The surface namelist allows for temperatures to be prescribed, as well as velocities, mass fluxes, and mass fractions should a vent area be described rather than a solid surface.

&OBST: Obstructions are rectilinear shapes in FDS, whose dimensions are given by minimum and maximum x, y, and z coordinates. Notice that in the example data file in figure 3, all obstructions have a **SURF_ID**.

&VENT: Vents are implemented in FDS like obstructions. Minimum and maximum dimensions from the x, y, or z direction must be zero, as vents are two dimensional objects in FDS. They are also identified by a **SURF** modifier, which may or may not allow gas to be injected into the simulation domain. The first vent in Appendix A.3 sample data file prescribes an opening in the object above it. The area of the opening is 4 m^2, will open when the time of the simulation is equal to zero, and has a '**LEAK**' surface identifier. In other words, a mass flux of 0.1 kg/ m^2/s will be injected into the domain from the '**LEAK**' vent area.

A.3 Sample FDS Input File

The following is a sample input (data) file for the combustion of the 0.5 m/s wind dispersion case. It is a four-block simulation that utilizes MPICH2 parallel processing capabilities. The simulation is set to run for 500.0 seconds, employs the FDS radiation model, and will be subjected to the additional methane species. Two surfaces have been prescribed to the FDS simulation; the first is a 'Leak' with a mass flux of .05537 $kg/m^2/s$ methane. Surfaces that have this ID prescribed to them will allow methane gas to be injected into the domain at a temperature of -162.0 C. The second surface ID is a wind, which is currently set to a velocity of 0.5 m/s. A 10.0 x 14.0 x 10.0 m^3 obstruction sits on the domain floor, its surfaces inert.

A pool sits against the leeward side of the obstruction, has an area of 60 m^2, and will inject methane from its leak-prescribed surface at time t = 0.0 seconds. The sides of the domain are open to the atmosphere, with one side dedicated to an inflow of wind due to its 'Wind' surface ID prescription. Volumetric thermocouples will record the fuel mass fraction of methane injected from the leak and the total flammable mass. A series of point thermocouples are positioned to record the incident heat flux from the downstream edge of the pool to the end of the domain 1-meter increments.

The mass is set to ignite at the Cartesian coordinates (x,y,z) = (18.0, 30.0, 2.25) at 260.1 seconds. Restart files are saved every 65.0 seconds, and in the event of a stoppage, the simulation will pick up from the latest set of CHID.restart files.

```
&HEAD CHID='pool_ship_real',TITLE='Tanker Methane Pool'/

&GRID IBAR=70,JBAR=30,KBAR=50 /
&PDIM XBAR0=0,XBAR=35.0,YBAR0=45.0,YBAR=60.0,ZBAR=25.0 /

&GRID IBAR=140,JBAR=120,KBAR=60 /
&PDIM XBAR0=0.0,XBAR=35.0,YBAR0=15.0,YBAR=45.0,ZBAR0=0.0,ZBAR=15.0 /

&GRID IBAR=70,JBAR=30,KBAR=50 /
&PDIM XBAR0=0.0,XBAR=35.0,YBAR0=0.0,YBAR=15.0,ZBAR0=0.0,ZBAR=25.0 /

&GRID IBAR=70,JBAR=60,KBAR=20 /
&PDIM XBAR0=0.0,XBAR=35.0,YBAR0=15.0,YBAR=45.0,ZBAR0=15.0,ZBAR=25.0 /


&TIME TWFIN=500.0,SYNCHRONIZE = .TRUE. /

&MISC RADIATION=.TRUE., DATABASE='./database3/database3.data',
SUPPRESSION=.FALSE., U0=0.5, REACTION='METHANE', DTCORE=65.0,
RESTART=.TRUE. /

&SPEC ID='MIXTURE_FRACTION',MASS_FRACTION_0=0.0 /

&REAC ID='METHANE'
      FYI='Methane, C H_4'
      MW_FUEL=16
      NU_O2=2.
      NU_CO2=1.
      NU_H2O=2.
      SOOT_YIELD=0.01
      RADIATIVE_FRACTION=0.15
      Z_LEAN = 0.0288
      Z_RICH = 0.70
      S_LST = 0.383  /

&SURF ID='LEAK', MASS_FRACTION(1)=1.0, TMPWAL=-162.0,
RGB=1.0,0.0,0.0, MASS_FLUX(1)=0.05537 /
&SURF ID='WIND', VEL=-0.5 /
&SURF ID='EARTH', RGB=0.50, 0.26, 0.16 /

&OBST XB=5.0, 15.0, 23.0, 37.0, 0.0, 10.0, SURF_ID='INERT' /
&VENT XB=15.0, 21.0, 25.0, 35.0, 0.0, 0.0, SURF_ID='LEAK', T_OPEN = 0.0
/

&VENT XB=0.0, 0.0, 0.0, 60.0, 0.0, 25.0, SURF_ID='WIND',
VENT_COLOR='INVISIBLE'  /

&VENT XB=0.0, 35.0, 0.0, 0.0, 0.0, 25.0, SURF_ID='OPEN' /
&VENT XB=0.0, 35.0, 60.0, 60.0, 0.0, 25.0, SURF_ID='OPEN' /
&VENT XB=35.0, 35.0, 0.0, 60.0, 0.0, 25.0, SURF_ID='OPEN' /
&VENT XB=0.0, 35.0, 0.0, 60.0, 25.0, 25.0, SURF_ID='OPEN' /

&VENT XB=0.0, 35.0, 0.0, 25.0, 0.0, 0.0, SURF_ID='EARTH' /
&VENT XB=0.0, 35.0, 35.0, 60.0, 0.0, 0.0, SURF_ID='EARTH' /
&VENT XB=0.0, 15.0, 25.0, 35.0, 0.0, 0.0, SURF_ID='EARTH' /
&VENT XB=21.0, 35.0, 25.0, 35.0, 0.0, 0.0, SURF_ID='EARTH' /
```

```
&DEFI IGNITION=.TRUE., XYZ(1) = 18.0, XYZ(2) = 30.0, XYZ(3) = 2.25,
R_IGN = 1.0, T_IGN_ON = 260.1, T_IGN_OFF = 261.1 /

&PL3D DTSAM=20.0, WRITE_XYZ=.TRUE.,
QUANTITIES='MIXTURE_FRACTION','TEMPERATURE','PROGRESS_VARIABLE','HRRPUV
','U-VELOCITY','V-VELOCITY', 'W-VELOCITY' /

&THCP DTSAM=5.0, XB=0.0,35.0,15.0,45.0,0.0,15.0,QUANTITY='flammable
mass',LABEL='Flammable Mass in Main Block' /

&THCP DTSAM=5.0, XB=0.0,35.0,15.0,45.0,0.0,15.0,QUANTITY='fuel mass
fraction',LABEL='Fuel Mass Fraction in Main Block' /

&THCP DTSAM=5.0, XYZ=21.0,30.0,0.0,QUANTITY='INCIDENT_HEAT_FLUX',
IOR=3, LABEL='IHF 6 m' /

&THCP DTSAM=5.0, XYZ=22.0,30.0,0.0,QUANTITY='INCIDENT_HEAT_FLUX',
IOR=3, LABEL='IHF 7 m' /

&THCP DTSAM=5.0, XYZ=23.0,30.0,0.0,QUANTITY='INCIDENT_HEAT_FLUX',
IOR=3, LABEL='IHF 8 m' /

&THCP DTSAM=5.0, XYZ=24.0,30.0,0.0,QUANTITY='INCIDENT_HEAT_FLUX',
IOR=3, LABEL='IHF 9 m' /

&THCP DTSAM=5.0, XYZ=25.0,30.0,0.0,QUANTITY='INCIDENT_HEAT_FLUX',
IOR=3, LABEL='IHF 10 m' /

&THCP DTSAM=5.0, XYZ=26.0,30.0,0.0,QUANTITY='INCIDENT_HEAT_FLUX',
IOR=3, LABEL='IHF 11 m' /

&THCP DTSAM=5.0, XYZ=27.0,30.0,0.0,QUANTITY='INCIDENT_HEAT_FLUX',
IOR=3, LABEL='IHF 12 m' /

&THCP DTSAM=5.0, XYZ=28.0,30.0,0.0,QUANTITY='INCIDENT_HEAT_FLUX',
IOR=3, LABEL='IHF 13 m' /

&THCP DTSAM=5.0, XYZ=29.0,30.0,0.0,QUANTITY='INCIDENT_HEAT_FLUX',
IOR=3, LABEL='IHF 14 m' /

&THCP DTSAM=5.0, XYZ=30.0,30.0,0.0,QUANTITY='INCIDENT_HEAT_FLUX',
IOR=3, LABEL='IHF 15 m' /

&THCP DTSAM=5.0, XYZ=31.0,30.0,0.0,QUANTITY='INCIDENT_HEAT_FLUX',
IOR=3, LABEL='IHF 16 m' /

&THCP DTSAM=5.0, XYZ=32.0,30.0,0.0,QUANTITY='INCIDENT_HEAT_FLUX',
IOR=3, LABEL='IHF 17 m' /

&THCP DTSAM=5.0, XYZ=33.0,30.0,0.0,QUANTITY='INCIDENT_HEAT_FLUX',
IOR=3, LABEL='IHF 18 m' /

&THCP DTSAM=5.0, XYZ=34.0,30.0,0.0,QUANTITY='INCIDENT_HEAT_FLUX',
IOR=3, LABEL='IHF 19 m' /
```

B.1 Implementation of a Parallel Processing Network Using MPICH2

The following text outlines the procedure followed in order to utilize the Microsoft Windows implementation of the message passing interface (MPI).

Local Area Connection Properties

The local area connections between machines participating in the MPI network must have identical subnet masks, default gateways, preferred DNS servers, and alternate DNS servers. The idea is to make all communication between the participating machines as transparent as possible. Right click 'My Network Places' and select 'Properties'. Select 'Local Area Connection' to get to the 'Local Area Connection Status' window. From here, select 'Properties' to obtain the 'Local Area Connection Properties' window.

This will allow you to select change you IP and DNS settings in the 'Internet Protocol' (TCP/IP) window. The TCP/IP properties can be changed in this window (Subnet mask, Default gateway, Preferred DNS and Alternate DNS servers).

The Subnet mask numbers for all of the participating machines must have identical Subnet masks. This is also true for the Default gateway address, as well as for each of the DNS servers. All of these respective addresses should be identical in order to make machine-to-machine communication as transparent as possible.

Additionally, Windows XP machines will likely have a firewall, which should be turned off so as not to impede communication between participating machines.

Network Groups

All participating machines must belong to the same workgroup. This is accomplished by right-clicking' My Computer', selecting 'Properties', and then clicking on the 'Computer Name' tag. Selecting the 'Change' option will allow the user to change the workgroup so that their ID is identical to the workgroup name of all other MPI participants. In order for these changes to take place, it is likely that you will have to restart your machine.

To check that each computer is in the same workgroup and that all computers in the workgroup can see each other, double-click 'My Network Places'. In Windows XP, you can view your workgroup computers on the left-hand side of the 'My Network Places' window, under 'Network Tasks'. All computers in the MPI workgroup should appear. You can access shared folders on each computer by double-clicking the name for each machine. Similarly, shared folders on other machines can be accessed on Windows 2000 OS machines. Double-click 'My Network Places' and then select 'Computers Near Me'. The workgroup should appear.

Usernames and Passwords

MPI threads are accessible from each machine only if they are logged on under an identical username and password. Each of these identical users should have full administrator privileges, which are granted in the process of creating the user on each machine. The interface for creating new users differs slightly for Windows 2000 and Windows XP OS.

Windows 2000

Go to the start menu and select settings to access the control panel. From there, select the 'Users and Password's icon. In the 'Users and Passwords' window, select 'Add'. This should be beneath the list of existing users. When prompted for a Username, type the name shared among those machines participating in the MPI network. Select 'Next', and the same procedure should be followed for the password. On the next page, when prompted for the user's level of access, select 'Other'. Make sure the user has full administrative privileges before finishing the user account.

When using processes from a machine using the Windows 2000 OS, you must be logged on as this shared user, meaning identical username and password.

Windows XP

The 'User Accounts' window can be accessed by selecting 'Start', 'Settings', and then the control panel. When prompted to pick a task in the 'User Accounts' window, select the option allowing you to create a new account. You will be asked to type a name for the

new account; this will be the shared username. You will next be asked for an account type, which should already be defaulted to 'Computer administrator'. Choose to create the account, and when you are brought back to the main 'User Accounts' window, select the account you have just created. Choose to create a password for this account, which will be identical to the shared MPI password.

Windows XP machines allow multiple users to be logged on simultaneously. As long as you switch users when you leave the account on screen, and do not log off, more than one user can run programs at the same time. This is not true for Windows 2000 machines.

Downloading and Installing MPICH2

MPICH is a Message-Passing-Interface implementation developed by Argonne National Laboratories . Recently, MPICH2 has replaced 1.x.x versions of MPICH, and should be readily downloadable from ANL's MPICH2 website [38]:

http://www-unix.mcs.anl.gov/mpi/mpich2/

Easy installation can be accomplished by selecting the 'Win32 IA32 platform', and downloading the http version of 'mpich2-1.0.3-1-win32-ia32.msi', an 8.2 MB file. The current version is 1.0.3. This should download the installation package for MPICH2 to your Windows desktop.

Double-clicking the installation icon on your desktop will prompt a window asking for the place on your computer that MPICH2 will be kept. Choose the default C:\Program Files\MPICH2. Installation will also ask for a name by which all processes will be

identified (the default password is ‘behappy’). All machines in the MPI cluster must have this same name. Once this is completed, finish the installation. MPICH2 must be installed on all participating machines, in the file extension C:\Program Files\MPICH2.

Compiling Visual FORTRAN Using MPICH2 Files

Fortran code is compiled in Visual Studio .Net 2003 for MPICH2 in exactly the same way it is compiled for the original MPICH. The only thing that needs to change is which Include and Library files the project is pointing to when the code is being compiled in Visual Studio .Net.

Opening up the project and selecting ‘Project’ and ‘Project Properties’ will bring you to the property page. The leftmost menu in the ‘Project Property’ window will provide myriad compiling options.

Select ‘Fortran’ in the leftmost menu in the ‘Project Properties’ page (the exact name will be the executable name, followed by ‘Property Pages’), and then the ‘General’ submenu. The main menu will have options for debugging, optimization, preprocessor definitions, and additional include directories. Under ‘Additional Include Directories’, type C:\Program Files\MPICH2\Include. Afterwards, select ‘Preprocessor’ in the leftmost ‘Fortran’ submenu. Make certain that C:\Program Files\MPICH2\Include is also typed in as this menu’s ‘Additional Include Directories’ option.

It is also advisable to ensure compilation is optimized for the specific computer processor of your machine. Under 'Fortran'/'Optimization', there are two optimization parameters of note: 'Optimize for Intel(R) Processor' and 'Use Intel(R) Processor Extensions'. Assuming a Pentium 4 machine, the first parameter should be set to 'Pentium(R) 4 and additional Intel processors (see documentation)'. The second parameter should be set to 'Intel Pentium(R) 4 and compatible Intel processors'. Both of these parameter settings should be available in a pull-down menu to the right of the parameter description.

The leftmost menu has a 'Linker' option, and it is here that you prescribe the library files that your code will use when being compiled. Selecting the input submenu will provide the 'Additional Dependencies' slot in the right-hand menu in the 'Property Pages' window. Here, you should type C:\Progra~1\MPICH2\Lib\fmpich2.lib, which refers to the fmpich2 library file in the 'Programs Files' folder on the computer's hard drive.

This should be enough information to successfully compile your processor in Visual Studio .Net 2003.

The last step for MPICH2 parallel processing would be to make identical folders on each participating machine. Each folder would be shared to every other machine on the network, and each would have a copy of the compiled FDS executable, and ideally, a copy of MPICH2. For example, an executable with an extension of C:\Documents and Settings\All Users\Desktop\IH_Run\HS-FDSRun on the host machine should have identical extensions on each of the other participating PCs.

The folder with the executable would have to be shared, and all users would have to have full administrator privileges. The folder on the machine which initiates the executable must not only have that executable, but also a configuration file simplifying startup of multiple block simulations. This configuration file can be accessed through a Windows command prompt and then changing the directory to where the file is located. MPICH2 executables utilizing configuration files are accessed at the command prompt by typing:

mpiexec.exe –file [filename]

The term [filename] refers to the name of the configuration file, which is config.txt.

If the networking addresses (except for the IP address) are identical, all of the folders are shared, all of the computers belong to the same workgroup and have identical usernames and passwords, and the appropriate MPICH2 files are used to compile the executable in Visual Studio, the code should run, and files generated by the separate blocks should be sent to the host machine's folder.

C.1 Mixture Fraction-Temperature Scatter Plots

This section is supplementary to Section 3.2.4, and illustrates the mixture fraction/temperature relationship in dispersion Cases 2 and 3. All three dispersions exhibit reasonable mixture fraction/temperature scatter. The Case 3 relationship (figure 40) differs slightly, as its lowest temperatures are 50 degrees C higher than the lower-wind dispersions. This is attributable to the strong recirculation downstream of the obstruction, which pushes much of the fuel-rich mass in the negative x-direction, and then laterally toward side recirculation regions and strong horseshoe vortices.

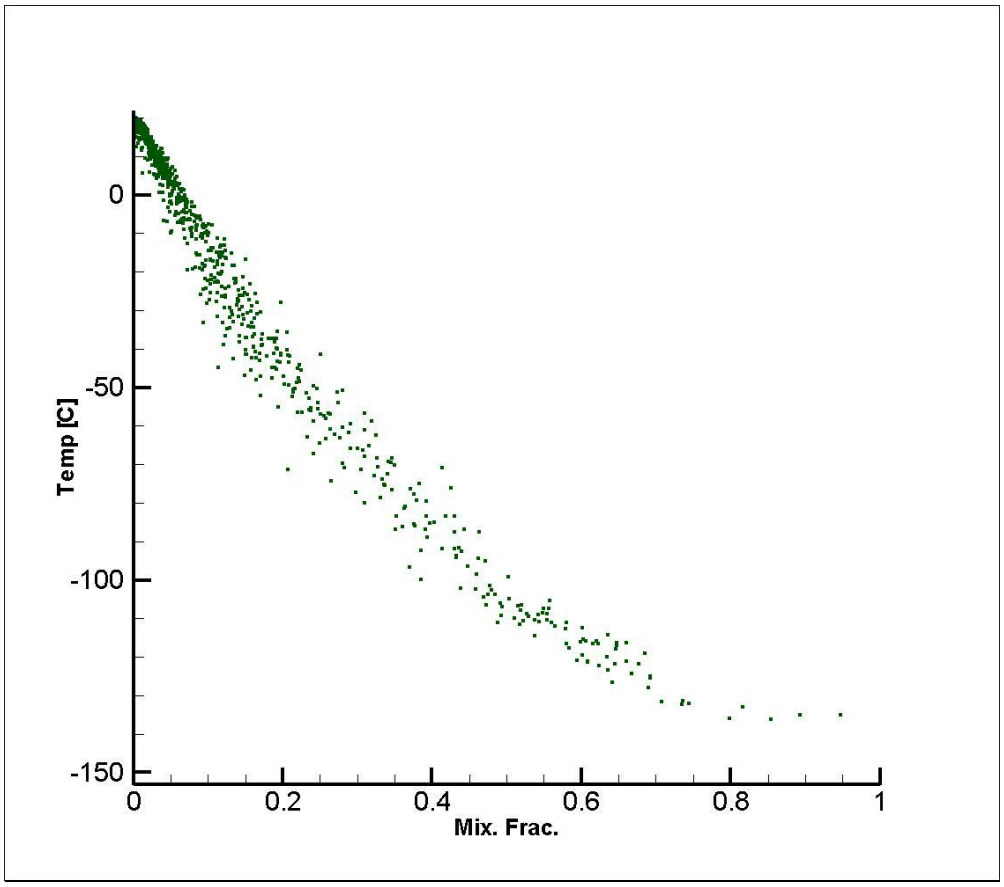

Figure 39: Mixture Fraction-Temperature Scatter for Case 2 (1.0 m/s Wind) Dispersion

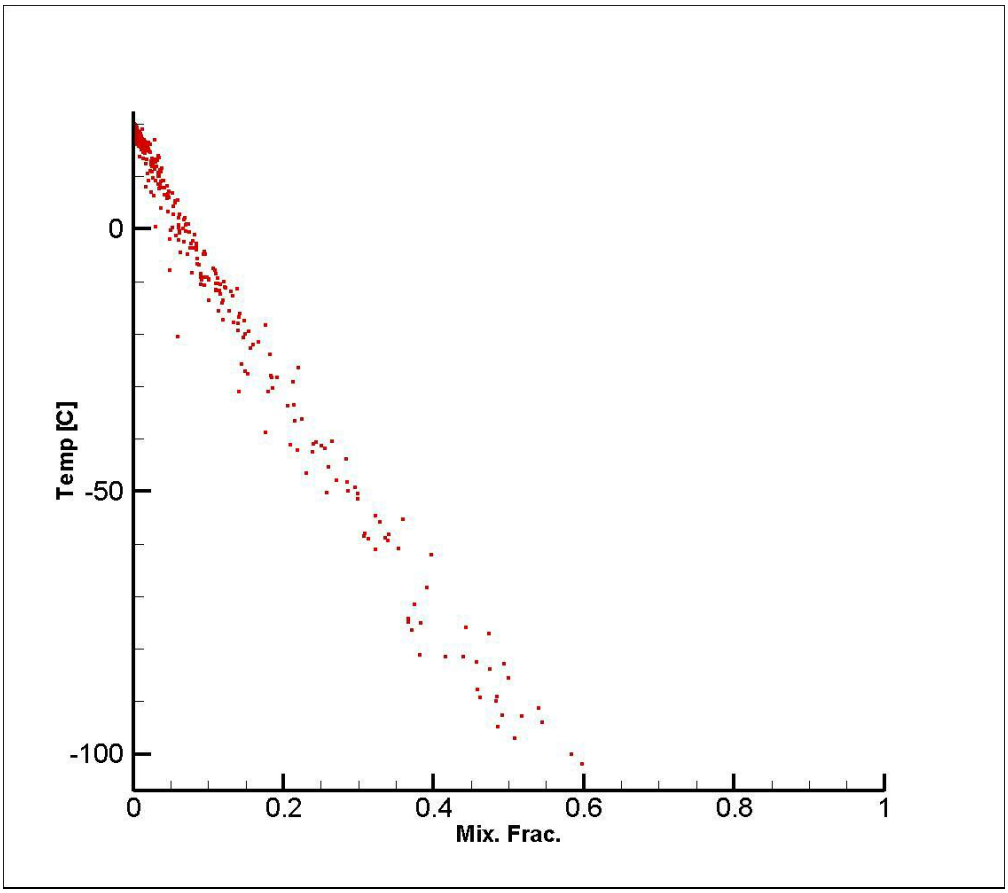

Figure 40: Mixture Fraction-Temperature Scatter for Case 3 (2.0 m/s Wind) Dispersion

REFERENCES

1. Administration, E.I., *U.S. Natural Gas Imports By Country*.

2. Administration, E.I., *U.S. Natural Gas Imports by Country*. 2006, Energy Information Administration.

3. *U.S Daily Average Supply and Disposition of Crude Oil*, in *Monthly Natural Gas Liquids Report*. 2004, Evironmental Information Administration.

4. Hightower, M., Gritzo, L., Luketa-Hanlin, A., Covan, J., Tieszen, S., Wellman, G., Irwin, M., Kaneshige, M., Melof, B., Morrow, C., Ragland, D., *Guidance on Risk Analysis and Safety Implications of a Large Liquified Natural Gas (LNG) Spill Over Water*, in *Sandia Report*. 2004, Sandia National Laboratories: Albuquerque, New Mexico.

5. Kaplan, A., Marshall G., *Worldwide LNG Trade to Expand with Gas Demand.* Oil & Gas Journal, 2003.

6. *Annual Energy Outlook 2005 with Projections to 2025*. 2005, Environmental Information Administration.

7. *Annual Energy Outlook 2006 with Projections to 2030*. 2006, Environmental Information Administration.

8. *Energy Information Administration Report*. 2003, Energy Information Administration.

9. *The LNG Value Chain*, Center for Energy Economics, BEG/UT Austin.

10. Commission, F.E.R., *Existing and Proposed North American LNG Terminals*, Federal Energy Regulatory Commission.

11. *Liquefied Natural Gas: The Wrong Choice for California*, Pacific Environment: San Francisco, California.

12. *LNG: Site-by-Site Impacts*, Ratepayers for Affordable, Clean Energy: San Francisco, California.

13. Dweck, J., Boutillon, S., *Deadly LNG Incident Holds Key Lessons for Developers, Regulators.* Pipeline & Gas Journal, 2004.

14. Branigin, W., *Two Sentenced to Death for USS Cole Attack*, in *Washington Post*. 2004: Washington, D.C.

15. *Yemen ship attack 'was terrorism'*. 2002, BBC News.

16. Lehr, W., Simecek-Beatty, D., *Comparison of Hypothetical LNG and Fuel Oil Fires on Water.* Journal of Hazardous Materials, 2004. **107**: p. 3-9.

17. Conrado, C., Vesovic, V., *The Influence of Chemical Composition on Vaporization of LNG and LPG on Unconfined Water Surfaces.* Chemical Engineering Science, 2000. **55**: p. 4549-4562.

18. Fay, J.A., *The Spread of Oil Slicks on a Calm Sea.* 1969.

19. Fay, J.A., *Model of Spills and Fires from LNG and Oil Tankers.* Journal of Hazardous Materials, 2003. **M96-2003**: p. 171-188.

20. Turns, S.R., *An Introduction to Combustion: Concepts and Applications, 2nd Ed.* 2000: McGraw-Hill.

21. Novozhilov, V., Koseki, H., *CFD Prediction of Pool Fire Burning Rates and Flame Feedback.* Combustion Science and Technology, 2004. **176**: p. 1283-1307.

22. Havens, J., *A Dispersion Model for Elevated Dense Gas Jet Chemical Release: Volume 2, User's Guide*. 1988, Environmental Protection Agency: Research Triangle Park, North Carolina.

23. Ermack, D.L., *User's Manual for SLAB: An Atmospheric Dispersion Model For Denser-Than-Air Releases [Abridged Version]*, A.a.G.S.D. Physics Department, Lawrence Livermore National Laboratory, Editor. 1990.

24. Trouvé, A., *Advanced Fire Modeling*. 2004.

25. Bernard, P.S., Wallace, J.M., *Turbulent Flow: Analysis, Measurement, and Prediction*. 2002: John Wiley & Sons, Inc.

26. McGrattan, K.e., *Fire Dynamics Simulator (Version 4) Technical Reference Guide, NIST Special Publication 1018*, NIST, Editor. 2005.

27. McGrattan, K., Forney, G., *Fire Dynamics Simulator (Version 4) User's Guide, NIST Special Publication 1019*, NIST, Editor. 2004.

28. Trelles, J., Kelly, A., Lattimer, B. *Validation of a Field Model for Liquid Spills*. in *Interflam 2004*. 2004. Edinburgh, Scotland.

29. Toro, E.F., *Shock-Capturing Methods for Free-Sufrace Shallow Flows*. 2001: Wiley and Sons Ltd. 309.

30. Opschoor, G., *Investigations into the Spreading and Evaporation of LNG Spilled on Water.* Cryogenics, 1977. **17**: p. 629-633.

31. Barbrauskas, V., *Heat Release Rates.* The SFPE Handbook of Fire Protection Engineering: Third Edition: p. 3.1-3.37.

32. Martinuzzi, R., Tropera, C., *The Flow Around Surface-Mounted, Prismatic Obstacles Placed in a Fully Developed Channel Flow.* Journal of Fluids Engineering, 1993. **115**(1): p. 85-92.

33. Krajnović, S., Davidson, L., *Large-Eddy Simulation of the Flow Around a Bluff Body.* AIAA, 2002. **40**(5): p. 927-936.

34. Kogaki, T., Kobayashi, T., and Taniguchi, N., *Large Eddy Simulation of Flow Around a Rectangular Cylinder.* Fluid Dynamics Research, 1998. **20**(1-6): p. 11-24.

35. Williamson, J., McGill, J., Trouvé, A., *A Filtered Progress Variable Approach to Model Turbulent Premixed Combustion in FDS. in Intl. Tech. Congress on Computational Simulation Models in Fire Engr. and Res.* 2004.

36. Hu, Z., Panafieu, G., Stauder, J., Trouvé, A., *A Presumed Pdf Approach to Model Turbulent Non-Premixed Combustion in FDS. in Intl. Tech. Congress on Computational Simulation Models in Fire Engr. and Res.* 2004.

37. Trouvé, A., *Large Eddy Simulation of the Transition from Premixed to Non-Premixed Turbulent Combustion Following Ignition of a Fuel Vapor Cloud.* 2005.

38. Gropp, W., Lusk, E., Ahton, D., Buntinas, D., Butler, R., Chan, A., Ross, R., Thakur, R., Toonen, B., *MPICH2 User's Guide*, M.a.C.S. Division, Editor. 2006, Argonne National Laboratory.

39. Bohl, D., Jackson, G., *Experimental Study of the Spill and Vaporization of a Volatile Liquid. in American Physical Society, 58th Annual Meeting of the Division of Fluid Dynamics.* 2005: American Physical Society

40. Gottuk, D.T., White, D.A., *Liquid Fuel Fires.* The SFPE Handbook of Fire Protection Engineering: Third Edition. **National Fire Protection Agency Association**: p. 2.297-3.316.

41. Gore, J.P., Zhan, N.J., *NOx Emission and Major Specie Concentrations in Partially Premixed Laminar Methane / Air Co-flow Jet Flames.* Combustion and Flame, 1995. **105**: p. 414-427.